Inhomogeneities and instabilities of Bose-Einstein condensates in rough potential landscapes

by

Joe Shearring, MSci

Thesis submitted to the University of Nottingham for the degree of Doctor of Philosophy, July 2013.

Abstract

In this work we investigate the dynamics of Bose-Einstein condensates (BECs) in inhomogeneous potential landscapes. As this research field continues to develop, more attention will focus on non-equilibrium systems, on potential applications that use condensates, and on the integration of cold atoms with other physical systems. This thesis covers all of these areas.

We begin by recapping the historical background of condensate physics, with a definition of the condensed phase and discussion of various analytical quantities of relevance to this work. The Landau picture of superfluidity and predictions of its breakdown, given by the Landau criterion, is particularly pertinent to the results on supersonic flow in an inhomogeneous system.

After outlining current experimental procedures, we present a computationally efficient modelling technique, used in our numerical simulations of atomic condensates. We then use this technique to study the dynamics of supersonic condensate flow, in the presence of a perturbing potential. Normally one would expect this situation to introduce disturbances, known as Landau excitations into the system, potentially destroying it. However, we find, under certain circumstances, complete suppression of Landau excitations: a behaviour that has not, to our knowledge, been previously observed. The efficiency of our chosen modeling technique allowed the possibility to conduct the large phase space campaigns necessary to find these special circumstances. On investigation, the mechanism resulting in the suppression of these Landau excitations is continuously related to the presence of transmission resonances in an equivalent linear

quantum system. This demonstration of a link between linear and non-linear quantum regimes is of great interest in understanding possible behaviour in other non-equilibrium superfluid systems.

Finally, we consider the magnetic fields from small scale (~ 1 µm) quantum electronic devices fabricated within a two-dimensional electron gas (2DEG). We demonstrate that atomic condensates provide a powerful tool for imaging these fields, or indeed similar fields created by other structures. Using a Fourier method, we show that the field profile that would be measured by the condensate can be used to recreate the current density of the 2DEG structure. The spatial resolution of this current mapping technique is limited only by the separation of the condensate from the current-carrying structure. We also show that quantum electronic conductors in 2DEGs are well suited to form a new generation of atom chips capable of trapping atoms < 1 µm away, thereby reducing both the size and power requirements of chip-trap potentials.

Acknowledgements

The existence of this thesis owes much to a number of people.

Bex and my family for their unwavering support.

Prof. Mark Fromhold as my principle supervisor who provided innumerable ideas, suggestions and insights.

Prof. Peter Krüger for much help, particularly regarding the practical aspects of BEC experiments and for steering the direction of the Landau work.

Prof. Andrea Trombettoni and Serena Fagnocchi for inspiration and guidance regarding the Landau investigations.

Cold atom theory colleagues and friends within the department for valuable discussions both on physics and life.

Contents

Chapter 1

BEC Theory

1.1 Historical background

All known particles fall into one of two categories, termed bosonic and fermionic. These tags relate to the branch of statistical mechanics, which describes the collective behaviour of bosonic and fermionic particles. Fermionic particles, or fermions, named after Enrico Fermi, obey Fermi-Dirac statistics [1, 2] and follow the Pauli-exclusion principle [3], namely that no two fermions may occupy an identical quantum state. Bosonic particles, or bosons, named after Satyendra Nath Bose, follow Bose-Einstein statistics [4]. In contrast to fermions, many bosons may occupy the exact same quantum state. Any boson, in the same quantum state as other bosons, becomes indistinguishable.

In both quantum mechanics and particle theory a fundamental quantity, termed *spin* (due to the conceptual analogy of a particle spinning around its own axis), is ascribed to particles. This is measured in units of the reduced Planck constant $\hbar$. Bosons

possess integer spin $S = 0, 1, 2, ...$ and Fermions half-integer spin $S = 1/2, 3/2, 5/2, ...$ Remarkably, the spin of an object is the sole quantity that determines whether the object is fermionic or bosonic.

Scientists soon realised that the study of pure collections of these basic objects offers a tool with which to observe and hopefully understand physics at a quantum level. Unfortunately, the world we live in conspires, through its immediately classical nature, to prevent us from easily studying quantum phenomena. Therefore, somewhat remarkably, much of the theoretical framework and predictions relating to the behaviour of quantum particles was developed well in advance of experimental observation. A key prediction in the bosonic field was initiated by a 1924 paper by Bose [5] describing photon statistics (photons fall into the bosonic class). Einstein, on receiving a copy of the paper for comments, extended the scope to include all non-interacting bosonic particles [6]. This work, which forms the basis of the field of Bose-Einstein statistics, predicted amongst other things that on lowering the energy of a system of bosons, generally achieved through lowering the kinetic energy of the system, increasing numbers of particles will occupy, or condense into, the lowest energy state of the system. As all the bosons are occupying the same quantum state, interacting with the environment in an identical fashion, they may, as a collection, be described by a single wavefunction, whose behaviour follows the laws of quantum rather than classical mechanics. This predicted object, a Bose-Einstein condensate (BEC), represented a new state of matter, which offered the unprecedented possibility of observing quantum behaviour in a macroscopic system. The race amongst experimentalists to observe

such a system began.

The major obstacle to observing a BEC is the fact that gases, on reduction of temperature, will liquefy or solidify before reaching the Bose-Einstein condensate phase. Once in the solid or liquid phase, it is impossible to undergo a phase transition to a BEC state because, with the higher density inherent to a solid or liquid phase, the interatomic interaction forces become too large to allow a macroscopic fraction of the particles to occupy the same quantum phase. Additionally, in the case of the solid phase, the ordering that occurs with this transition will also *freeze* the particles into a non-condensed state.

An exception to this situation is helium. As a noble gas, the interatomic interactions in helium are very weak, which means that at standard atmospheric pressure the atoms remain in the liquid phase all the way down to 0K. It should therefore come as no surprise that the earliest system to be recognised as having BEC characteristics was liquid helium-4. First produced in 1908 [7], it was seen to exhibit superfluid behaviour below a certain temperature, 2.17 K. This transition was explained by Fritz London in 1938, as resulting from the helium having entered the Bose-Einstein condensed phase [8]. This was later proved correct and much of the initial work and theory regarding Bose-Einstein condensates was developed around liquid helium-4.

Although the study of superfluid liquid helium-4 as a type of BEC represented an important milestone in the field, the interactions between liquid helium atoms are still sufficiently strong that less than ten percent of the atoms occupy the lowest energy state or BEC

phase. Thus, superfluid liquid helium-4 should be viewed more as a prototype BEC than a true BEC, in which the vast majority of the atoms in the system occupy the lowest energy state.

Over the following decades, magnetic trapping and evaporative cooling techniques, described later, were developed with the aim of creating a BEC of hydrogen atoms. However, it was the combination of these magnetic methods with the laser cooling techniques, to which alkali atoms are best suited, that finally led to the experimental observation of Bose-Einstein condensation. This was achieved in 1995 by a Colorado based group of Cornell and Wieman [9], swiftly followed by several others including Ketterle at MIT [10].

Following this breakthrough, with condensates now offering an *achievable* quantum research toolkit, the field of BEC research exploded, through the 1990s and into the current millenium. The current situation is that there are scores of quantum cold gas groups worldwide, working experimentally and theoretically. Research topics are diverse, ranging from answering fundamental questions, such as the nature of vortex formation [11], to looking at exotic situations, such as BECs in zero gravity [12].

An indication of the status of BEC research as one of the most exciting and important fields of modern physics is that the underlying experimental breakthroughs that led to their realisation resulted in not one, but two, Nobel prizes. The 1997 prize to Steven Chu, Claude Cohen-Tannoudji and William D. Phillips "for development of methods to cool and trap atoms with laser light" and the 2001 prize to Eric A. Cornell, Wolfgang Ketterle and Carl E. Wieman "for the achievement of Bose-Einstein condensation in dilute gases

of alkali atoms, and for early fundamental studies of the properties of the condensates" [13, 14]. Both of these prizes were awarded a remarkably short time (in Nobel prize terms) after the associated research. Confirming that achievement of Bose-Einstein condensation, represents a major milestone for science.

1.2 Analytical definitions

As mentioned in the previous section, a BEC is a collection of bosons that have condensed into the same quantum ground state. The mechanism by which this transition occurs can be derived, and the derivation process also gives us the opportunity to define several other useful quantities.

1.2.1 Transition temperature T_c

As a rough and ready indication of the presence of a BEC we can firstly look at what temperature we may expect centre-of-mass atomic wavefunctions to overlap. As a consequence of wave-particle duality, it is possible to ascribe an atomic wavelength to a particle. In the case of thermal particles, moving freely in a three-dimensional space, this wavelength is the thermal de Broglie wavelength [4],

$$\lambda = \sqrt{\frac{2\pi\hbar^2}{mk_BT}}, \tag{1.1}$$

where m is the mass of the particle, T the temperature and k_B is the Boltzmann constant. If this wavelength is longer than the mean

inter-atomic spacing in the system

$$\lambda = n^{-1/3}, \tag{1.2}$$

where n is the atom density, the individual atomic wavefunctions will begin to overlap and the atoms will have 'knowledge' of each other. By equating (1.1) with (1.2) we see that we can expect this to happen around a temperature

$$T_c = \frac{2\pi\hbar^2 n^{2/3}}{m k_B}. \tag{1.3}$$

This is a very simplistic approach, based on a consequence rather than the cause of BEC and, as such, overestimates T_c by, for example, a factor of $\sqrt{2}$ in the case of a uniform Bose gas in a box. It is, however, a useful starting point to give one a general feel for the physics before we make our description more accurate by bringing in system size and shape constraints as well as atom number and atom-atom interactions.

We start our more rigorous definition from the Bose distribution function [4], responsible for the initial prediction of the existence of BECs, which gives the mean number of particles in a quantum state n,

$$\overline{N}_n = \frac{1}{\exp([E_n - \mu]/k_B T) - 1} \tag{1.4}$$

where E_n is the energy of the state, T the temperature and μ the chemical potential of the system, which is itself a function of the particle number, N, and temperature T. The relationship between

μ, N and T is constrained by the condition

$$N = \sum_n \frac{1}{\exp([E_n - \mu]/k_B T) - 1}, \tag{1.5}$$

that the sum of the average number of particles in each mode must equal the total number of particles. In order to gain an insight into the condensation phenomenon, it is instructive to split the total number of particles into two parts: those in the groundstate, N_{gs}, and those in excited states , N_{ex}, which ensure that

$$N = N_{gs} + N_{ex}. \tag{1.6}$$

As discussed in the previous section, condensation coincides with a macroscopic occupation of the groundstate. However, rather than directly calculate the occupation of the groundstate, it proves easier to calculate the occupation of the excited states and then infer the groundstate population, N_{gs}, using the relation given by Eq. (1.6),

$$N_{ex} = N - N_{gs} = \sum_{n \neq 0} \frac{1}{\exp([E_n - \mu]/k_B T) - 1}. \tag{1.7}$$

With the semiclassical assumption that for a large system the spacings between energy levels become small, and the subsequent implication that the excitation energies are large compared to the level spacings, the summation can be replaced by an integral [15]

$$N_{ex} = N - N_{gs} = \int_0^\infty \frac{\mathrm{d}n_q}{\exp([E_n - \mu]/k_B T) - 1}. \tag{1.8}$$

We are currently working in terms of a quantum number, n_q, but by

rewriting in terms of energy using the relationship

$$dN = D(E)\mathrm{d}E, \tag{1.9}$$

where $D(E)$ is the density of states of the system, gives

$$N_{ex} = N - N_{gs} = \int_0^\infty \frac{D(E)\mathrm{d}E}{\exp([E-\mu]/k_BT) - 1} \tag{1.10}$$

in which the contribution from the zero-point energy has been ignored, i.e. we have set $E_0 = 0$. This assumption is valid for large N and thus consistent with our previous assumptions. If condensation occurs *below* a temperature that allows macroscopic occupation of the groundstate, it follows that above this temperature all the atoms may be accommodated in the excited energy levels and, equivalently, condensation occurs at the temperature at which this is no longer true. Therefore, the lowest temperature at which $N_{ex} = N$ is the definition which best suits our continuing derivation of the transition temperature T_c. On consideration of Eq. (1.5), it is apparent that the highest temperature for a given distribution occurs for $E_0 = \mu$. As we have already set E_0 to 0 we can use this fact to rewrite Eq. (1.10) at the critical temperature T_c giving,

$$N_{ex} = N = \int_0^\infty \frac{D(E)\mathrm{d}E}{\exp(E/k_BT_c) - 1}. \tag{1.11}$$

At this point, it is worth taking a moment to further consider the behaviour of the chemical potential μ. We know that at high temperatures the occupation of the groundstate $N_n(E_0) << 1$ and so, from Eq. (1.4), $\mu << E_0$. As the temperature lowers, μ ap-

proaches the value of E_0. At the critical temperature $\mu = E_0$, but at temperatures lower than T_c, μ may not drop below the value of E_0 because, from Eq. (1.4), the number of atoms in the groundstate, $N_n(E_0)$ would then become negative, which is clearly unphysical. Therefore we see that at all temperatures at and below the critical temperature, $T \leq T_c$, the chemical potential of the system remains fixed at $\mu = E_0 = 0$.

Having arrived at Equation (1.11), which expresses the critical temperature T_c in terms of energy, we can continue with the derivation of the transition temperature by using a density of states function, $D(E)$, appropriate to the system under consideration.

Condensate systems are commonly prepared using traps with a potential form which may be approximated, by that of a harmonic oscillator. In three-dimensions this is of the form,

$$V(x, y, z) = \frac{m}{2}(\omega_x^2 x^2 + \omega_y^2 y^2 + \omega_z^2 z^2). \tag{1.12}$$

We will choose this as the example in our continuing derivation of the transition temperature. The quantum energy levels of the harmonic oscillator Eq. (1.12) are [16]

$$E(n_x, n_y, n_z) = (n_x + \frac{1}{2})\hbar\omega_x + (n_y + \frac{1}{2})\hbar\omega_y + (n_z + \frac{1}{2})\hbar\omega_z \tag{1.13}$$

where n_x, n_y and n_z are quantum numbers corresponding to motion in the x, y and z directions respectively. The permissible values of these quantum numbers, $(i = x, y, z)$, are integer values greater or equal to zero $n_i \in \mathbb{Z} \geq 0$. The energy $\dfrac{\hbar\omega_i}{2}$ that remains for $n_x = n_y = n_z = 0$ is the zero-point energy. As already mentioned, for

a large system this zero-point energy may be ignored. Additionally, if the system is large the number of quantum states will high enough to represent the discrete quantum numbers n_i as a continuous variable.

Through these choices the total energy of the system, E, is now also a continuous variable. The volume of energy space containing states with energy less than E is then

$$V(E) = \int_0^E \left(\int_0^{E-E_x} \left[\int_0^{E-E_z-E_y} \mathrm{d}E_z \right] \mathrm{d}E_y \right) \mathrm{d}E_z, \tag{1.14}$$

where we have used the relationship $E = E_x + E_y + E_z$, where $E_i = n_i \hbar \omega_i$ to express the integral in terms of a coordinate system linked to the energy in each dimension. By dividing this total volume by the volume occupied by an individual state given, by Eq. (1.13), as $\hbar^3 \omega_x \omega_y \omega_z$ we obtain an expression for the approximate number of states below a given energy E,

$$N(E) = \frac{1}{\hbar^3 \omega_x \omega_y \omega_z} \int_0^E \left(\int_0^{E-E_x} \left[\int_0^{E-E_z-E_y} \mathrm{d}E_z \right] \mathrm{d}E_y \right) \mathrm{d}E_z. \tag{1.15}$$

Due to our choice of axes this integral is easily evaluated to give

$$N(E) = \frac{E^3}{6\hbar^3 \omega_x \omega_y \omega_z}. \tag{1.16}$$

We can use this with Eq. (1.9), re-expressed as

$$D(E) = \frac{\mathrm{d}N(E)}{\mathrm{d}E}, \tag{1.17}$$

to find the density of states for a harmonic oscillator

$$D(E) = \frac{E^2}{2\hbar^3\omega_x\omega_y\omega_z}. \tag{1.18}$$

This is the very quantity we need to continue with our derivation of the transition temperature. Equation (1.18) may be expressed in a more general form, applicable for a potential of arbitrary shape and dimension

$$D(E) = A_\alpha E^{\alpha-1}, \tag{1.19}$$

where A_α and α are constants. In the case of a three-dimensional harmonic oscillator, $\alpha = 3$ and $A_3 = \frac{1}{2\hbar^3\omega_x\omega_y\omega_z}$. Consequently, substituting Eq. (1.18) into Eq. (1.11) we get

$$N = \frac{1}{2\hbar^3\omega_x\omega_y\omega_z}\int_0^\infty \frac{E^2 \mathrm{d}E}{\exp(E/k_BT_c) - 1}. \tag{1.20}$$

Rewriting Eq. (1.20) in terms of the dimensionless variable, $x = \frac{E}{k_BT_c}$, along with the constants defined in Eq. (1.19), gives,

$$N = A_\alpha(k_BT_c)^\alpha \int_0^\infty \frac{x^{\alpha-1}\mathrm{d}x}{e^x - 1}, \tag{1.21}$$

a form which contains the standard integral

$$\int_0^\infty \frac{x^{\alpha-1}\mathrm{d}x}{e^x - 1} = \Gamma(\alpha)\zeta(\alpha), \tag{1.22}$$

where $\Gamma(\alpha)$ is the Gamma function and $\zeta(\alpha)$ the Riemann zeta function. Consequently at the critical temperature,

$$N = A_\alpha(k_BT_c)^\alpha\Gamma(\alpha)\zeta(\alpha), \tag{1.23}$$

which gives an equation for the critical temperature,

$$T_c = \frac{1}{k_B} \frac{N^{1/\alpha}}{[A_\alpha \Gamma(\alpha)\zeta(\alpha)]^{1/\alpha}}. \tag{1.24}$$

In the case of a three-dimensional harmonic oscillator, $\alpha = 3$, $A_3 = \dfrac{1}{2\hbar^3\omega_x\omega_y\omega_z}$, $\Gamma(3) = 2$ and $\zeta(3) \approx 1.202$. The critical temperature is therefore

$$T_c = 0.045 N^{1/3} (f_x f_y f_z)^{1/3}\, n\mathrm{K} = 0.045 N^{1/3} \overline{F}\, n\mathrm{K}, \tag{1.25}$$

where $\overline{F} = (f_x f_y f_z)^{1/3}$ is the geometric mean of the trap frequencies in Hz. In the case of a BEC with typical experimental parameters, $N = 10000$, $f_x = f_y = f_z = 50\,\mathrm{Hz}$, $\omega_{x,y,z} = 2\pi f_{x,y,z}$, gives $T_c \approx 50\,\mathrm{nK}$.

As another example, for the case of a uniform Bose gas in a three-dimensional box of volume V the constants of the system are [4], $\alpha = 3/2$, $A_{3/2} = (V m^{3/2})/(2^{1/2}\pi^2\hbar^3)$, $\Gamma(3/2) \approx 0.886$ and $\zeta(3/2) \approx 2.612$, which gives a critical temperature of

$$T_c \approx 3.31 \frac{\hbar^2 n^{2/3}}{k_B m}. \tag{1.26}$$

This is roughly half the value predicted by our initial simplistic calculation Eq. (1.3). Throughout the derivation we have frequently called on the fact that the system is large enough to be thought of as infinite, allowing us to ignore the zero-point energy. A more thorough treatment for a finite sized system not included here, reveals that the correction to the critical temperature is only of order 1% [4].

The equation for the critical temperature gives us a value at which condensation occurs. We may now also find the ratio of

condensed to non-condensed atoms at a given temperature $T < T_c$. To do this, we start with Eq. (1.10) which gives the number of atoms in excited states. As before, we know that at temperatures at or below the critical temperature, $\mu = E_0$, which, for a large system we may approximate by $E_0 = \mu = 0$. Using this fact and subsequent approximation, along with the general form for the density of states Eq. (1.19) and the introduction of a dimensionless variable $x = \dfrac{E}{k_B T}$ gives the equation,

$$N_{ex} = A_\alpha (k_B T)^\alpha \int_0^\infty \frac{x^{\alpha-1} \mathrm{d}x}{e^x - 1}, \tag{1.27}$$

which is strikingly similar to Eq. (1.21) and may be evaluated using the same standard definitions to give,

$$N_{ex} = a_\alpha (k_B T)^\alpha \Gamma(\alpha) \zeta(\alpha). \tag{1.28}$$

At $T = T_c$ we know that $N_{ex} = N$, so Eq. (1.28) at this temperature becomes,

$$N = A_\alpha (k_B T_c)^\alpha \Gamma(\alpha) \zeta(\alpha). \tag{1.29}$$

Dividing Eq. (1.28) by Eq. (1.29) gives the condensate fraction

$$\frac{N_{ex}}{N} = \left(\frac{T}{T_c} \right)^\alpha. \tag{1.30}$$

At a given temperature $T < T_c$ the number of condensed particles is

$$N_{gs} = N - N_{ex} = N \left[1 - \left(\frac{T}{T_c} \right)^\alpha \right], \tag{1.31}$$

a fraction that is slightly reduced if the derivation is done for a

finite system. Of greater impact to both the transition temperature and the condensate fraction is the effect of interactions between the bosons, discussed in the next section.

1.2.2 Including interactions

So far we have been considering the case of an ideal Bose gas, a model system in which the behaviour of individual atoms is unaffected by the presence of other atoms in the system. While this has been useful to gain an understanding of some of the key features of a Bose gas, such as transition temperatures, for a real Bose gas interatomic interactions exist and, crucially, drive much of the physics of the system. It is therefore vital to both understand these interactions and find a way to deal with them.

In studies of a quantum mechanical system perhaps the most useful thing to know is the relevant Hamiltonian operator, $\hat{H}$. This operator, acting on state Φ_S gives the energy eigenvalue, E_S, of the system via

$$\hat{H}\Phi_S = E_S\Phi_S. \tag{1.32}$$

Knowing the form of the Hamiltonian of a given system generally confers insight into both the equilibrium state and the time-evolution of the system. For most systems it is convenient to split the Hamiltonian in the form,

$$\hat{H} = \hat{T} + \hat{V} \tag{1.33}$$

where $\hat{T}$ and $\hat{V}$ are the operators corresponding respectively to kinetic and potential energy.

For a single particle the potential energy operator is simply

$$\hat{V} = V(\underline{\mathbf{r}}, t), \tag{1.34}$$

the local potential energy at time, t. The kinetic energy operator is related to the momentum of the particle,

$$\hat{T} = \frac{\hat{p}^2}{2m} = -\frac{\hbar^2}{2m}\nabla^2, \tag{1.35}$$

which makes use of the momentum operator,

$$\hat{p} = -i\hbar\nabla, \tag{1.36}$$

where ∇ is the gradient operator, with ∇^2 therefore giving the divergence of the gradient, known as the Laplacian. The Hamiltonian for a single particle can thus be expressed in the form,

$$\begin{aligned} \hat{H} &= \hat{T} + \hat{V} \\ &= -\frac{\hbar^2}{2m}\nabla^2 + V(\underline{\mathbf{r}}, t) \end{aligned} \tag{1.37}$$

which is known as the Schrödinger equation.

Similarly for many particles, N, we can write the Hamiltonian in the form

$$\hat{H}_{many} = \hat{T}_{many} + \hat{V}_{many} \tag{1.38}$$

The kinetic energy operator is simply given by the sum of the kinetic

energy operators for each of the N particles, i.e.

$$\begin{aligned}\hat{T}_{many} &= \sum_{n=1}^{N} \hat{T}_n \\ &= -\frac{\hbar^2}{2} \sum_{n=1}^{N} \frac{1}{m_n} \nabla_n^2, \end{aligned} \tag{1.39}$$

with the Laplacian evaluated for each particle depending upon its position.

The many particle potential operator, $\hat{V}_{many}$, is also easily defined, but contains terms which are difficult to work with. In the non-interacting case, which we have been studying to date, the potential energy term may also be written as a sum of the single-body, individual particles potential energy contributions, U_n, giving

$$\begin{aligned}\hat{V}_{many} &= \sum_{n=1}^{N} U_n \\ &= \sum_{n=1}^{N} U(\mathbf{r}_n, t). \end{aligned} \tag{1.40}$$

This allows us to write the Hamiltonian for a many body non-interacting system as

$$\begin{aligned}\hat{H} &= -\frac{\hbar^2}{2} \sum_{n=1}^{N} \frac{1}{m_n} \nabla_n^2 + \sum_{n=1}^{N} V_n \\ &= \sum_{n=1}^{N} \hat{H}_n, \end{aligned} \tag{1.41}$$

which is simply the sum of the single particle Hamiltonians for all the particles making up the system.

This form of a many body Hamiltonian is relatively simple to

deal with. However, on including interatomic interactions, it is no longer the case that the potential energy operator may be separated into a sum of individual single particle terms. Instead, it must either be included in the form

$$\hat{V}_{many} = U(\mathbf{r}_1, \mathbf{r}_2, \mathbf{r}_3, \ldots, \mathbf{r}_N, t), \tag{1.42}$$

a non-separable term that depends on the position of all of the particles at a given time. Or as a series of sums, representing interactions between increasing numbers of bodies, $U_2, U_3, \ldots U_n$,

$$\hat{V}_{many} = \sum_{i,j} U_2(\mathbf{r}_i, \mathbf{r}_j) + \sum_{i,j,k} U_3(\mathbf{r}_i, \mathbf{r}_j, \mathbf{r}_k) + \ldots. \tag{1.43}$$

Using this definition in Eq. (1.38) gives us the general Hamiltonian for a many body interacting system,

$$\hat{H} = -\frac{\hbar^2}{2} \sum_{n=1}^{N} \frac{1}{m_n} \nabla_n^2 + \sum_{i,j} U_2(\mathbf{r}_i, \mathbf{r}_j) + \sum_{i,j,k} U_3(\mathbf{r}_i, \mathbf{r}_j, \mathbf{r}_k) + \ldots. \tag{1.44}$$

Where the number of terms needed in $\hat{V}_{many}$ depends on the system in question.

This version of the many body Hamiltonian is significantly harder to work with, as the potential energy depends on the specific configuration of all of the particles in the system. In order to conserve total energy it follows that the kinetic energy also depends on the specific configuration. Thus any change in motion or energy of a particle will cause changes to every other particle. Calculation of these cross terms is in general problematic, particularly from a nu-

merical perspective. In some specific cases, for example through use of Monte-Carlo simulations for repulsive "hard-sphere" potentials, systems of up to 10^4 atoms [17] have been simulated directly from a full interacting many body Hamiltonian. Increases in computing power are also allowing brute force approaches to simulating more general systems, but these are still limited to atom numbers in the tens and hundreds . As the condensate behaviour we wish to study occurs in the realms of large particle numbers $N \sim 10^4 - 10^6$ pursuing this brute force approach is unwise for the foreseeable future. We therefore seek a Hamiltonian that encapsulates the interactions whilst being more tractable to current numerical approaches.

1.2.3 Scattering length and mean field theory

To do this we turn to a mean field approach/approximation. This general technique is often used when dealing with large N-body systems. The mean field approach is to replace an N-body system with a one body system containing a field which is chosen to approximate the combined effect of the interactions of all the other particles on that body. As well as hopefully reducing the analytical and numerical complexity of the system, this approach can also give a description of the system in terms of parameters which have readily understandable physical meanings. This mean-field approach was first applied to dilute Bose gases by Bogliubov in 1947 [18]. The mean field equation we will work towards is known as the Gross-Pitaevskii equation (GPE), a mean field Hamiltonian for BEC systems independently developed by Gross and Pitaevskii in 1961 [19, 20, 21].

For the systems under consideration, collections of neutral alkali

atoms, the main contribution to the interacting potential will be scattering events. A scattering event may, in the centre of mass frame, be expressed as the sum of an incoming plane wave e^{ikz} and the outgoing scattered wave $\Psi_{sc}(\underline{\mathbf{r}})$,

$$\Psi = e^{ikz} + \Psi_{sc}(\underline{\mathbf{r}}). \tag{1.45}$$

As we are working with a dilute system, throughout our derivation the scattered wave will assume the form of a spherical wave $f(\mathbf{k})\dfrac{e^{ikr}}{r}$ with an amplitude $f(\mathbf{k})$, where $\mathbf{k}$ specifies the wavevector of the scattered wave and r is the radial distance from the scattering event. Assuming spherical symmetry in the scattering process means that the scattering amplitude $f(\mathbf{k})$ will depend only on the angle θ between the directions of the particles' relative momentum before and after the scattering event,

$$\Psi = e^{ikz} + f(\theta)\frac{e^{ikr}}{r}. \tag{1.46}$$

If considering only two-body collisions, $f(\theta)$ approaches a constant, $-a$, termed the *scattering length*. In the low energy limit $k \to 0$ and Eq. (1.46) becomes,

$$\Psi = 1 - \frac{a}{r}. \tag{1.47}$$

One can evaluate the scattering cross section σ corresponding to this wavefunction [4] to find

$$\sigma = 4\pi a^2. \tag{1.48}$$

This expression shows the relationship between the scattering length

and the effective range of the interatomic potential, which is that of a hard sphere of radius a.

The scattering length a is the quantity used to represent the strength of interactions in the system we are dealing with. Through following a similar, though slightly more complex, derivation for a system in which there are only low momentum collisions between long-wavelength particles provides an effective interaction term

$$U_0 = \frac{4\pi\hbar^2 a}{m}, \tag{1.49}$$

related to the scattering length [4].

The Gross-Pitaevskii equation

We start the derivation of the GPE with the approximation that, in sufficiently dilute systems, only two-body collisions need including in the interaction potential. This allows us to rewrite the full interaction term (1.42) as an effective, contact potential

$$V_{eff} = U_0\delta(\mathbf{r} - \mathbf{r}'), \tag{1.50}$$

plus an additional term, $V(\mathbf{r})$, which represents any external potential. As our BEC is a dilute system comprising low momentum, long-wavelength particles in which two-body collisions dominate, the most appropriate form for U_0 is that presented in Eq. (1.49).

Using this form for the contact potential, the contribution to the total energy E of the BEC system is given by

$$V_{int} = U_0 n(\mathbf{r}), \tag{1.51}$$

where $n(\mathbf{r})$ is the condensate density. Using the relation $n(\mathbf{r}) = |\Psi(\mathbf{r})|^2$ gives

$$V_{int} = U_0 |\Psi(\mathbf{r})|^2 . \tag{1.52}$$

We can now write the many body interacting Hamiltonian in a mean-field form

$$-\frac{\hbar^2}{2m}\Psi(\mathbf{r}) + V(\mathbf{r})\Psi(\mathbf{r}) + U_0 |\Psi(\mathbf{r})|^2 \Psi(\mathbf{r}) = \mu\Psi(\mathbf{r}), \tag{1.53}$$

which is the *time-independent Gross-Pitaevskii equation*, where μ is the chemical potential of the system, discussed further in Section 1.2.4. This equation has the form of the time-independent Schrödinger equation for a single particle

$$-\frac{\hbar^2}{2m}\Psi(\mathbf{r}) + V(\mathbf{r})\Psi(\mathbf{r}) = E\Psi(\mathbf{r}), \tag{1.54}$$

with the addition of a non-linear mean-field term, $U_0 |\Psi(\mathbf{r})|^2 \Psi(\mathbf{r})$, which takes into account all of the interactions between particles. It is worth noting that the wavefunction, $\Psi(\mathbf{r})$, in the GPE (1.53) is a quantum wavefunction describing the full BEC system and it is this BEC wavefunction that acts as the single body in our one-body mean field approach.

There is also a corresponding equation,

$$-\frac{\hbar^2}{2m}\nabla^2\Psi(\mathbf{r},t) + V(\mathbf{r},t)\Psi(\mathbf{r},t) + U_0 |\Psi(\mathbf{r},t)|^2 \Psi(\mathbf{r},t) = i\hbar\frac{\partial\Psi(\mathbf{r},t)}{\partial t}, \tag{1.55}$$

the *time-dependent Gross-Pitaevskii equation*, again a generalisation of the Schrödinger equation with a non-linear interaction term. It is this time-dependent form that we use as the basis for simulations of

condensate dynamics.

This formalism immediately shows one of the many advantages of the mean field, Gross-Pitaevskii, approach to looking at a condensed system. Through using it we now have an equation that describes the behaviour of the BEC in terms of the behaviour of a single entity, $\Psi(\mathbf{r})$, the condensate wavefunction rather than N-coupled equations describing the behaviour of all N condensed atoms. Viewing the system in terms of the behaviour of this single, macro-wavefunction greatly simplifies many conceptual situations and also explains the reasoning behind likening a BEC to a *matter wave*.

Having achieved our goal of describing an ideal Bose gas system by an equation, the GPE, which describes and can be used to model, a condensate comprising Bose particles, we are now in a situation to use this equation to derive various quantities of note.

1.2.4 Chemical potential and healing length

The chemical potential, μ, of a system is a concept used in a variety of physical situations. It gives a measure of the amount of energy within the system. Values, or equations, describing the chemical potential of a system, are gained from the change in the total energy of the system, E, with changing particle number, N. The chemical potential is then given using the thermodynamic relation

$$\mu = \frac{\partial E}{\partial N}. \tag{1.56}$$

In a uniform Bose gas, the wavefunction of each particle is $\sqrt{n} = \sqrt{N/V}$, where, V, is the volume of the system. The interaction

energy between pairs of particles is U_0/V. There are $N(N-1)/2$ ways of arranging pairs of N bosons. The interaction energy of this system is thus given by,

$$E = \frac{N(N-1)}{2}\frac{U_0}{V} \approx \frac{1}{2}Vn^2U_0. \tag{1.57}$$

As there is no external potential and no net kinetic energy within the uniform system, this represent the total energy present and Eq. (1.57) can be put into the thermodynamic equation, Eq. (1.56), yielding

$$\mu = U_0 n. \tag{1.58}$$

This is the chemical potential of a uniform Bose gas.

For a non-uniform system, the path to the equation governing the energy and chemical potential is more complex and the full derivation is not included. It does, however, offer another approach with which to gain the GPE and so a summary of the key steps in its derivation is now offered. The energy functional [4], Eq. (1.59), now includes terms corresponding to the kinetic energy and external potential, as well as the interaction term, which can no longer be simplified through assumption of a constant density,

$$E(\Psi) = \int d\mathbf{r} \left[\frac{\hbar^2}{2m}\left|\nabla\Psi(\mathbf{r})\right|^2 + V(\mathbf{r})\left|\nabla\Psi(\mathbf{r})\right|^2 + \frac{1}{2}U_0\left|\nabla\Psi(\mathbf{r})\right|^4\right]. \tag{1.59}$$

In Eq. (1.59), $\Psi(\mathbf{r})$, is a single wavefunction representing the condensed state,

$$\Psi(\mathbf{r}) = N^{1/2}\phi(\mathbf{r}), \tag{1.60}$$

where the single particle wavefunction, $\phi(\mathbf{r})$, is normalised to 1.

The form of the condensate wavefunction, Ψ, is found by minimising the energy, Eq. (1.59), with respect to $\Psi(\mathbf{r})$ and its conjugate $\Psi^*(\mathbf{r})$, whilst ensuring that the total number of particles remains constant. This can be done through a Lagrange multiplier method, requiring $\delta E - \mu \delta N = 0$. In this case, μ is the Lagrange multiplier, which ensures the particle number remains fixed. Having done this, the condensate wavefunction can be shown to satisfy the GPE,

$$-\frac{\hbar^2}{2m}\Psi(\mathbf{r}) + V(\mathbf{r})\Psi(\mathbf{r}) + U_0 \left|\Psi(\mathbf{r})\right|^2 \Psi(\mathbf{r}) = \mu\Psi(\mathbf{r}). \tag{1.61}$$

The healing length of a condensate, ξ, is a useful measure of the distance over which a condensate stops being influenced by a localized perturbation, or the distance from a local disturbance that it will take a condensate to return its to bulk value. Consequently, ξ is a useful length scale for the system under consideration. It is determined by the competition between the kinetic energy of the particles

$$K.E. = \frac{\hbar^2}{2mr^2} \tag{1.62}$$

and the interaction term between them,

$$P.E. = nU_0. \tag{1.63}$$

In Eq. (1.62) and (1.63), r is a distance, n the BEC's density and U_0 the effective interaction term Eq. (1.49). The healing length ξ is defined as the length r over which these two terms are equal, i.e.

$$\xi^2 = \frac{\hbar^2}{2mnU_0} = \frac{1}{8\pi na} \tag{1.64}$$

where a is the scattering length.

To expand on this concept, if the spatial extent of an object or potential perturbation is $l < \xi$ then its impact on the condensate is expected to be limited as the energy associated with the object is low compared to the kinetic energy of the system. Equivalently, if $l > \xi$, one would expect the perturbation to influence the condensate and this effect will extend over a distance $d \sim \xi$.

Thomas-Fermi approximation

The form of the full GPE can be difficult to probe analytically. It is therefore instructive to consider approximations that simplify the GPE, whilst still providing useful observations. Perhaps the most useful of these approximations is the Thomas-Fermi approximation, described below.

Harmonically (or similarly) trapped, repulsive condensates containing many atoms, represent a large proportion of BEC experiments. If these systems are at rest, or only moving with low velocity, there is little kinetic energy present. In this case, the potential energy term dominates the GPE. Within this regime, the case can be made to neglect the effect of the kinetic energy term. Rewriting the GPE, Eq. (1.53), omitting the kinetic energy term gives the Thomas-Fermi approximation,

$$\left[V(\mathbf{r}) + U_0 \left|\Psi(\mathbf{r})\right|^2\right] \Psi(\mathbf{r}) = \mu\Psi(\mathbf{r}), \tag{1.65}$$

where μ is the chemical potential. This approximate form of the

GPE has an analytical solution,

$$n(\mathbf{r}) = |\Psi(\mathbf{r})|^2 = [\mu - V(\mathbf{r})]/U_0, \tag{1.66}$$

for $\mu > V(\mathbf{r})$, and $\Psi = 0$ for $V(\mathbf{r}) > \mu$. Having made the Thomas-Fermi approximation, we immediately and easily gain a useful physical quantity: the extent of the condensate cloud. This is given by the area bounded by the curve

$$V(\mathbf{r}) = \mu. \tag{1.67}$$

In the case of a harmonic oscillator trap, the potential is of the form,

$$V_i(\mathbf{r}) = \frac{m\omega_i^2 x_i^2}{2}, \tag{1.68}$$

for a given axis, i. One may extract the spatial extent, R_i, of the condensate, along that axis, by putting Eq. (1.68) into Eq. (1.67), to give,

$$R_i^2 = \frac{2\mu}{m\omega_i^2}. \tag{1.69}$$

The constraint that the total number of particles in the condensate, N, is fixed can be expressed by the normalisation condition,

$$N = \int \mathrm{d}\mathbf{r}\, |\Psi(\mathbf{r})|^2 . \tag{1.70}$$

Use of this equation, along with the solution of the Thomas-Fermi approximation, Eq. (1.66), for the harmonic oscillator potential given by Eq. (1.68), allows us to gain an expression linking the number of

atoms, N, to the chemical potential, μ:

$$N = \frac{8\pi}{15}\left(\frac{2\mu}{m\overline{\omega}^2}\right)^{3/2}\frac{\mu}{U_0}. \tag{1.71}$$

In Eq. (1.71), $\overline{\omega}$ is the geometric mean trap frequency, $\overline{\omega} = (\omega_x\omega_y\omega_z)^{1/3}$. Equation (1.71) can also be solved for the chemical potential, μ,

$$\mu = \frac{15^{2/5}}{2}\left(\frac{Na}{\overline{a}}\right)^{2/5}\hbar\overline{\omega}, \tag{1.72}$$

where a is the scattering length and

$$\overline{a} = \sqrt{\frac{\hbar}{m\overline{\omega}}}. \tag{1.73}$$

In condensate systems where $\frac{Na}{\overline{a}} \gg 1$, the Thomas-Fermi approximation offers an excellent tool to gain analytical insight into their properties. It is also of use in comparison with GPE results. In appropriate cases, the difference between the Thomas-Fermi approximation and the results of a GPE simulation, gives detail regarding the effect of kinetic energy on the properties of the condensate.

1.2.5 Reduced dimensionality

Continuing developments in BEC trap design allow increasing control over condensate shape. Of particular interest to us is the case where one, or more, of the dimensions are strongly confined. For sufficiently strong confinement, the modes available to the condensate, in the confined direction may be suppressed. The condensate dynamics are then dominated by the less strongly confined directions and the

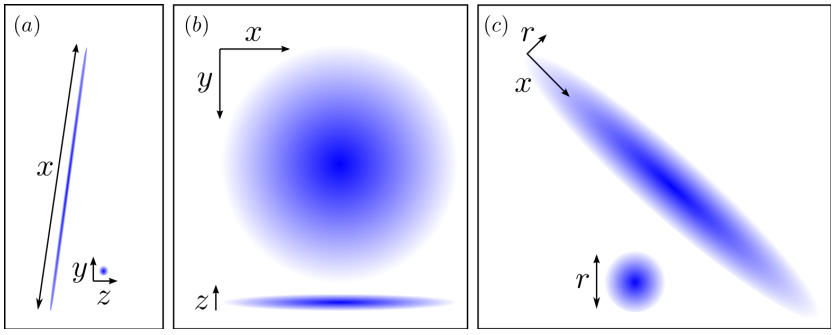

Figure 1.1: (a) One dimensional *cigar* shaped condensate (b) Two dimensional *pancake* shaped condensate (c) Axially symmetric condensate. In each case, the grey scale images show the atom density profiles in directions of both weak and strong confinement.

condensate becomes a reduced dimension, $d < 3$, system. Figure 1.1 shows common forms of these reduced dimensional condensates, The reduced dimensionality has associated consequences, discussed in this section.

We base our discussion on the one dimensional case, used most extensively within this thesis. The first priority is to establish the validity of the claim to be in a reduced dimensional regime. That only the groundstate mode has appreciable occupation in a confined dimension can be summarised by the condition,

$$\mu, kT \ll \hbar\omega_{\perp} \tag{1.74}$$

where $\omega_{\perp}$ is the trapping frequency in the confined dimension, assumed to be harmonic. As we are working with the zero-temperature, Gross-Pitaevskii model, the relevant energy scale is in fact just the chemical potential, μ and the condition for reduced dimensionality is

$$\mu \ll \hbar\omega_{\perp}. \tag{1.75}$$

The density profile and behaviour of the condensate cloud in the strongly confined dimensions is effectively *frozen* into the groundstate of the trap in that dimension. It is therefore useful to reformulate the GPE, used to model condensate dynamics, in terms of a one dimensional line density, n_{1d}, and associated one dimensional interaction term, g_{1d}, which satisfy

$$\mu = g_{3d}\, n_{3d} = g_{1d}\, n_{1d}, \tag{1.76}$$

where n_{3d}, g_{3d} are the three dimensional density and interaction term respectively. Equation (1.49), reproduced here defines g_{3d} as

$$U_0 = g_{3d} = \frac{4\pi\hbar^2 a}{m}. \tag{1.77}$$

If operating in a one dimensional regime, the density profile of the unconfined, x direction is independent of the *frozen*, density profile of the confined y and z directions, i.e.

$$n(x, y, z) = n(x)\, n(y, z). \tag{1.78}$$

In the case of a harmonic potential in the strongly confined directions, the density profile in these dimensions will be Gaussian. In the case of equal confinement along the y and z axis the density is given by,

$$n(y, z) = e^{-\frac{(y^2 + z^2)}{2a_\perp^2}}. \tag{1.79}$$

With $a_\perp$ the extent of the Gaussian groundstate,

$$a_\perp = \sqrt{\frac{\hbar}{m\omega_\perp}}. \tag{1.80}$$

Inserting Eq. (1.79) into Eq. (1.78) and integrating over the confined dimensions gives

$$\begin{aligned} n_{1d} &= \int n_{3d}(x,y,z)\,\mathrm{d}y\,\mathrm{d}z \\ &= n_0(x)\int e^{-\frac{(y^2+z^2)}{2a_\perp^2}}\,\mathrm{d}y\,\mathrm{d}z \\ &= n_0(x)\,2\pi a_\perp^2. \end{aligned} \tag{1.81}$$

Here $n_0(x)$, is the peak density along the unconfined dimension. Equation (1.81) may be rearranged to give the 3d density in the case of a 1d condensate,

$$n_0(z) = \frac{n_{1d}}{2\pi a_\perp^2}, \tag{1.82}$$

which can then be used in Eq. (1.76), to derive a form for the 1d interaction term, g_{1d}, in the following way

$$\begin{aligned} g_{3d}\,n_{3d} &= g_{1d}\,n_{1d} \Rightarrow \\ \frac{4\pi\hbar^2 a}{m}\frac{n_{1d}}{2\pi a_\perp^2} &= g_{1d}\,n_{1d} \Rightarrow \\ g_{1d} &= \frac{2\hbar^2}{m}\frac{a}{a_\perp^2}. \end{aligned} \tag{1.83}$$

From the reduced dimensionality condition Eq. (1.75) and our newly derived expression for the interaction strength in one dimension,

Eq. (1.83), we also gain an interesting constraint on the $1d$ density,

$$\begin{aligned} \mu = g_{3d}\, n_{3d} = g_{1d}\, n_{1d} &\ll \hbar\omega_\perp \\ \frac{2\hbar^2 a}{m a_\perp^2} n_{1d} &\ll \hbar\omega_\perp \\ n_{1d} &\ll \frac{1}{2a}, \end{aligned} \tag{1.84}$$

which is independent of the perpendicular trapping geometry.

1.3 Superfluidity

Superfluidity describes a quantum state of matter, which behaves like a fluid. However, in contrast to a *normal fluid* a *superfluid*, flows without friction as well as exhibiting several other interesting properties on excitation and during breakdown, as discussed later.

Originally observed in 1937 in low-temperature helium systems [22, 23], superfluidity is now acknowledged to manifest, in some form, for any macroscopic system placed in an environment, normally low temperatures, in which quantum laws govern the behaviour of the system [24]. It should therefore come as no surprise that BECs exhibit superfluid characteristics, relevant details of which are described below.

1.3.1 Frictionless flow

Frictionless flow, a result of a superfluid having zero viscosity, produces a range of interesting effects. In the case of superfluids such as helium, perhaps one of the most unusual consequences of this zero viscosity is the tendency for the superfluid to flow out of any

unenclosed container. Since there is no friction, the surface tension between the container's walls and the superfluid is sufficient to *pull* the superfluid up the walls and out of the container.

As condensates are not held in physical traps, this effect does not concern us. Of more relevance, is how a BEC's superfluid nature, influences its interactions with its potential landscape. Imagine an object being moved through the condensate. This could be an actual physical object, or a disturbance in the external potential, $V(r)$, created through use of an additional electric or magnetic field. Obviously this set up is equivalent to a moving condensate passing a stationary object. Whilst the condensate is in a superfluid regime, the lack of friction allows it to smoothly deform around the object without excitation.

The resistance of the BEC to excitation, whilst in the superfluid regime gives experimental advantages. It allows smooth manipulation of the condensate, in the knowledge that it will return to its initial state, on removal of the perturbation. Of greater interest to us, within this thesis, is the behaviour of a BEC as you manipulate its environment is changed to take it out of the superfluid stage, into a region where perturbing potentials will cause excitations and possibly break up the condensate.

1.3.2 The Landau criterion

When a superfluid system passes an obstacle with increasing velocity, it does not remain superfluid indefinitely. Above a certain velocity, excitations are created. The velocity at which this happens, corresponds to the point at which the moving superfluid system contains

enough energy to create the simplest excitation of the systen. This criterion was originally proposed by Landau [25] and is thus known as the Landau criterion. The speed to which it relates, is termed the Landau, or Landau critical, velocity, v_c^L.

We now derive this velocity for a condensate system following the approach of [4].

Consider a system in which an obstacle moves through a condensate with energy, E, at a constant speed, v. If one moves to another frame of reference, the energy of the system is given, through a Galilean transformation, by

$$E(\mathbf{v}) = E - \mathbf{p}\cdot\mathbf{v} + \frac{1}{2}Mv^2 \tag{1.85}$$

where, $\mathbf{p}$, is the condensate momentum and $M = Nm$ the total mass of the system.

Therefore, in a frame that moves with the obstacle, through a stationary condensate, $E = E_0$, $\mathbf{p} = 0$, with no excitations, the system energy is

$$E(\mathbf{v}) = E_0 + \frac{1}{2}Nmv^2. \tag{1.86}$$

The presence of excitations modifies this energy. The system energy for a single excitation with energy, ϵ_p and momentum, $\mathbf{p}$, becomes

$$E(\mathbf{v}) = E_0 + \epsilon_p + \mathbf{p}\cdot\mathbf{v} + \frac{1}{2}Nmv^2. \tag{1.87}$$

Comparing Eq. (1.87) with Eq. (1.86) one sees that the difference in energy between a system with, and without, an excitation is, $\epsilon_p + \mathbf{p}\cdot\mathbf{v}$. In the frame of a static obstacle, the obstacle is unable to transfer energy to the condensate. The speed at which an excitation

forms is thus given when the phase velocity of the excitation equals the velocity of the fluid,

$$v = \frac{\epsilon_p}{p}. \tag{1.88}$$

A process analogous to the Cherenkov effect, which occurs when a charged particle passes through a medium, with a velocity greater than the phase velocity of excitations in the medium. This causes the blue glow of nuclear reactors amongst other phenomena.

The minimum velocity at which one will create an excitation is therefore given by

$$v_c^L = min\left(\frac{\epsilon_p}{p}\right), \tag{1.89}$$

the *Landau critical velocity*. At speeds under this value, the condensate, on encountering an obstacle, behaves like a superfluid, with no excitations created. Above this speed, excitations will start to be created, degrading the superfluid flow characteristics.

This equation is of a general form for any superfluid. To gain an equation for a specific superfluid, for example a condensate, requires a consideration of the excitation energy spectrum of that system. This can be done through hydrodynamic or microscopic (as originally done by Bogoliubov) theory. For a condensate at small momentum, the spectrum is a linear function of momentum and is given by the equation

$$\epsilon_p \simeq \sqrt{\frac{nU_0}{m}}p. \tag{1.90}$$

The Landau critical velocity of a uniform Bose gas is therefore

$$v_c^L = \sqrt{\frac{nU_0}{m}}. \tag{1.91}$$

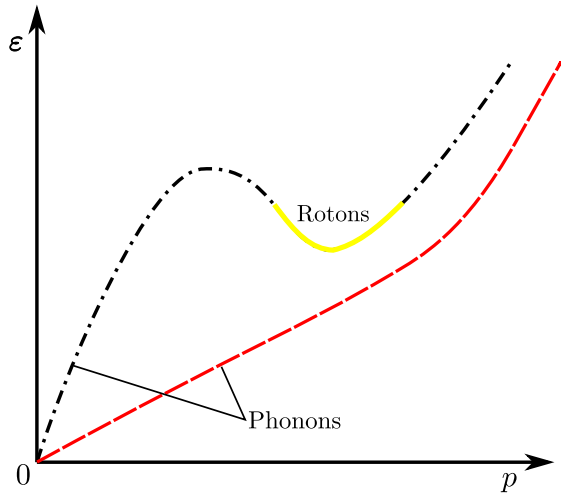

Figure 1.2: Example excitation spectrums, at low energies, for a Bose gas (red dash) and helium-4 (black dot-dash). Both show a linear area corresponding to phononic excitations, the helium-4 spectrum also contains a dip (yellow), not present in the Bose gas spectrum. This corresponds to the roton excitations which are the first excitations created in a helium-4 system.

The linear, sound-like, nature of the excitation spectrum tells us that the first excitations produced, will be long wavelength, phononic excitations. These manifest as a travelling disturbance in the density of the condensate. This is in contrast to the archetypal superfluid, Helium-4. The strong correlations present in Helium-4, creates an excitation spectrum which also contains a dip, rather than the simpler linear spectrum of a Bose gas. Therefore the first excitations created in superfluid helium are of a different form and are called rotons. The differing forms of these excitation spectra are shown in Figure 1.2.

Having talked about the nature of the elementary excitations within condensates (phonons), we now briefly cover the two other notable forms of excitations one observes within condensates, namely *solitons* and *vortices*.

Solitons

The non-linearity of the GPE, our main tool for stufy of condensate behaviour, limits analytical analysis of excitations. The time-dependent GPE does, in fact, have analytical solutions for a system with excitations. The excitations, known as *solitons*, present as localised disturbances in density. *Soliton*, or *Solitary wave* disturbances travel through the condensate without change in form (neglecting their breakdown behaviour discussed later). In this respect, their behaviour is in fact similar to that of a particle moving through a medium. They are in fact used as analogues to particles in some experiments.

Perhaps unsurprisingly, as the only analytical solution to the non-linear GPE, it is the non-linearity of the medium that gives rise to the stable existence of solitons. The interaction term balances the kinetic term, which would otherwise cause the disturbance to spread/disperse.

For a condensate with attractive interactions, the solitons present as positive disturbances to the density, $n_{sol} > n_{bulk}$ and are known as *bright* solitons. In the more commonly-used repulsive regime, the solitons take the form of density depressions, $n_{sol} < n_{bulk}$, called *dark* solitons. These are then further split into *black* solitons, in which the local density drops to zero, and *grey* solitons where the density drops to a non-zero value.

For a one dimensional condensate, with repulsive interactions, the density profile, with a grey soliton present is [4],

$$n(x,t) = n_{min} + (n_{bulk} - n_{min}) \tanh^2 \left(\frac{x - v_x t}{\sqrt{2}\xi'} \right). \tag{1.92}$$

Here, ξ' is the width of the soliton, which also depends on the soliton's velocity via the relation

$$\xi' = \frac{\xi}{(1-(v_x/v_c^L)^2)^{1/2}}, \tag{1.93}$$

where ξ is the healing length, Eq. (1.64), and v_c^L is the speed of sound or Landau velocity for a uniform gas, as in Eq. (1.89). The velocity of the soliton, is related to its depth through,

$$\left(\frac{v_x}{v_c^L}\right)^2 = \frac{n_{min}}{n_{bulk}}. \tag{1.94}$$

As velocity relates to phase gradient, we can also see that the phase change, $\Delta\Phi$, across the soliton satisfies,

$$\frac{v_x}{v_c^L} = \cos\left(\frac{\Delta\Phi}{2}\right) = \sqrt{\frac{n_{min}}{n_{bulk}}}. \tag{1.95}$$

From Equations (1.94) and (1.95) we learn that a black soliton, which has, $n_{min} = 0$, is stationary, $v_x = 0$, with a $\Delta\Phi = \pi$ phase change across it.

In the case of a one dimensional, uniform condensate, solitons are stable indefinitely. However in higher dimensions and non-uniform systems, this is no longer true. As the speed and shape of a soliton depends on the local speed of sound, if this is non-uniform, different parts of the soliton move at different speeds. This causes *refraction* of the soliton and eventually splitting. This breakdown mechanism is known as the *snake instability*.

Vortices

The other topological defects commonly observed within condensates are vortices. As mentioned when discussing phase imprinting in Section 2.4, the velocity of the condensate, Equation (2.8), reproduced here,

$$\mathbf{v} = \frac{\hbar}{m}\nabla\phi, \tag{1.96}$$

is related to the the phase. This has a profound consequence in relation to rotational flow. As the phase, ϕ, in Eq. (1.96) is scalar, it follows that

$$\nabla \times \mathbf{v} = 0. \tag{1.97}$$

This means that unless the phase contains a singularity, the velocity field is irrotational.

If one takes a closed contour around a point of the condensate, in order that the wavefunction is single-valued everywhere, the change in phase of the wavefunction must be,

$$\Delta\phi = \oint \nabla\phi \cdot d\mathbf{l} = 2\pi l, \tag{1.98}$$

an integer, l, multiple of 2π. From Equations (1.96) and (1.98), we can calculate the circulation around the same contour,

$$\Gamma = \oint \mathbf{v} \cdot d\mathbf{l} = \frac{\hbar}{m} 2\pi l = l\frac{h}{m}. \tag{1.99}$$

In the case where $l = 0$ there is no rotation and no vortices. For $l \neq 0$, the contour necessarily encloses a singularity, a *vortex*, around which the condensate rotates. At this point the wavefunction vanishes so it can be thought of as being somewhat like the behaviour

of a whirlpool in water. However, in marked contrast to classical systems, the rotation within the system is quantised in units of $\frac{h}{m}$.

Angular momentum can be imparted to a condensate system in a variety of ways, commonly through rotation of the confining trap or 'stirring' with a laser. Vortices can also form via the break down of solitons. In this way, single and multiple vortices, with varying values of quantised rotation, have been created and observed in condensates, including the observation of vortex lattice formation in multiple vortex situations [26]. Unlike solitons, vortices remain stable in a wide range of experimental situations.

Chapter 2

Experimental considerations

The numerical simulations within this work are designed to represent physically achievable experimental situations, albeit ones that may be difficult to implement. It is therefore important to have a grasp of the techniques available to experimentalists to ensure that the theoretical situations are constructed with physically realistic parameters. This section explores experimental methods, from the initial cooling and trapping techniques, the development of which were Nobel prize winning, and also the key breakthroughs that of enabled actual BEC experiments to take place. We then move to look at the various ways in which BECs may be manipulated. Finally, we outline the measurement techniques and their limitations, which constrain the size of effects that can be realistically detected. Obviously, an understanding of these various experimental considerations also leads to a greater awareness of the areas in which numerical simulations are most advantageous in probing BEC behaviour.

2.1 Cooling

As discussed in Section 1.1, traditional refrigerative cooling techniques are insufficient for creating BECs for two reasons. Firstly, the temperatures required for condensation, being in the nano-Kelvin range are too low for any previous refrigeration techniques. Secondly, such techniques are fundamentally unsuitable, even as an intermediary stage, as they require a physical interface between the refrigerant and the matter being cooled. To work, this requires the matter being cooled to have a density so high that the system will inevitably condense from the gas phase to the liquid/solid phase. As mentioned in Section 1.1, this prevents the possibility of a subsequent transition to the Bose condensed phase.

A different approach was therefore needed. The successful method was facilitated by the development of laser physics. Laser devices employ optical amplification of light through stimulated emission of photons, which results in the emission of highly coherent light, both spatially and temporally. Although the theoretical framework underpinning lasers was developed in 1917 by Einstein [27], it took until the 1960s for devices to be created that utilised these principles. The development and refinement of laser devices have opened up wide ranging applications and possibilities across all aspects of physics and, in fact, life in general. The concept of their use to enable the cooling of gaseous atoms was first suggested in 1975 [28, 29] through the method described below.

The first cooling stage is done using a *Zeeman slower*, a laser directed at a beam of hot, gaseous atoms. Radiation pressure acts to reduce the atoms' kinetic energy and thus temperature. Doppler

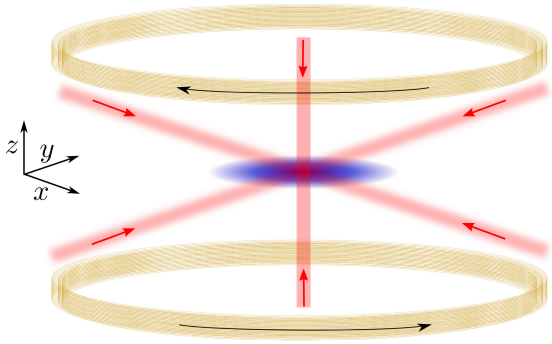

Figure 2.1: Schematic diagram of s magneto-optical trap (MOT) setup as used for cooling and trapping of BECs. Red lines indicate laser light orientated orthogonally in the x, y and z directions. Black arrows show direction of the current flow in the coils, which create the magnetic trap discussed in Section 2.2.

effects, which change the frequency of the laser as viewed in the rest frame of the slowing atom, complicate the procedure. These are countered through the application of an inhomogeneous magnetic field. This inhomogeneous magnetic field changes the atoms' energy levels, which is known as the Zeeman effect. The field is carefully chosen such that the change in energy levels exactly counters the Doppler effects, which act to change the frequency of the laser seen by the slowing atom. In this way, the atom is at resonance with the laser throughout the slowing process and will continue to be slowed, or equivalently, cooled. Through use of a Zeeman slower, temperatures of a few Kelvin can be achieved.

The second stage is based around the Doppler effect and is thus termed Doppler cooling. One starts by matching a particular electronic transition $|g\rangle \rightarrow |e\rangle$, within an atom with an appropriate laser, which is chosen so as to be red detuned with respect to the electronic transition.

If the laser is pointing in the $-z$ direction, the Doppler effect

means that an atom moving toward the laser light source will see the frequency up-shifted towards the transition, thus increasing the chance of electronic excitation through absorption of a photon. After absorption of the photon, the atom will subsequently emit a photon in a random direction. Each absorption process results in a loss of momentum of the atom in the z direction. Although the emission process increases the momentum of the atom, the direction of the increase is random and thus the net result is a decrease in the speed of the atom in the z direction. Through an appropriate arrangement of six counter-propagating lasers, such as the one shown in figure 2.1, it is possible to produce a net decrease in momentum in all directions. Unless the atom is almost stationary, at which point the Doppler effect becomes negligible, the detuning and Doppler effect ensure that an atom, whose momentum has been decreased by one laser, is not going to have it increased by the counter propagating laser. The presence of a harmonic magnetic trapping field, which will be discussed shortly, can aid this process. The change in the atoms excitation energy levels, as they move away from the magnetic trap centre means the atom will preferentially absorb light from a laser source pointing back towards the trap centre, assisting the cooling and and trapping process.

In this way, the mean kinetic energy and associated temperature of the atom can be reduced. The lowest temperature, $T_{doppler}$, that can be attained by this process is associated with the lifetime, Γ_e, of the excited state

$$kT_{doppler} = \frac{\hbar\Gamma_e}{2}. \tag{2.1}$$

For the alkali atoms used in BEC experiments, this temperature is

in the hundreds of micro Kelvin range. In the case of sodium atoms, using the transition between the 3P and 3S levels, $T_{doppler} \sim 240\mu$K.

Although the atoms are, on average, stationary, having reached a point at which they are equally likely to absorb a photon from either of the counter propagating beams, they undergo a random walk, with a kinetic energy and temperature still too high to allow condensation. The next, and final, stage of laser cooling is known as Sisyphus cooling. Again, counter propagating lasers are used, but this time they are set to have orthogonal polarization. The periodic light field created causes shifts in the energy of the magnetic groundstate substates and, additionally, pumps transitions between them. The effect is that as an atom, undergoing its random walk, moves within the field structure, it is forced to climb potential hills, losing kinetic energy. As the atom reaches the top of a potential hill, it is then pumped into a lower potential energy substate, with a net kinetic energy loss. This technique moniker links to the Greek legend of Sisyphus, a king punished by being given the task to roll a boulder up a hill, only for it to always fall to the bottom as it neared the summit. This method, which represents the limits of laser cooling, is limited only by the energy of a single photon recoil event and allows temperatures of $\sim 1\mu$K to be reached. Crucially, however, all three stages of laser cooling *preserve* the low density nature of the initial hot gas of atoms, preventing unwanted condensation into a liquid phase.

To reduce the temperature by the final amount required for condensation we use the principle of *evaporative cooling*. A system at a given temperature is, in fact, constructed from a collection of atoms

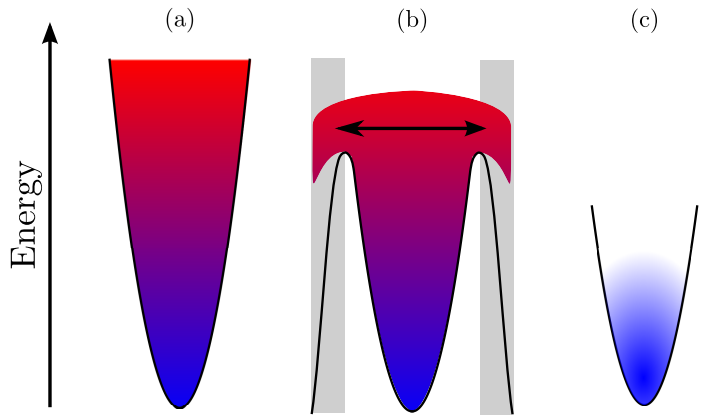

Figure 2.2: Evaporative cooling. After collecting the laser cooled gas (a), an rf-field (grey) is applied to the edges of the trap allowing high energy (red) atoms to escape (b). The remaining atoms re-thermalise at a cooler temperature allowing Bose-Einstein condensation to occur (c).

with energies given by the Maxwell-Boltzmann distribution for that temperature, which is proportional to $\exp(-\epsilon/kT)$. The fact that a range of energies is present is used to enable cooling. The cloud of atoms, cooled through the laser cooling techniques described above, is held in a magnetic trap constructed using principles described in the following section. One then lowers the sides of the trap, as shown in figure 2.2, usually through local application of an rf-field, which flips atoms from a trapped to an untrapped state. In this way, atoms possessing a high energy will escape and the remaining atoms will re-thermalise at a new lower average energy. Careful extension of this process provides the key to unlocking nano-Kelvin temperatures and condensation.

It should also be mentioned that there is a requirement throughout experimental work that processes take place within a vacuum sufficiently high to prevent unwanted collisions and at densities within

a given range. Elastic collisions between condensate atoms are necessary during the cooling process, as a mechanism for thermalisation of the system. Inelastic collisions on the other hand have unwanted effects. During an inelastic collision, the particle's state may be changed to an untrapped state, it may be ejected from the trap kinetically or even involved in a molecule forming process. All of these events are damaging to the experimental procedure.

To minimise these elastic collisions two criteria must be followed. Firstly the density of the system must be kept sufficiently low, $n < 10^{14}\text{cm}^{-3}$, that 3-body collisions are rare. Secondly BEC experiments are conducted within vacuum chambers to minimise collisions with other particles within the experimental chamber. To ensure that the collision rates with other particles are lower than the thermalisation rate and experimental timeframe, requires a vacuum that will restrict unwanted collisions between the condensate and particles within the chamber to a rate of less than one per minute. This requires a vacuum of the order $10^{-10} - 10^{-11}$ mbar.

The vacuum requirement provides an additional practical challenge in ensuring that the various necessary components do not interfere with each other or with the optical access that is required for condensate imaging and laser input.

2.2 Trapping

In order to understand the experimentally-achievable parameters used in our simulations, in this section we briefly examine the two main methods used by experimentalists to trap condensates.

Magnetic trapping is the first technique whose principles we will outline. This takes advantage of the potential created by the interaction of the atom's magnetic dipole moment, $\boldsymbol{\mu}_F$, for quantum state F, with an external field $\mathbf{B}(\mathbf{r})$. Classically the interaction energy is given by,

$$V_F = -\boldsymbol{\mu}_F \cdot \mathbf{B}(\mathbf{r}). \tag{2.2}$$

The quantum mechanical energy levels of an atom in the field are given by

$$E_{m_F} = g_F m_F \mu_B B, \tag{2.3}$$

where g_F is the Landé g factor and μ_B the Bohr magneton. Therefore an atom in a state with a negative dipole moment will seek low-field regions (*low field seeker*) whereas one with a positive dipole moment will seek high field regions (*high field seeker*). Usefully, magnetic dipole moments may be manipulated through addition of a laser light field.

Maxwell's equations forbid the creation of a local maximum in a magnetic field but not the creation of a local minimum [30, 31]. Therefore, one is constrained to construct field profiles containing a minimum with which to contain a condensate comprising low field seeking atoms. There exists a menagerie of magnetic atom traps, each with their own advantages and disadvantages. For our purposes we will divide them into two classes. The first class of traps we will consider use large scale coil and wire structures external to the experimental chamber. Much of the design groundwork for these systems was done before the advent of BECs, with the aim of providing systems to contain hot plasmas. The second type of trap

uses small scale structures housed on semiconductor chips, termed *atom chips*, which are placed in close proximity to the BEC.

Magnetic fields produced by structures external to the vacuum chamber were the first to be used in relation to BEC trapping. There are a variety of different coil/wire configurations that can be used. The simplest configuration involves using a pair of coils, with the current flowing in alternate directions. This produces a quadrupole-like field profile, with the field vanishing at a point. Near this point, the field profile approximates that of a harmonic trap.

The main problem encountered with this class of magnetic traps is that a moving atom will experience a time dependent magnetic field. This will induce transitions into untrapped states. These unwanted transitions become greater when $\mu_B B$ is small. Therefore, the zero field point at the trap's centre acts as a hole for trapped atoms, limiting storage times.

As a result, most other external structures used are modifications to this simple coil design and aim to remove the zero field point. This can be done most simply with an additional bias field to plug the hole, or through use of a laser light field plug. Use of an additional rotating, spatially uniform, magnetic field creates a trap which, on time averaging, contains no zero. This is known as a time-averaged orbiting potential (TOP) trap. In one of the most successful and popular methods, termed an Ioffe-Pritchard trap, the current flows the same way in both of the coils and Ioffe bars (conductors parallel to the symmetry axis) thereby creating a highly adjustable trap profile, with a non-zero field minimum.

In order to continue the development of the BEC research field,

increasingly complicated experimental set ups are desired. Using structures external to the vacuum chamber is, in general, limited to the creation of slowly-changing potentials, both in time and space. A solution to creating quickly-varying potentials, is to create the magnetic field within the vacuum chamber, in close proximity to the condensate. This is done by mounting conductors on a semiconductor surface and the resulting devices are collectively known as *atom chips*. One common form of atom chip trap is the *z-trap* shown in Figure 2.3.

This approach allows one to have field profiles which, due to the close proximity of the condensate, vary on a length scale limited solely by the fabrication process of placing the conductors on the semiconductor surface. As well as creating trapping stuctures, these same structures can be used to create experimental scenarios, discussed later in Section 2.4. As a result atom chips represent a highly flexible, integrated, experimental tool. They have the additional benefit that a new experimental setup can be implemented by simply changing a small chip within the experimental chamber, rather than having to implement large-scale changes to external structures.

Laser light trapping works by using an oscillating electric field, created by a strong laser light field, to mix the ground and excited states of an atom. Using the dipole approximation, the interaction between the electric field vector $\boldsymbol{\varepsilon}$ and the atom, with electric dipole moment operator $\mathbf{d}$, is

$$H' = -\mathbf{d} \cdot \boldsymbol{\varepsilon}. \tag{2.4}$$

The energy of the resulting mixed state is therefore dependent on both the intensity of the laser and the detuning of the laser from the groundstate to excited state transition. In the case of red detuning,

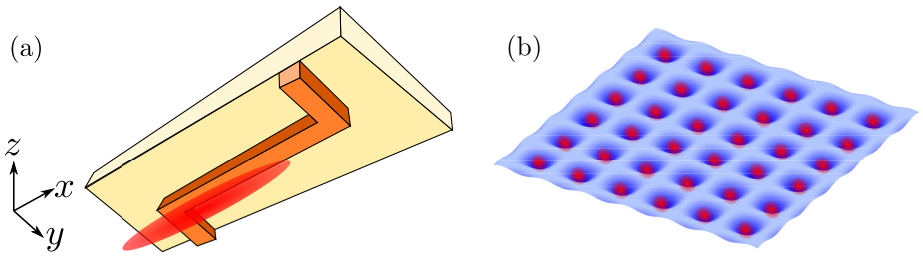

Figure 2.3: Examples of BEC traps. (a) An atom chip 'z-trap', named due to the shape of the conductor (orange structures on semiconductor surface) configuration. The condensate (red cloud) is trapped through the combination of the radial field from the central wire, plus a uniform field created by coils external to the vacuum chamber. The bends in the wire 'pinch' the field at either end to provide confinement in the x-direction. (b) BEC/BECs (depending on depth/separation) in an optically-created lattice. In this case, counter propagating blue laser beams have been used to create a 2d lattice structure. The condensates (red) are attracted to areas of low intensity. Varying the laser parameters allows control over the depth, size and separation of lattice sites.

the laser frequency is below that required for the transition and the mixed state has a lower energy in higher field regions. Atoms will therefore be drawn to high intensity regions of the field. For blue detuning the converse is true.

Other than optical access and limitations on the vacuum chamber, almost arbitrarily complicated potentials can be constructed through use of these laser light fields. They have been particularly useful in creating BEC lattice structures, as depicted in Figure 2.3. Such structures comprise sheets of laser light, which create a standing waves pattern within which the condensate sits. Varying the laser parameters allows one to create and modify the lattice parameters. This has opened the door to using BEC systems as extremely pure analogue models of solid state lattice structures. Through use of this technique,

a range of solid state behaviours have been demonstrated including Bloch oscillations [32] and the Mott-insulator transition [33].

Localised laser light also provides a powerful tool for manipulating discrete areas of existing potentials including, as just mentioned, filling the hole in quadrupole traps.

2.3 Modifying the atom-atom scattering length

The concept of a scattering length, as a measure of the interactions within a condensate system, was discussed in Section 1.2.3. Unless the situation is that of a multi-component BEC, condensate experiments trap a single state of the atomic system. This single state has a scattering length associated with it, for example 4.761×10^{-9} m for a Rubidium-87 singlet state [4].

As the scattering length relates to a particular transition within the trapped condensate atoms, it transpires that, if we are able to modify this transition, we can modify the scattering length, thus changing the physics and behaviour of the system. This can be visualised in the following way. Suppose, as shown in Figure 2.4, that there is another state whose energy is close to that of the trapped state. If these two states are coupled in some way, the scattering length within the trapped state is altered. This effect is known as a *Feshbach Resonance*. In general, the change to the scattering length will be of the form [4],

$$\Delta a \sim \frac{C}{E - E_{res}}, \tag{2.5}$$

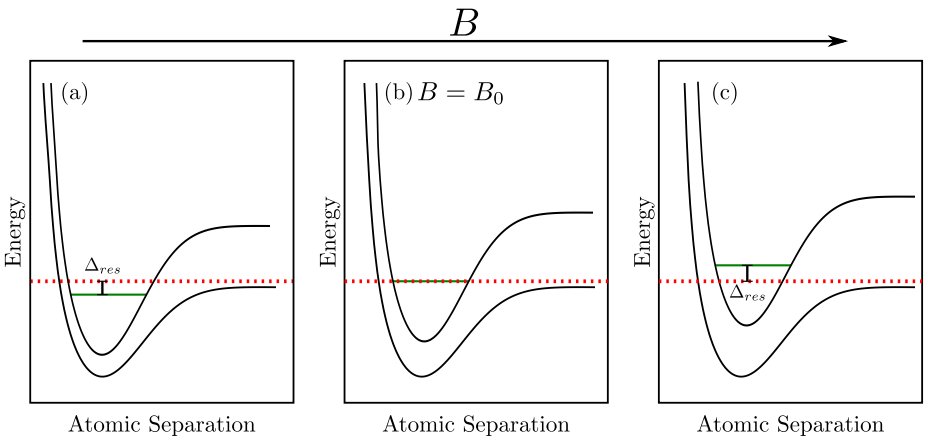

Figure 2.4: Schematic of the potential energy curves that give rise to Feshbach resonances. The black curves show the variation of the potential energy, versus the separation of the two atoms, for two different magnetic spin states. The red dashed line represents the energy level in the open channel, E, the green shows the near resonant energy level, E_{res}, in the closed channel (Δ_{res} is resonance width). As the external magnetic field, B, is increased on moving from (a) to (c), the relative positions of the energy curves and E_{res}, also change. (b) shows the curves and field value, $B = B_0$, for which $E_{res} = E$.

where E is the energy level of the trapped state and E_{res} the energy of the near resonant, closed state.

If the two states involved in the Feshbach resonance correspond to different magnetic states, it is possible to alter their relative energies in a continuous fashion through use of an external magnetic field. In this case the new, modified, scattering length is given by [34],

$$a_{fb} = a\left(1 - \frac{\Delta_{res}}{B - B_0}\right). \tag{2.6}$$

Here, B, is the external magnetic field, Δ_{res} the width of the resonance and B_0 represents the field value at which the the closed energy level is exactly on resonance with the open energy level. Additionally,

one sees that by varying the closed energy level from above, to below, the open energy level it is possible to switch from a positive to a negative scattering length.

Fortuitously, Feshbach resonances have been identified for a number of the alkali atom systems with which cold atom experiments are performed. In the experiment of Cornish et al. [35], the scattering length of Rubidium-85 was swept from strongly attractive to strongly repulsive values. This technique allows experimentalists to tune the interaction strength to any desired value, including turning it off, and thus is a powerful tool within the experimentalist's arsenal.

A final, but noteworthy point is that in order for Feshbach resonances to modify the scattering length, there must be some coupling between the involved energy levels. This is often done through use of a radio frequency field, known as $rf - dressing$. It is even possible to couple multiple Feshbach resonances in a single system, offering even more complex modification to the scattering length [36].

2.4 Manipulation

Creation and confinement of a BEC is, in itself, a notable achievement. After accomplishing the formation of a confined condensate, the logical extension is to look at ways in which the condensate may be manipulated. This is done both to probe the condensate and also to engineer a situation in which the condensate can itself be used as an experimental tool.

As with trapping, manipulation can be achieved magnetically, optically or by placing in proximity to shaped structures. Additionally,

rf-dressing techniques may be used. We will describe each of these techniques individually, although in experiments they are, obviously, combined.

Small scale magnetic manipulation is normally achieved through the use of atom chips. The ability to precisely control, or turn on and off, the currents through the various conducting channels on an atom chip allows one to create local changes in the magnetic field. The extent and type of control is limited only by the ingenuity of the atom chip design, though manufacturing limitations and the current capacity of the structure do play a role. Field profiles, which vary on the micrometre and millisecond range are currently common.

A change in trap profile can be achieved through turning on additional current-carrying structures, or by adjusting the current structures forming the initial trap. Increasing, or turning on, current in wires parallel to an elongated BEC in a z-trap will increase the perpendicular confinement.

Introducing a field from a structure not related to the confinement of the condensate allows one to add features to the potential landscape of the trap. One simple technique is to place a wire parallel to one BEC axis, and perpendicular to another. The field from this wire will create a local perturbation to the trap in the perpendicular direction. As the current is increased in this wire, the modification to the trap profile will disturb the BEC. Once the perturbation magnitude passes a certain value ($\sim \mu$), it is possible to split the condensate into two parts. Introduction and removal of a potential, to split and then recombine the condensate, provides a possible interferometric technique.

Another magnetic manipulation technique, still in its infancy, is the use of fields from ferromagnetic objects. These have the advantage that they can be shaped almost arbitrarily. Unlike the electric structures, there is no need for contact leads nor any issues regarding heat dissipation. Their disadvantage is the narrower range of fields available and their static nature. Through use of devices similar to hard drives, or, innovatively, hard drives themselves [37], one can conceivably make rewritable magnetic structures for use in experimental procedures.

Larger scale magnetic manipulation is normally achieved through use of a more slowly-varying magnetic field. This sort of field is typically generated by coils external to the experimental chamber. As discussed above, these externally-generated fields are often needed in trap creation, to compensate for or negate gravity, or to *plug* a hole in the bottom of a trap. They are also of use in experimental manipulation, for example an overall tilt in the external magnetic field can be used to move the condensate. This can be extended to induce rotation, or raise and lower the trapped condensate.

Optical manipulation involves the use of laser light fields acting on a condensate. Lasers offer extreme precision, in terms of position and also potential shape and size. This makes them ideal for use in manipulating an already trapped condensate.

Through scanning a laser, acting repulsively, across a trapped condensate, it is possible to *write* patterns into the density profile of the condensate. This can either be done continuously, by fast scanning of the laser across the surface, or, uniquely, with the modified density then being allowed to evolve.

Perhaps one of the most powerful tools optical manipulation offers is the ability to imprint an arbitrary phase on the condensate. To do this a laser radiation field is applied to the condensate for a short duration, τ. In this case the only change to the condensate will be an additional phase term given by [4],

$$\delta\phi(\mathbf{r}) = -\frac{1}{\hbar}\int_0^\tau dt V(\mathbf{r},t), \tag{2.7}$$

for a pulse starting at $t = 0$. It is therefore clear that through the correct choice of $V(\mathbf{r},t)$, the potential produced by the radiation field, we can create any phase profile we desire, subject to limitations on the optics.

The velocity of the condensate can be determined from consideration of the hydrodynamic equation and is linked to the gradient of the phase [4],

$$\mathbf{v} = \frac{\hbar}{m}\nabla\phi. \tag{2.8}$$

Therefore, through the correct choice of laser radiation field, we can *imprint* a velocity of our choosing, either locally, or globally, on the condensate without having to modify our trap in any way. Solitons, discussed in more depth later, are analytically derivable excitations of the condensate wavefunction. In the case of 'black' solitons their position is marked by a density node across which there is a π phase shift. It is therefore possible to create solitons [4] through imprinting this π phase shift onto a condensate in the position one wishes to create the soliton.

If the condensate trap has been formed through optical methods, large scale changes can be produced by moving the trap, similar to

the manipulation allowed by using an external magnetic field. In the case of optical lattices, the frequency and height of the lattice can be altered allowing different regimes to be reached.

Condensate manipulation can also be achieved by placing physical objects within the condensate's environment. The potential in the vicinity of an object is best represented by the Casimir-Polder potential. For a planar object this is,

$$V(r) = \frac{-C_4}{r^4}, \tag{2.9}$$

where r is the distance to the object. This potential is attractive at long distances and, on inclusion of the Leonard-Jones term, repulsive at short. With thought one can make use of this fact to construct, geometrically, shapes which create a desired potential. This approach is, however, complex and in its infancy, the main complication being that it is difficult to analytically, or numerically, determine the form of the surface potential for complex shapes.

The final manipulation method we describe involves the use of Feshbach resonances, as discussed in Section 2.3. When considering factors that influence the behaviour of the condensate, we look to the Gross-Pitaevskii equation, Eq. (1.53), reproduced here,

$$-\frac{\hbar^2}{2m}\Psi(\mathbf{r}) + V(\mathbf{r})\Psi(\mathbf{r}) + U_0\left|\Psi(\mathbf{r})\right|^2\Psi(\mathbf{r}) = E\Psi(\mathbf{r}). \tag{2.10}$$

With the ability to locally modify interactions, i.e. let $U_0 \to U_0(\mathbf{r})$, via local tuning of Feshbach resonances, one can create behaviour equivalent to that which would be produced through an external

potential,

$$V(\mathbf{r}) \simeq U_0(\mathbf{r}) \left|\Psi(\mathbf{r})\right|^2 . \tag{2.11}$$

This technique is sometimes called *rf-manipulation*, as the local implementation of the Feshbach resonance can be enacted through use of a spatially dependent radio frequency field. This additional control mechanism also offers the possibility to modify an existing external potential.

2.5 Imaging

Having discussed the various ways in which experiments are conducted, it is important to also consider the ways in which the results of these experiments are extracted. In contrast to the highly sophisticated techniques that have had to be developed to trap and manipulate condensates, imaging techniques are still relatively simple. The two main methods utilise either light scattering from atoms, or refraction of light, as it passes through the cloud.

The refractive method utilises the fact that the optical path length depends on the density of the medium that the light passes through. Light is split into a reference beam and a probe beam. The probe beam passes through the condensate before being recombined with the reference beam. Intensity variations in the recombined light give information on the changed optical path length and condensate density. This method does not require the light to be near resonance with internal transitions of the condensate atoms and represents an imaging technique which is particularly non invasive.

In the case of imaging as a result of scattering, fluorescence

imaging captures photons scattered from the cloud and absorption imaging examines the shadow produced by the cloud. In both cases, the light is at or near resonance. Capturing fluoresced photons is harder than detecting the absence of photons in the cloud's shadow. As a result, absorption imaging is orders of magnitude more sensitive than fluorescence imaging [38].

The optical density of the cloud is an issue for both of these techniques. For a typical condensate, this can be greater than unity across the majority of the cloud. This results in an almost purely black or white image, from which very little density profile information may be extracted.

One option to improve this situation is to detune the light from the scattering level. The other is to turn off the trap and wait before undertaking *time-of-flight* (TOF) imaging. A repulsive condensate will expand, reducing its optical density. The profile of the unexpanded cloud can then be inferred. The fact that the cloud has expanded also makes it easier to resolve with the photon capture device, often some form of CCD. There is, however, the disadvantage that you destroy the condensate. In order to image an experiment at various times through its evolution, it must be repeatedly run to collect the images. In fact, even imaging the unexpanded condensate may alter the internal states of the atoms sufficiently to alter the condensates behaviour.

As well as these standard techniques, other techniques are under continual development. Particular goals are single-atom resolution and non-destructive imaging. Two examples, among many, are the experiments of Westbrook and Ott. In the experiments of

Westbrook [39, 40, 41] a condensate of metastable Helium atoms is prepared. To image the condensate, it is allowed to fall upon a micro-channel plate, which allows three-dimensional time of flight distributions with single-atom resolution. In the experiments of Ott [42, 43, 44] a focused electron beam is used to image the cloud, with principles similar to those in electron beam microscopy. This provides in-situ measurements at a single-atom detection level.

Chapter 3

Numerical techniques

In this chapter, we discuss the important features of the numerical techniques used for BEC simulation in this thesis.

3.1 BEC simulation

In modelling a condensate experiment, we first start with an appropriate choice of system. We can vary the atom number, $N = \int |\Psi(\mathbf{r})|^2 \, d\mathbf{r}$, or peak density, the interaction length and mass (both related to atom species) and the external potential, $V(\mathbf{r}, t)$. It is the external potential, $V(\mathbf{r}, t)$, which offers the greatest and most flexible control of the experiment, providing a way to both trap and manipulate the condensate.

As theorists, we have the luxury of free control of any of these parameters, including the ability to create almost arbitrarily complicated potentials. This gives the opportunity to explore real experimental situations and those that would be very difficult to achieve experimentally.

Having chosen a system that we want to explore, the simulation of the experiment is performed by evolving in time the time-dependent GPE, Eq. (1.55), reproduced here,

$$-\frac{\hbar^2}{2m}\nabla^2\Psi(\mathbf{r},t)+V(\mathbf{r},t)\Psi(\mathbf{r},t)+U_0\left|\Psi(\mathbf{r},t)\right|^2\Psi(\mathbf{r},t)=i\hbar\frac{\partial\Psi(\mathbf{r},t)}{\partial t}. \tag{3.1}$$

This can be done through a variety of numerical techniques, which are well documented in the review of Proukakis [45].

Each approach has its own advantages and disadvantages. To cover the phase space under investigation often requires large numbers of simulations. It is therefore important to pick a method that is both fast and stable. As we were trying to understand pure, non-linear, quantum systems, we decided to use a method that represents a zero-temperature system, rather than some of the other methods available, which attempt to incorporate some measure of temperature or thermal excitations.

On consideration of these criteria, we decided to use a *fourth-order Runge-Kutta method*, optimised for systems with interactions, which was implemented via a Fourier method, RK4IP-P, detailed in Appendix A. As an aid to computational efficiency, we applied a projection operator to the standard GPE, giving the *projected Gross-Pitaevskii equation* (PGPE). This projection was carefully chosen to reduce memory requirements, whilst, as will be explained, retaining the behaviour, as described by the well established GPE. This PGPE approach can, in many ways, be seen as a subset of the Truncated Wigner (TW) method, which will also be briefly described. By introducing quantum noise in a specific manner, the TW method

allows incoherent excitations to occur. Details of this method are given in the thesis of Norrie [46].

3.2 Projected Gross-Pitaevskii equation

In performing the numerical evolution of the PGPE, we must choose a basis to describe the condensate. While we may choose any set of orthonormal basis states, two bases are particularly appropriate for the majority of condensate systems: the harmonic oscillator basis and the plane wave basis.

The harmonic oscillator basis is obviously well suited to situations where the condensate is held by a trap, as most trapping potentials are harmonic. But for this work, we chose a plane wave basis. The plane wave basis offers good performance in a range of situations and is particularly effective for untrapped condensates and for situations with periodic boundary conditions, as found in the majority of the simulations within this thesis.

The condensate wavefunction, Ψ, may be fully described in the plane wave basis as,

$$\Psi(\mathbf{r}) = \sum_{j=0}^{\infty} \alpha_j e^{i\mathbf{k}_j \cdot \mathbf{r}}, \tag{3.2}$$

where j specifies the mode with a wavevector, $\mathbf{k}_j$, and amplitude, α_j. Clearly it is not numerically possible to include an infinite number of modes. We deal with this through splitting our mode space into low energy, L, and high energy, H, subspaces and then only considering the low energy subspace. The cut off energy boundary ϵ_{cut}, which

separates these subspaces corresponds to a cut off wavenumber,

$$k_{cut} = \frac{1}{\hbar}\sqrt{2m\epsilon_{cut}}. \tag{3.3}$$

Neglecting modes with energy below ϵ_{cut} our condensate wavefunction becomes

$$\Psi(\mathbf{r}) = \sum_{j=0}^{j=j_L} \alpha_j e^{i\mathbf{k}_j\cdot\mathbf{r}}, \tag{3.4}$$

where j_L is the mode corresponding to the cut off, $k_{j_L} = k_{cut}$.

We assume that all particles under consideration reside within the low energy subspace, and that the high energy subspace is only accessed by intermediate virtual states during scattering events. This division is not simply practically motivated. In our derivation and discussion of the GPE, we repeatedly used assumptions which relied on finite populations of low energy modes. Therefore inclusion of high energy, scarcely populated, modes within the numerical system would be contrary to the validity of the GPE as an appropriate medel for the system. The splitting of subspaces and removal of unpopulated high energy modes, is analytically defined as a projection, thus our GPE, becomes a projected Gross-Pitaevskii equation (PGPE).

3.3 Discretisation and Fourier aliasing

To numerically implement our, now projected, GPE, with use of the RK4IP method we must also consider the effect of the discretisation of space. Such discretisation is necessary because our system will be stored on a discrete grid, with a finite number of elements. The Fourier method works by evolving the mode amplitudes using a

spatially discretised form of the equation governing their evolution. This equation is a Fourier series in undiscretised space, but becomes a discrete Fourier transform (DFT) when the spatial grid is imposed. Fortuitously, there is a host of extremely efficient and fast DFT calculation algorithms available. In general these are known as fast Fourier transforms (FFTs). The specific algorithm used in this work is called FFTW3 [47].

To use these FFT algorithms, particularly in two and three dimensions, it is necessary to meet a number of conditions. The most crucial of these is that both the momentum modes, k_j, and coordinate space points, x_n, must be identically, arranged on a uniform grid, each with equal numbers of equally-spaced grid points.

In the case of a three dimensional rectangular coordinate grid, of spatial extent $V = L_x \times L_y \times L_z$, the corresponding Fourier space will be spherical with a radius given by the cut-off wavevector, k_{cut}. It is therefore necessary to pad our momentum space with additional modes to create a rectangular system. These modes will lie outside the low-energy subspace and must be treated carefully to avoid Fourier aliasing and correctly implement the projection.

The first step is to define our coordinate and padded momentum space grids,

$$\mathbf{x}_n = \frac{L_x n_x}{N_x}\hat{\mathbf{x}} + \frac{L_y n_y}{N_y}\hat{\mathbf{y}} + \frac{L_z n_z}{N_z}\hat{\mathbf{z}} \tag{3.5}$$

$$\mathbf{k}_j = \frac{2\pi j_x}{L_x}\hat{\mathbf{k}}_x + \frac{2\pi j_y}{L_y}\hat{\mathbf{k}}_y + \frac{2\pi j_z}{L_z}\hat{\mathbf{k}}_z, \tag{3.6}$$

where N_x, N_y and N_z give the number of grid points in each direction,

so that the a total number of points is

$$N = N_x \times N_y \times N_z. \tag{3.7}$$

The sets $[n_x,\ n_y,\ n_z]$ and $[j_x,\ j_y,\ j_z]$ are integers, spanning identical ranges. These sets are chosen to have an even number of points, ideally with a point at the origin

$$n_{x,y,z}\ ,\ j_{x,y,z} \in [-N_{x,y,z}/2, N_{x,y,z}/2 - 1]. \tag{3.8}$$

If the grid does not include a point at the origin, a phase gradient, which depends on the grid size, is introduced. This spurious effect may obscure the genuine condensate behaviour. It is worth noting that this definition does not include a point at the positive boundary. Due to the periodic nature of the Fourier method it is incorrect (though a common mistake) to include points on both the positive, $L/2$, and negative, $-L/2$, boundaries: though in the case of large grids the error introduced will be small.

The extent of each space is given by

$$\begin{aligned} L_{x,y,z} &= N_{x,y,z}\frac{L_{x,y,z}}{N_{x,y,z}} && (3.9)\\ &= N_{x,y,z}\Delta_{x,y,z} \\ K_{x,y,z} &= N_{x,y,z}\Delta k_{x,y,z} && (3.10)\\ &= 2\pi\frac{N_{x,y,z}}{L_{x,y,z}}. \end{aligned}$$

As mentioned, though we only only wish to include low energy modes, with $k < k_{cut}$, it is necessary to pad the momentum space

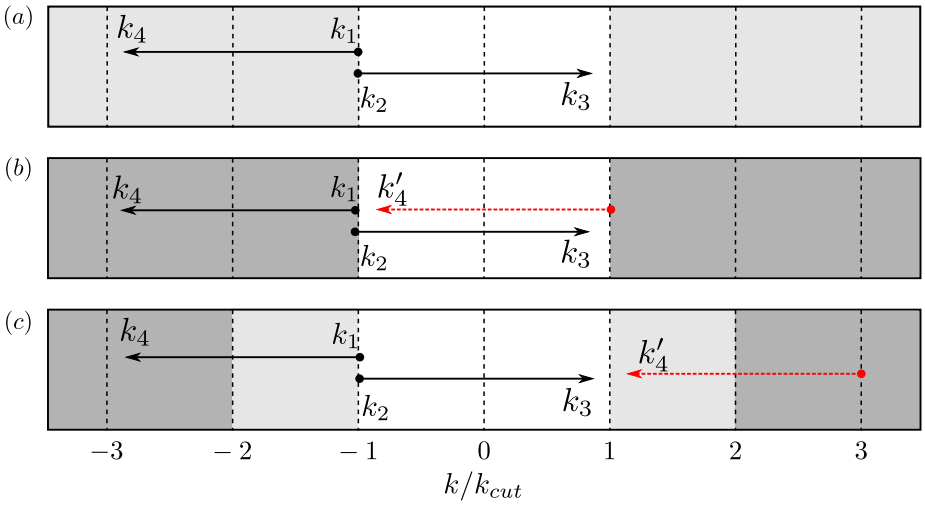

Figure 3.1: Schematic illustration of a scattering event involving two particles, $\mathbf{k}_1$ and $\mathbf{k}_2$ (black dots) at the edge of the considered momentum space with $k_1 = k_2 = -k_{cut}$. Light grey regions represent included momentum space outside the low energy subspace (white). Dark grey regions represent truncation of momentum space, i.e. are not included in the calculations. In (a) the full momentum space is included and the scattering takes place without aliasing. In (b) only the low energy subspace, of width $2k_{cut}$, is included. In this case, one of the final scattering wavevectors, k_4 is incorrectly aliased to k_4' (dashed red arrow) within the low energy subspace. (c) shows the result of padding the momentum space to a full width of $4k_{cut}$. There is again aliasing, but now the aliased wavevector, k_4', lies outside the low energy subspace and will therefore be removed by the projection, preventing incorrect modelling of condensate dynamics.

to correctly model the system. As a first step, one might think that simply padding the spherical low energy subspace into a rectangular form, as shown in Figure 3.1 (b), would be enough. However on consideration of Fourier aliasing, it becomes clear that further padding is required.

Within a Fourier method, both coordinate and momentum spaces are treated as periodic. Consequently, if some process causes a position or momentum component to become external to the grid, it

is mapped back into the grid, gaining an incorrect, lower, momentum value, separated from the true value by an integer multiple of the size of the momentum space, i.e. such that $k_{aliased} = k_{real} \pm nK_{x,y,z}$. This aliasing will obviously distort the modelled behaviour of the BEC.

The extent of momentum space padding required to remove this aliasing can determined by considering the most extreme event that could be expected to occur, as illustrated in Figure 3.1. In our system this would be a scattering event involving two particles with initial wavevectors, $\mathbf{k}_1$ and $\mathbf{k}_2$, both at the edge of the considered momentum space, e.g. with $\mathbf{k}_1 = \mathbf{k}_2 = -k_{cut}$ for a 1d scenario. If, as a result of the scattering event, one of the final wavevectors is $\mathbf{k}_3 = k_{cut} - \Delta k$ then, to satisfy momentum conservation, the other must be $\mathbf{k}_4 = -3k_{cut} + \Delta k$.

This result indicates that to completely remove Fourier aliasing, the mode space should be padded to extend between $\pm 3k_{cut}$ in each dimension. Figure 3.1 (a) shows the correct modelling of a scattering event within a system of this size. Figure 3.1 (b), shows an aliasing effect, which would incorrectly place a high energy quanta, corresponding to one of the final wavevectors, within the low energy subspace. As we are only concerned with aliasing events that would incorrectly place quanta within our low energy system subspace, it is sufficient to pad the mode space to extend between $\pm 2k_{cut}$, in each dimension, as demonstrated by Figure 3.1 (c). With this level of padding, the mode located at $\mathbf{k}_4 = -3k_{cut} + \Delta k$ in our extreme event example, would be mapped/aliased to $\mathbf{k}_{4'} = k_{cut} + \Delta k$, outside the low energy subspace. It will therefore be removed by the projection

and not influence condensate behaviour as governed by the GPE.

3.4 Groundstate generation

Analytical groundstates of the GPE only exist for a select few potentials. It is therefore useful to have a numerical technique to find the initial groundstate for an arbitrary potential landscape. As mentioned above, any wavefunction may be represented as an expansion over a set of orthonormal modes,

$$\Psi(0) = \sum_j \phi_j. \tag{3.11}$$

Each mode evolves, gaining a phase, which depends on the mode energy,

$$\Psi(t) = \sum_j \phi_j e^{iE_j t/\hbar}, \tag{3.12}$$

where E_j is the energy of the j^{th} mode.

If we choose to run our simulation in imaginary time, $t \to it$, Eq. (3.12) becomes,

$$\Psi(t) = \sum_j \phi_j e^{-E_j t/\hbar}, \tag{3.13}$$

which has the form of a dissipative equation. As the groundstate's mode energy is lowest, its decay is the slowest. Therefore the groundstate of the system may be found by starting with a *guessed* initial wavefunction, which is then evolved in imaginary time, with renormalisation at each time step, until the wavefunction ceases to evolve. Care must be taken in the choice of the initial, guessed, wavefunction,

$\Psi(0)$, and the size of the timestep to ensure that the groundstate found is a global, rather than local, minimum. This can be verified by extracting and tracking the chemical potential of the system, as described below.

3.4.1 Extracting the chemical potential

It is relatively simple to extract the chemical potential of the system as it evolves in imaginary time, through use of the following technique. From Eq. (3.13), we know that

$$\Psi(t + i\Delta t) = e^{-\mu \Delta t}\Psi(t), \tag{3.14}$$

where Δt is the time step. It therefore follows that,

$$\underbrace{\int |\Psi(t + i\Delta t)|^2 \, d\mathbf{r}}_{I} = e^{\frac{-2\mu\Delta t}{\hbar}} \underbrace{\int |\Psi|^2 d\mathbf{r}}_{N} \tag{3.15}$$

$$\Rightarrow \mu = -\frac{\hbar}{2\Delta t} \ln\left(\frac{I}{N}\right).$$

As N is a known, fixed, quantity, the number of atoms and, hence, I, is already calculated at each timestep for the purposes of renormalisation. It is thus simple to track the evolving chemical potential as the system evolves to its groundstate. This allows an insight into the progress of the groundstate generation and also provides a tool to check the veracity of the groundstate. For a given system, if we have found the true groundstate, varying the parameters, for example the timestep or spatial resolution, will not give a lower energy value.

3.5 Notes on numerical efficiency and stability

There are a number of points regarding the system parameters and implementation, which, if followed, give increased efficiency and computational speed. Due to the nature of the Fourier methods used, we gain the best performance for an even number of modes. Ideally this number will be 2^n. However, as this will not always be possible, a number with a large number of prime factors makes a satisfactory alternative.

The full, padded, momentum grid is only required when transforming to/from coordinate space at the beginning/end of each time step. For the other steps within the numerical method, it is sufficient to use the smaller grid corresponding to the low energy subspace, as the padded modes play no role in the system evolution. By only using the full, padded, momentum space where necessary, memory and processing demands are significantly reduced. Further details are given in Appenix A.

The stability of the numerical simulations is verified through calibration, i.e. by varying the timesteps, spatial resolution and mode numbers, until we are sure that the method is capturing the full dynamics of the system. The projection operator, which introduces an atom loss mechanism, means that the atom number may not be fully conserved. However, if the atom number changes by more than a small amount, this indicates that the simulation is not accurate. Common causes of this are insufficient modes, or too large a time step.

3.6 Extension to the Truncated-Wigner method

A brief discussion of the Truncated-Wigner (TW) method, which can be viewed as an extension to the PGPE, follows.

The TW method allows for the inclusion of spontaneous and spontaneously initiated processes, which are inaccessible to the GPE. Consequently, the TW approach enables the modelling of certain, experimentally observed, phenomena such as collisional haloes [48]. A full discussion of the derivation and statistics behind the TW method is given in [46]. If viewed as an extension to the PGPE, the TW formalism can be relatively simply summarised and numerically implemented. The technique works by taking an initial state of the PGPE,

$$\Psi(0) = \sum_j \alpha_j(0)\phi_j \tag{3.16}$$

and then modifying the mode amplitudes, in order that they follow a probability distribution, determined by the Wigner function. The modified initial mode amplitudes are given by,

$$\alpha'_j(0) = \alpha_j(0) + \frac{1}{2}(A_j + iB_j), \tag{3.17}$$

where A_j and B_j are real, randomly generated, numbers following a Gaussian distribution with unit standard deviation and a zero mean.

The result of this 'seeding', is that all the modes within the system now have a finite population. The finite population gives access to all included modes during the subsequent time evolution of the initial state. The freedom to explore these modes is the mechanism that

allows spontaneous processes to occur.

Due to the random nature of the initial state, its subsequent evolution is a numerical equivalent to a single experimental run (which also contains random fluctuations). As in an experiment, each run will only give information on the evolution of that particular starting state. To gain insight into the overall behaviour of the condensate, many simulations with different, random, initial states must be evolved, and then combined, to build a picture of the average behaviour.

The addition of the quantum noise to the system also acts to change the number of atoms within the system to

$$N' = N_0 + \frac{M}{2}, \tag{3.18}$$

where M is the number of system subspace modes and N_0 is the initial condensate atom number. As M is normally an appreciable fraction of N_0, care must be taken when comparing systems, as the TW method represents an appreciably different system to that described using the PGPE. Additional care must be exercised when modelling a system over a long time period. When using the TW method, the added quantum noise *thermalises* through collisional processes, changing its characteristics and invalidating the theoretical principles on which the theory is founded.

Chapter 4

Supersonic flow across a potential defect

Having covered the background and simulation techniques that underpin this work, we now focus on applying them to the study of cold-atom transport in *inhomogeneous potential landscapes*. In this section, we look in particular at the effect of small scale inhomogeneities on supersonic flow and find interesting links to other quantum mechanical (QM) systems.

4.1 Potential landscapes

As the BEC field continues to grow and mature, attention is turning towards areas that were initially overlooked or deemed unimportant to the challenges of the day.

Prior to the experimental realisation of atomic condensates, theoretical studies aimed to predict the basic properties of Bose-Einstein condensation. Experimentally, the first challenges tackled were to

realise the condensate and then to refine the techniques of creating condensates.

As the challenge of experimental condensate creation diminished, the next wave of experimental and theoretical research focused on proving and investigating central quantum mechanical principles. Areas such as quantum reflection [49], simple quantum interferometric systems [50] and soliton/vortex experiments [51, 52] dominated. Additionally, more control over the trapping geometry allowed exploration of restricted dimensionality regimes.

Throughout the focus has been on homogeneous systems. That is systems which are analytically smooth, trapped or controlled by well behaved potentials, containing analytically definable excitations, such as solitons and vortices, or investigating non-equilibrium behaviour on large scales, for example phase transitions. However, as experimental limits are continually pushed it becomes clear that there is a wealth of interesting physics relating to the imperfections, or deviations of real-world systems from the homogeneous case and that we are now in a position in which we can begin to investigate behaviour in inhomogeneous systems, both theoretically and experimentally.

Disorder in condensed matter systems is a large field in its own right [53, 54], with many interesting questions to be answered. Due to the high levels of control offered by condensate experiments, they offer an ideal medium with which to probe the effects of disorder. There are already cases in which a non-homogeneous potential has been used to investigate behaviour that only occurs in the presence of disorder. Anderson localisation, an effect which limits the diffusion of waves, requires a disordered medium. In the case of BECs, it may

be observed through use of a noisy *speckle* optical potential [55], a quasi-periodic lattice [56] or other potentials with some controllable disorder parameter. At sufficient disorder levels, Anderson localisation is able to stop the free expansion of the BEC and instead, form a stationary localised wavefunction. This effect also impacts on transport, tunnelling and other properties of the BEC.

Another key question, concerns whether supersonic flow of BECs, or similar coherent quantum systems, can ever be observed without loss of the coherence properties of the system. One might expect, using the Landau picture of superfluidity, that any non-homogeneous system will simply break down as a result of excitations caused by supersonic flow past inhomogeneities.

Additionally, regardless of the refinement in field generation, there will always be a resolution limit at which a homogeneous field will, in fact, be fluctuating. Causes of these fluctuations range from thermal and electronic noise, to micro-fabrication limitations in the creation of small scale structures. Knowledge of the effect of these fluctuations is therefore key.

Fields generated by atom chips represent an area in which limitations caused by non-ideal potentials are particularly prevalent. The close proximity of the condensate to the potential-producing structures leaves little opportunity for spatial variations in the potential to be screened. It has been shown that the limiting factor in the accuracy of a variety of atom chip experiments is potential *roughness*, caused by imperfections in the current-carrying structures [57].

One could approach this issue by looking to create smoother potentials. This is a laudable enterprise and enhancements in trapping

and manipulation techniques will always be welcome. It is, however, interesting to take the opposite approach, as in this work, and to try to more fully understand the role of small scale potential fluctuations in a BEC experiment.

We decided to look at the concept of a potential defect by considering a rectangular well or barrier. We start by defining this problem in a linear quantum mechanical system, which may be done analytically (see Section 4.2). We then extend the analysis, through use of numerical simulations, to the non-linear case (Section 4.3). The results of these simulations show a clear link to the linear problem. This link and extensions to the system are explored in the remainder of the chapter.

4.2 Quantum mechanical case

Our approach starts with the very simple case of a single perturbation to an otherwise homogeneous system. We begin by considering the linear analogue of the non-linear system, which we eventually aim to investigate.

If the interaction term, U_0, in the GPE is set or reduced to zero, we regain the Schrödinger equation, describing a linear quantum mechanical system. In the case of a linear quantum mechanical system, it is possible, for some simple shapes of perturbing potentials, to analytically derive transmission and reflection probabilities. This allows an ideal starting point from which to further investigate supersonic flow of condensates past perturbing potentials. The analytical approach presented here uses the transfer matrix method,

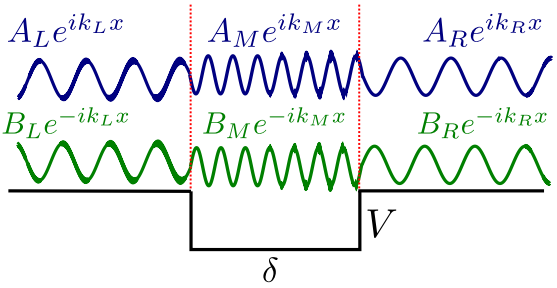

Figure 4.1: Schematic representation of a linear quantum mechanical system comprising a potential well of depth V and width δ. Rightwards/leftwards travelling waves are represented in blue/green respectively.

comprehensively outlined by Gilmore [58]. Here, we explore the case of a rectangular well/barrier of height/depth V and width δ.

We split the system into three regions, shown in Figure 4.1. The ingoing and outgoing regions, where the potential = 0, and a region (middle, M) containing the potential under analysis. For the ingoing (left, L) and outgoing (right, R) regions the wavefunctions can be written,

$$\phi_L(x) = A_L \exp^{ik_L x} + B_L \exp^{-ik_L x}, \tag{4.1}$$

$$\phi_R(x) = A_R \exp^{ik_R x} + B_R \exp^{-ik_R x}, \tag{4.2}$$

where k is the wavevector,

$$k = \sqrt{\frac{2mE}{\hbar^2}}, \tag{4.3}$$

of the quantum mechanical wave in that region. The wavefunction and its derivative must be single valued at all points in space.

These matching criteria may be used to relate the various ampli-

tudes, using a transfer matrix, T, approach,

$$\begin{bmatrix} A_L \\ B_L \end{bmatrix} = T \begin{bmatrix} A_R \\ B_R \end{bmatrix} = \begin{bmatrix} t_{11}(E) & t_{12}(E) \\ t_{21}(E) & t_{22}(E) \end{bmatrix} \begin{bmatrix} A_R \\ B_R \end{bmatrix}. \tag{4.4}$$

Where T is formed by multiplying a series of matrices related to the system [58],

$$T = E^{-1}K^{-1}MKE. \tag{4.5}$$

The E^{-1} and K^{-1} matrices relate to the left hand region, E and K to the right hand region and the M matrix to the middle region containing the potential, see Figure 4.1.

It is possible to derive and use these matrices for a variety of situations. To relate most closely to the subsequent numerical results, we use a barrier of height V and width δ, for a system with energy $E > V$. In this case the relevant matrices are,

$$K^{-1} = \frac{1}{2}\begin{bmatrix} 1 & \frac{1}{ik_L} \\ 1 & \frac{1}{-ik_L} \end{bmatrix}, \tag{4.6a}$$

$$E^{-1} = \begin{bmatrix} \exp^{-ik_L x} & 0 \\ 0 & \exp^{ik_L x} \end{bmatrix}, \tag{4.6b}$$

$$M = \begin{bmatrix} \cos(k'\delta) & -k'^{-1}\sin(k\delta) \\ k\sin(k'\delta) & \cos(k'\delta) \end{bmatrix}, \tag{4.6c}$$

$$K = \begin{bmatrix} 1 & 1 \\ ik_R & -ik_R \end{bmatrix}, \tag{4.6d}$$

$$E = \begin{bmatrix} \exp^{ik_R x} & 0 \\ 0 & \exp^{-ik_R x} \end{bmatrix}, \tag{4.6e}$$

where k' is the wavevector in the region containing the potential

$$k' = \sqrt{\frac{2m(E-V)}{\hbar^2}}. \tag{4.7}$$

Using these matrices in Eq. (4.5) and assuming $k_L = k_R = k$ gives

$$T = \begin{pmatrix} \cos(k'\delta) - \left(\frac{ik}{2k'} + \frac{ik'}{2k}\right)\sin(k'\delta) & \frac{\exp^{-2ikx}(0.5ik^2 - 0.5ik'^2)\sin(k'\delta)}{kk'} \\ \frac{\exp^{2ikx}(-0.5ik^2 + 0.5ik'^2)\sin(k'\delta)}{kk'} & \cos(k'\delta) + \left(\frac{ik}{2k'} + \frac{ik'}{2k}\right)\sin(k'\delta) \end{pmatrix}. \tag{4.8}$$

Using this transfer matrix, we can now find an expression for the transmission coefficient of a wave incident on the barrier region.

Conservation of momentum dictates that,

$$\hbar k_L \left(|A_L|^2 - |B_L|^2\right) = \hbar k_R \left(|A_R|^2 - |B_R|^2\right). \tag{4.9}$$

For a particle or wavefunction incident from the left, there will be transmission and reflection, but no probability of incidence on the barrier from the right. Therefore $B_R = 0$ and the conservation equation can be rewritten,

$$\left|\frac{B_L}{A_L}\right|^2 + \frac{k_R}{k_L}\left|\frac{A_R}{A_L}\right|^2 = 1. \tag{4.10}$$

In this form, inspection of the various terms allows definition of a reflection coefficient

$$\mathfrak{R} = \left|\frac{B_L}{A_L}\right|^2 \tag{4.11}$$

and transmission coefficient

$$\mathfrak{T} = \frac{k_R}{k_L} \left| \frac{A_R}{A_L} \right|^2 , \tag{4.12}$$

which, together, satisfy the conservation equation

$$\mathfrak{T} + \mathfrak{R} = 1. \tag{4.13}$$

Use of the transfer matrix, Eq. (4.4), to find A_L, with $B_R = 0$, allows the transmission coefficient, $\mathfrak{T}$, to be expressed in terms of a single element of the transfer matrix

$$\mathfrak{T} = \frac{k_R}{k_L} \left| \frac{1}{t_{11}(E)} \right|^2 , \tag{4.14}$$

which can be simplified further if the wavevectors to the left and right are equal i.e.,

$$\text{if } k_L = k_R \ , \quad \mathfrak{T} = \left| \frac{1}{t_{11}(E)} \right|^2 . \tag{4.15}$$

An example of the transmission coefficient versus E curve for a square barrier, demonstrating the occurrence of resonances in the transmission probability, is shown in Figure 4.2, $\mathfrak{T} = 1$ whenever an integer number of half de Broglie wavelengths spans the barrier.

4.3 Numerical set up

Having outlined an analytical, linear, QM system, we now explain how to extend the analysis into the non-linear regime, through use of numerical simulations. All results in this section have been calculated

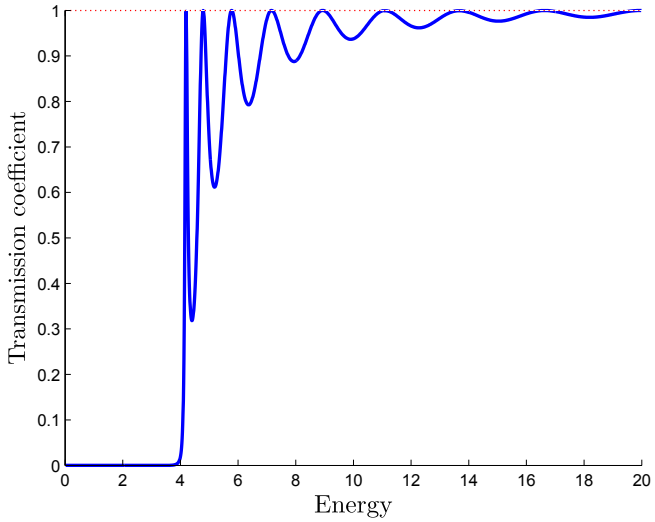

Figure 4.2: Transmission probability calculated for a barrier of height, $V = 4$ and width $\delta = 5$, with $m = \hbar = 1$.

through numerically advancing the condensate wavefunction, Ψ, using a one dimensional projected Gross-Pitaevskii equation (PGPE) method, as outlined in Section 3.1.

The numerical set up for the simulations, illustrated in Figure 4.3, takes a box of length L, filled with condensate atoms. The atom density is initially uniform. We chose $n_{bulk} = 1 \times 10^7$ atoms m^{-1}, which is well within the limit required for a BEC system to be treated as 1d or quasi-1d, Eq. (1.84). The confining trap frequency is set to $f_\perp = \omega/2\pi = 10 =$ kHz to ensure suppression of axial modes so that we can use the 1d interaction term, Eq. (1.83), reproduced here

$$g_{1d} = \frac{2\hbar^2}{m}\frac{a_s}{a_\perp^2}. \tag{4.16}$$

The atom species under consideration is Rubidium-87, with a mass of 87.0 a.m.u. and a 3d scattering length $a_s = 5.4 \times 10^{-9}$ m.

Due to the use of Fourier transforms in our numerical method,

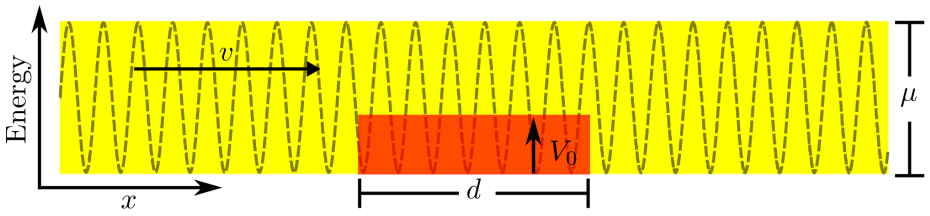

Figure 4.3: Numerical set-up. Yellow region represents the condensate, with chemical potential, μ. Dotted line represents the phase imprint for a given speed, v. A barrier (orange) of width d and height V_0 is slowly introduced after the phase imprint, see text for further details.

the boundary conditions are implicitly periodic. A *flow* can therefore be created by imprinting a phase along the initial, uniform, wavefunction,

$$\psi_{t=0}(x) = \sqrt{n_{bulk}} \cdot e^{ikx}, \tag{4.17}$$

where k is the wavevector corresponding to the required velocity, v, of the condensate

$$k = \frac{vm}{\hbar} \quad . \tag{4.18}$$

In order to satisfy the periodic boundary conditions, there is the requirement that the phase may only change by $\Delta\phi = 2\pi n$ over the length, L, of the system, where n is an integer. This restriction gives us possible velocity values,

$$v = \frac{\hbar}{m}\frac{2\pi n}{L}. \tag{4.19}$$

The uniform density condensate, with a phase corresponding to a uniform flow with velocity, v, represents the starting point for our simulation. Having created this initial state we start the numerical time evolution.

To conduct our numerical experiment, a perturbation to the external potential is introduced in the centre of the system, see Figure 4.3. If this potential were to be introduced instantaneously, it would excite the condensate, which could mask, or destroy, the effects under investigation. To minimise this shock, the perturbation is introduced using a $\tanh(t^2/\alpha_t)$ prefactor to the perturbation amplitude. The constant, α_t, is chosen to raise the potential to within 1% of its full value over a given time period. Test simulations, using a subsonic BEC, showed that introduction over $\sim 10^5$ time steps with $dt = 1.0 \times 10^{-7}$s produced no excitations. The value of α_t corresponding to this $\sim 10^5$ time step ramp is $\alpha_t = 3.6 \times 10^9$, which was then used for subsequent simulations, unless stated otherwise.

Limitations to the perturbing potentials that may be modelled arise from the resolution and size of the system. The spatial resolution, which, via the Fourier transform, links to the energy resolution, is chosen to allow full modelling of features of order $\Delta x \approx 0.1\xi$ spatially and $\Delta E \approx 0.1\mu$ energetically. We also ensure that the simulation does not run for longer than $t_{max} = L/(2v)$, to prevent any disturbances that we create from reaching the periodic system boundaries. Allowing flow across these boundaries would be appropriate if considering a toroidal ring system. As we are trying to isolate the case of simple flow across the barrier, appropriate to both a ring and a 1d 'cigar' shaped system, we limit the run time to $t < t_{max}$.

In an attempt to only capture behaviour after the perturbing potential is applied, the wavefunction is only output at set times after the completion of the tanh ramp, where the completion time is, as mentioned, $t = 0.01\text{s} = b_{raise}$. At these set times, the density of

the condensate, $|\Psi|^2$, is output for all x, creating a snapshot/frame of the condensate at that moment in its time evolution. Pavloff, defined a drag value [59] to investigate the behaviour of the condensate. In this work we define a similar drag value, related to the disturbance of the condensate from its bulk value,

$$\mathfrak{D} = \sum_{x_1}^{x_n} (|\Psi_x|^2 - |\Psi_{bulk}|^2). \tag{4.20}$$

The measure that we have chosen, $\mathfrak{D}$, to represent the disturbances within the system, involves more than just the transmission coefficient, $\mathfrak{T}$, of the system. However, with some more analytical work, we can derive an expression for $\mathfrak{D}$. Firstly, from Eq. (4.4), setting B_R to zero we get the relationships

$$A_L = t_{11} A_R, \tag{4.21}$$

$$B_L = t_{21} A_R, \tag{4.22}$$

$$A_R = \frac{A_L}{t_{11}} = \frac{B_L}{t_{21}}, \tag{4.23}$$

which will be of use to us shortly. Using the definition Eq. (4.1), for ϕ, gives us,

left side of potential	right side of potential
$A_L^2 + B_L^2$	A_R^2
$= A_L^2 + \left(\frac{t_{21}}{t_{11}}\right)^2 A_L^2$	$= \frac{A_L^2}{t_{11}^2},$

(4.24)

as the form of $|\phi|^2$ on either side of the potential. A value for n_{bulk}

is given by $|\phi|^2$ of the initial input wavefunction $A_L \exp^{ikx}$,

$$n_{bulk} = |A_L \exp^{ikx}|^2 = A_L^2. \tag{4.25}$$

Subtracting Eq. (4.25) from Eq. (4.24) gives values corresponding to the production of excitations at either side of the potential

left side of potential	right side of potential
$\mathfrak{D}_{left} = \left(\frac{t_{21}}{t_{11}}\right)^2 A_L^2$	$\mathfrak{D}_{right} = \left(\frac{1}{{t_{11}}^2} - 1\right) A_L^2,$

(4.26)

where the time dependence of these two terms will be given by a time dependent prefactor, $C(t)$, specific to the given situation.

Using the relation $\mathfrak{T} = (1/t_{11})^2$, from inspection of Eq. (4.8), gives,

$${t_{11}}^2 = \cos^2(k'\delta) + \frac{1}{4}\left(\frac{k}{k'} + \frac{k'}{k}\right)\sin^2(k'\delta), \tag{4.27}$$

$${t_{21}}^2 = \frac{1}{4}\frac{(k'^2 - k^2)^2}{(kk')^2}\sin^2(k'\delta), \tag{4.28}$$

which can be used in Eq. (4.26), to give values for the disturbance.

As excitations to the system are primarily observed upstream (to the left) of the condensate [60], we restrict our excitation measure to the left side ($x = 0$ running to $x = L/2$) of the potential, referred to so far $\mathfrak{D}_{left}$, but now referred to as simply $\mathfrak{D}$. Similarly, when considering the disturbances at a specific time, t_{sp}, it is $\mathfrak{D}_{left}(t_{sp})$ that we refer to.

The influence of any modulations in the density, caused by raising the perturbing potential, was considered by looking at the difference in $\mathfrak{D}$ at two different times. Each frame includes any excitation, or density modulation, caused by raising the potential. Taking the difference between time steps should therefore remove any effect that this modulation may have on the results. This procedure gives a numerical excitation measure of

$$\mathfrak{D}_{diff} = C(t_2\mathfrak{D} - C(t_1)\mathfrak{D} = (C(t_2) - C(t_1)) \left(\frac{t_{21}}{t_{11}}\right)^2 A_L^2 \qquad (4.29)$$

where, $C(t)$, is a time dependent constant related to the production of excitations, which is proportional to the transmission $C \propto \mathfrak{T}$. In fact, it transpired that for our work *any* of the excitation measures, whether for the full box, left hand side at a specific time, or difference between frames, showed the same behaviour.

4.3.1 System parameters

In conducting the numerical situations, certain assumptions and definitions of variables were chosen as follows.

In all cases we start with a uniform bulk density of $n_{1d} = 1 \times 10^7 \mathrm{m}^{-1}$. When modifying the scattering length, we refer to modified scattering length in terms of $g_{fac} \times g$, where g_{fac} is a the factor by which the Rubidium scattering length, $g = 5.4 \times 10^{-9}$ m, is scaled. Speeds, unless otherwise specified, are given in ms^{-1}.

In referring to lengths, we use as our length scale the healing length, ξ, for the unmodified scattering length system, $g_{fac} = 1.0$. Likewise, as an energy scale we take the chemical potential, μ of

the unmodified scattering length system. In considering the Landau critical velocity, v_c^L of a system, we refer to the critical velocity in the undisturbed, bulk part of the system.

4.4 Initial results

We started by introducing relatively small, $\sim 1 - 10\xi$ wide (system size is 100s of ξ wide), rectangular (both positive and negative) perturbations to the potential landscape of the flowing one dimensional condensate. In the case of an interacting non-linear quantum system, the traditional Landau picture, as described in Section 1.3, predicts that the excitation versus velocity curve for this system will be as depicted in Figure 4.4.

On examining Figure 4.4, the curve schematically divides into three sections. The first, lowest velocity, section I corresponds to the region in which the system is universally subsonic. As a result it behaves as a superfluid, smoothly responding to the perturbing potential with no excitations created.

The second, intermediary speed region II, of most interest to this work, is the area in which a large number of excitations are expected. It starts somewhat before the bulk critical velocity is reached, as the perturbed density near the applied potential causes the velocity to locally exceed the Landau velocity, thereby triggering the production of excitations. These excitations swiftly peak at a velocity corresponding to the Landau velocity, v_c^L, of the bulk system. After the peak, there is a gradual decline in the magnitude of excitations, as the kinetic energy of the system grows in comparison

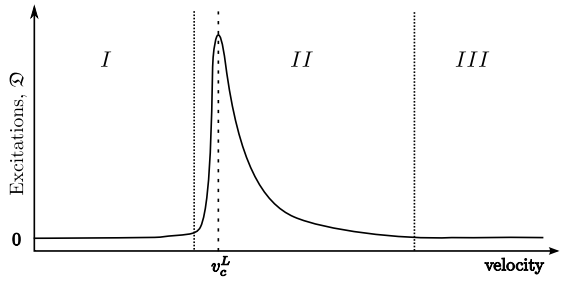

Figure 4.4: Expected variation of the excitation parameter, $\mathfrak{D}$ with velocity in the Landau picture. Dotted lines divide the three regions, I (subsonic region excitation free), II (subsonic-supersonic transition region where significant excitation occurs beyond the critical velocity, v_c^L (dashed line)), III (far supersonic, kinetic energy dominates, little excitation).

to the potential energy. The potential energy is fixed and, in this case, mainly related to the size of the perturbing potential.

The third region III, again an area of low excitations, corresponds to the high velocity region in which the kinetic energy is so large in comparison to the potential energy scale of the perturbation that the condensate no longer *sees* the perturbation. In this regime, the condensate is sometimes referred to as a *quasi-ideal gas* [61].

Our results, for example those shown in Figure 4.5, did not show this predicted excitation versus velocity curve. Instead of the excitations smoothly falling away in the intermediate velocity region II we find, within this region, multiple points at which the excitations vanish. This behaviour occurred for both the barrier and well perturbations.

Immediately this was reminiscent of the multiple transmission resonances present within the linear quantum mechanical case. Running the same simulations with $g_{fac} = 0$ showed (Figure 4.5) as expected, an exact match with the analytically-calculated resonance positions.

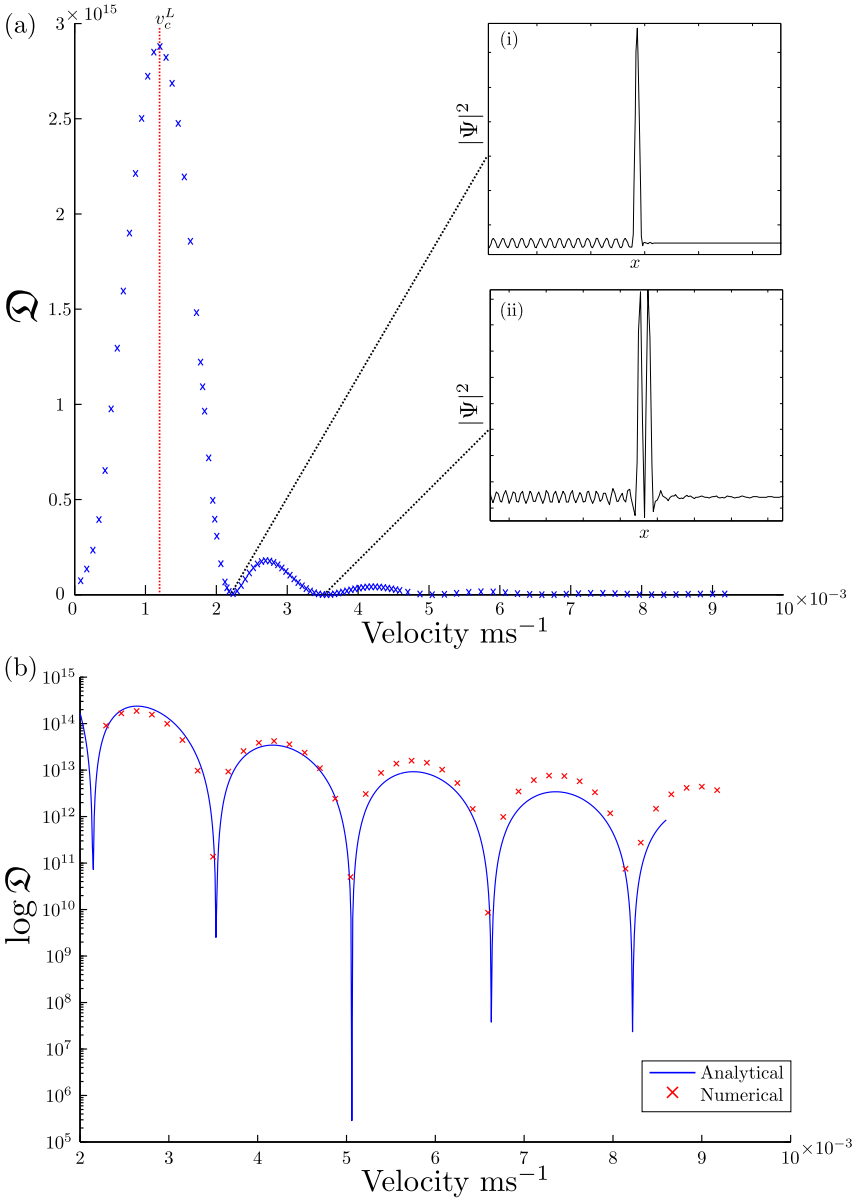

Figure 4.5: (a) Velocity versus excitation, $\mathfrak{D}$ curves, in this case for a barrier of width, 6ξ, height 0.2μ , with $g_{fac} = 0.5$, for frames at times $t_1 = 1.1b_{raise}$. $t_2 = 1.2b_{raise}$. Insets (i) and (ii) show the density of the condensate at the first and second-order Landau excitation free points (LFP) respectively. They reveal the formation of an n-peaked density modulation, where n is the order of the LFP. (b) Crosses show velocity versus $\log \mathfrak{D}$ results for the same perturbing potential and time snapshots, but with $g_{fac} = 0$, the analytically calculated curve (solid) is also included.

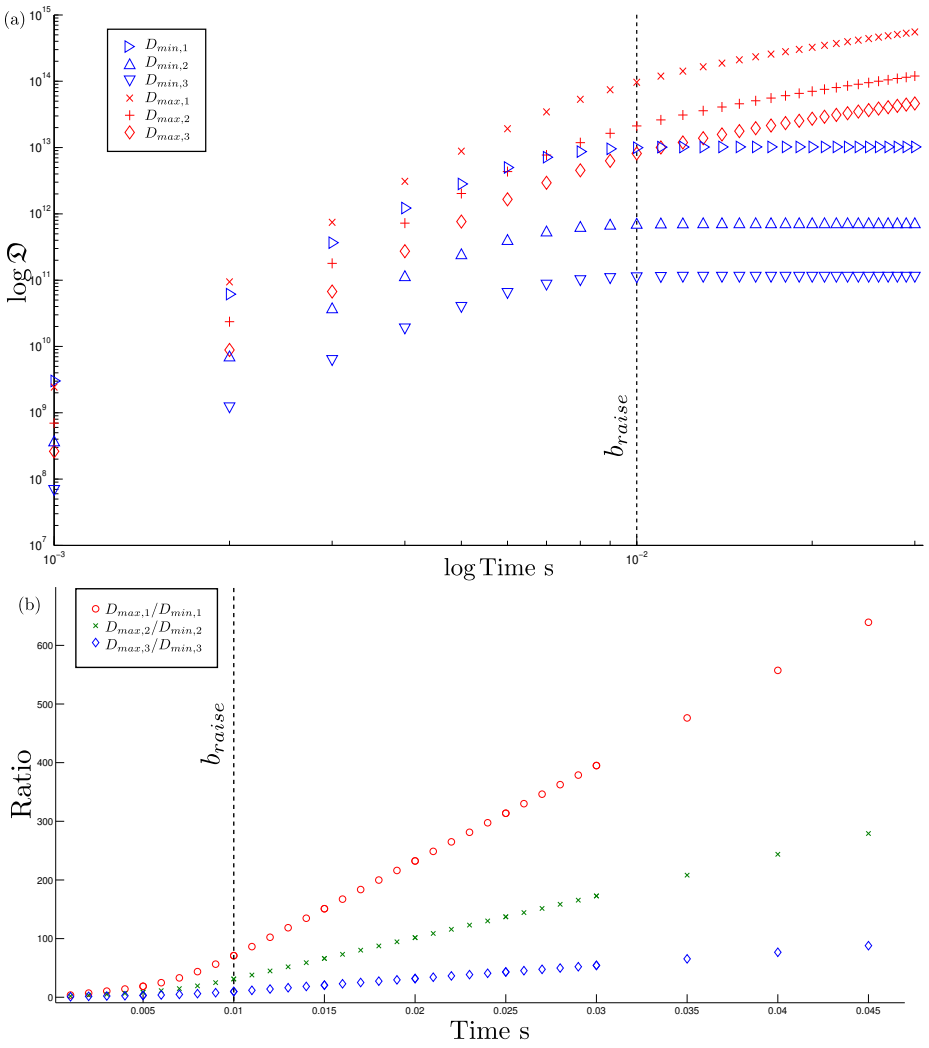

Figure 4.6: Figures illustrating the bound nature of the resonances. In (a) the values of $\mathfrak{D}_{min}$ and $\mathfrak{D}_{max}$, at the positions of the first three minima/maxima are plotted (see key for meaning of symbols). The introduction of the perturbing potential, $t = 0 \rightarrow t = b_{raise}$, causes a growth in all values. After the perturbation has attained its maximum value, $\mathfrak{D}_{max,n}$ continues to increase, indicating the production of excitations, $\mathfrak{D}_{min,n}$, at a constant value due to complete suppression of excitations. (b) shows the ratio $\mathfrak{D}_{max,n}/\mathfrak{D}_{min,n}$, and indicates that after introduction of the barrier the production of excitations is linear with time.

Away from the resonance positions, discrepancies in the match result from the background drop off of excitations, which means that the increasing kinetic energy (discussed above), is not fully taken into account.

On examining the condensate profile, $|\Psi(x)|^2$, within the perturbing potential, we observed fluctuations, with an additional peak appearing at each successive resonance (Figure 4.5, inset (i) and (ii)). This is reminiscent of another textbook system, the energy eigenfunctions of an infinite square well.

Figure 4.6 examines the suppression of excitations at these resonance points. It shows that at each resonance the Landau excitations are *completely* suppressed for all time, whereas off resonance, excitations grow at a constant rate. Figure 4.7 confirms that the values, in particular the $\mathfrak{D}_{min}$ values, are *not* influenced by the speed over which the potential is introduced. The increase in $\mathfrak{D}_{max}$ for longer potential ramp times, shown in Figure 4.7, occurs because the analysis of $\mathfrak{D}$ is being conducted over the time during which the potential is introduced. Although longer ramp times introduce fewer excitations, we are sampling excitation production over a longer period of time, hence the larger values of $\mathfrak{D}_{max}$ for longer potential introduction times.

It seems clear that these resonances in our non-linear system, which is free from Landau excitations, link to the analytical transmission resonances in the analogous linear quantum mechanical system. The next step is to gain a greater understanding of how the positions of these resonances change with the system parameters.

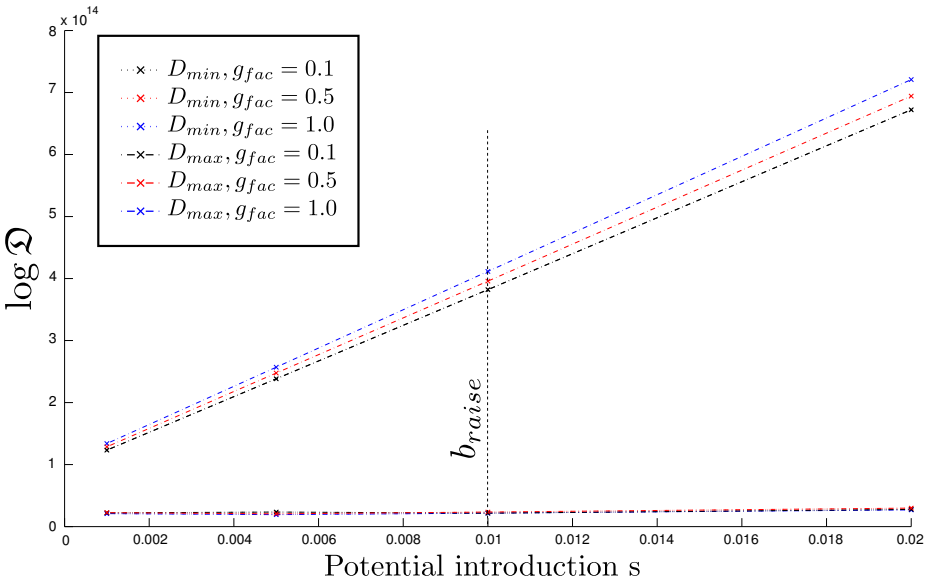

Figure 4.7: $\mathfrak{D}_{max}$ and $\mathfrak{D}_{min}$ values calculated for different times over which the potential is introduced. $\mathfrak{D}_{min}$ remain constant for different speeds of introduction. $\mathfrak{D}_{max}$ is larger for longer introduction times, as more time is available to produce excitations at these off resonance points.

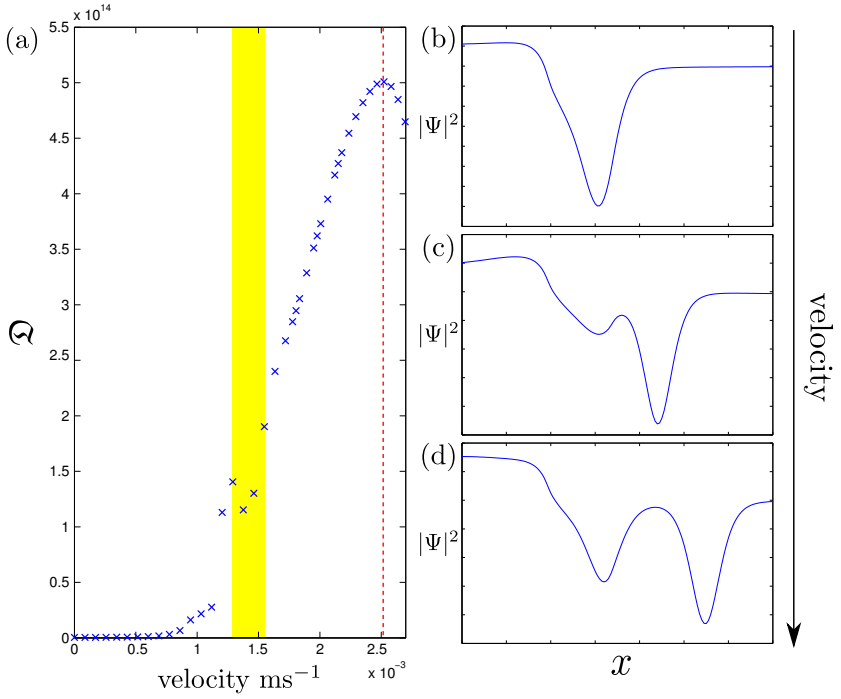

Figure 4.8: In (a) the yellow rectangle highlights the unexpected deviation from the traditional Landau picture (Figure 4.4), of the excitation, $\mathfrak{D}$, versus velocity curve that was observed for $V < v_c^L$ (red dotted line) for some parameters of the perturbing potential. Panels (b)-(d) show $|\Psi|^2$ versus x, at increasing velocity values chosen to span the deviation. They show the change from a single peak, to a double peak in the condensate density. The x-axis is restricted to the perturbing potential region.

4.4.1 Deviation before v_c^L

It was also observed that for some parameters studied for slow past the rectangular potential barrier, the Landau excitations do not follow the expected behaviour. This behaviour, shown in Figure 4.8 during the onset of excitations, occurs at a speed below the bulk Landau critical velocity, v_c^L.

On examination of the condensate density, $|\Psi|^2$, within the perturbing potential region, it seems that there is a small suppression in

excitations, linked to a transition between two distinct quasi-bound states localised within the potential region, see insets Figure 4.8.

In this subsonic case, for an attractive perturbing potential the density within the potential region, n_{state}, satisfies $n_{state} < n_{bulk}$. This behaviour contrasts with the atom density profiles observed at the $v > v_c^L$ resonant points, in which the density of the *quasi-bound* state exceed the bulk density. As a result, we do not believe that this behaviour is linked to the same linear transmission resonance mechanism as in the $v > v_c^L$ case, but relates instead to some other, possibly similar, mechanism.

4.5 Phase space campaign

We began a phase space campaign sweeping through values of the scattering length and the height and width of the perturbing potential. We also looked for any difference between a positive/repulsive barrier and a negative/attractive well.

Figure 4.9 shows that changing the scattering length causes the positions and form of the resonant points to smoothly alter. Increasing g_{fac} shifts the Landau excitation free points (LFPs) to higher velocities. The frequency of occurrence of LFPs increases with increasing g_{fac} and with increasing potential size. We found that the first observed resonance was not necessarily that of a first order LFP. The difference in behaviour observed for a barrier and a well was simply a positional shift, as shown in Figure 4.10.

There are cases, in which the resonant behaviour is not observed. Although we see persistence of the resonance behaviour for small at-

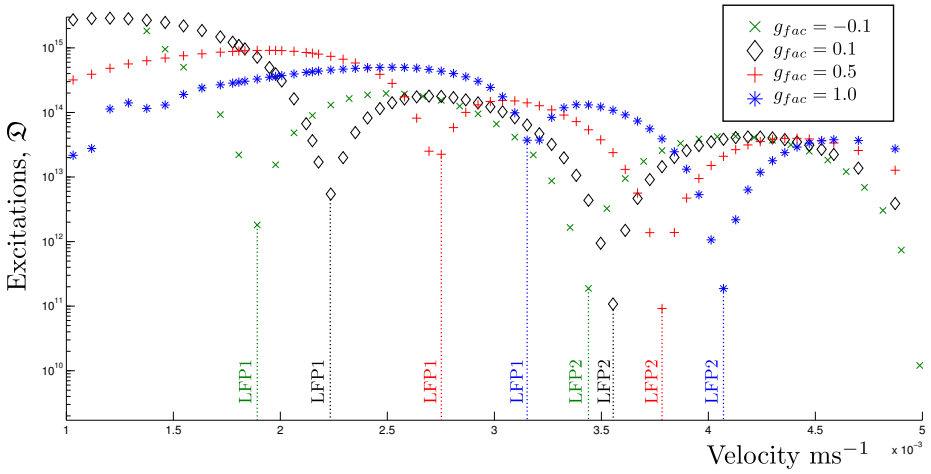

Figure 4.9: A collection of excitation versus velocity lines for different g_{fac} values shown in the key (in each case the perturbing potential had the same size, both spatial and in amplitude). As g_{fac} increases, the position of the LFPs (marked by vertical dotted lines) move to higher velocity values.

tractive interactions $g_{fac} \sim -0.1$, for strongly attracting systems the excitations *clump* together strongly (a 'Bose Nova' [62]) altering local Landau velocities and masking/destroying the resonant suppression of excitations.

For barrier widths less than the healing length of the system, the perturbing potential becomes delta like as seen by the condensate and the resonances are again not observed. If the perturbing potential is taller or deeper than the chemical potential of the system, it produces excitations of a magnitude that again mask or destroy the resonance profile that we are looking for.

Returning to the cases in which resonances were found, we now introduce a classification of the resonance points. The simplest way to do this is by specifying the number of peaks in the corresponding part of the density profile that lies within the potential area. A

resonance position with two peaks within the potential region thus becomes a second order Landau-excitation free point (LFP2).

Having labelled the resonance points, we can plot their relative positions for different phase space parameters. The relevant plot is the product of the barrier/well width, d and the atomic wavevector within the perturbation region at resonance, k_p, against $g_{fac}gn_{1d}/V$. The latter is, effectively, the ratio of the chemical potential of the system $\mu_{sys} = g_{fac}gn_{1d}$, to the potential energy scale, determined by the amplitude of the pertubation, V. When this is done for a range of phase space parameters, with a fixed product of height and width squared i.e., $Vd^2 = A$ where A is a constant, the points corresponding to the different orders of resonance, i.e. points $LFP1, 2, 3, \ldots$ collapse onto distinct separate lines, crossing $g_{fac} = 0$ at the positions of the linear QM resonances.

Figure 4.10 shows the results of a large number of simulations in which $Vd^2 = \hbar^2/m$. The positions of the different LFPs vary continuously with changing k_pd (which in our case relates to changing the condensate speed), passing through the analytical, linear, value at $g_{fac} = 0$. An attempt was made to analyse the problem using multiple-scale analysis, as detailed in [63], however this did not match our numerical results.

In particular, multiple-scale analysis predicts a negative slope to the relative positions of LFPs versus k_pd, for some orders of LFPs. This is not observed in any of our simulations, though our results of $g_{fac}gn_{1d}/V$ versus k_pd, do match an intuitive picture, that an increasing barrier size and or increasing repulsive interactions, will require a higher wavevector to meet the resonant criteria.

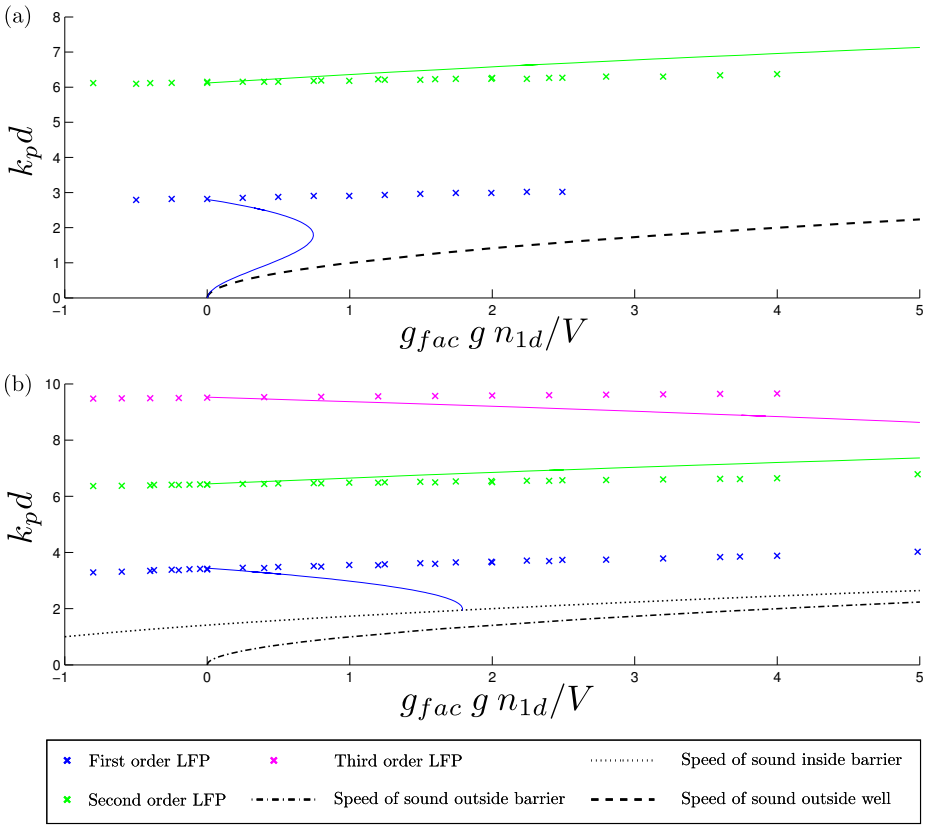

Figure 4.10: Results of simulations for potentials in which $V\delta^2 = \hbar^2/m$. (a) Shows $g_{fac}gn_{1d}/V$ versus $k_p\delta$, for a potential well and (b) shows the same plot, for a barrier. In both cases the points (see key for parameters) corresponding to different order LFPs can be seen to group on continuous lines. Solid lines are created using multiple-scale analysis.

4.6 Stability analysis

Some investigations were conducted into the stability of the resonant behaviour when the system is subject to a perturbation. Initially this was done by adding other speeds to the initial system. Specifically we modified the initial state to

$$\psi_{t=0}(x) = \sqrt{n_{bulk}}(Ae^{ik_A x} + Be^{ik_B x}), \tag{4.30}$$

where k_B is the second speed and A and B are the relative amplitudes of the two waves with different speeds. This method introduces density modulations to the system due to interference between the mismatched phase components, which causes a locally varying Landau velocity.

Despite these modulations, for a small second, or indeed any multiple combination of supplementary velocity components, in which the perturbation was small (i.e. $B \lesssim 0.05A$). We still observed resonances in the suppression of Landau-excitations, corresponding to the primary speed. However, $\mathfrak{D}_{min}$ changed value due to the secondary components producing excitations, when the primary component was on resonance.

After observing the resonances within the well and barrier cases, discussed above, we extended our investigations in order to gain a fuller understanding of the causes of the resonant suppression of Landau excitations. This was done by first considering the $\mathfrak{D}$ versus velocity curves for a variety of potential shapes.

4.7 Other potential shapes

As the resonances in the suppression of Landau excitations, observed for the rectangular potentials, are linked to predicted resonances in linear QM systems, the next potential form to be considered was a modified Pöschl-Teller (PT) potential. This is defined by the equation

$$V_{PT}(x) = -\frac{\hbar^2}{2m}\alpha^2 \frac{\lambda(\lambda-1)}{\cosh^2 \alpha x}, \tag{4.31}$$

where α and λ are constants. The form of the PT potential shown in Figure 4.11, was chosen as it is the simplest of a class of potentials to possess analytical solutions in the linear QM system. The transmission probability for Eq. (4.31) is given by [64, 65],

$$|T|^2 = \sin^2(\Phi_e - \Phi_0). \tag{4.32}$$

The argument of the sine term is

$$\Phi_e - \Phi_0 = \tan^{-1}\left(\frac{\sinh(\pi k/\alpha)}{\sin(\pi\lambda)}\right), \tag{4.33}$$

where $k^2 = 2mE/\hbar^2$. If the constant, λ, is an integer, the denominator vanishes and the PT potential is the supersymmetric partner of the zero-potential case [66] and thus the transmission coefficient Eq. (4.32), is 1 for all energies. This is not the case for the repulsive form of the potential.

To see if these linear results were replicated within our non-linear system, simulations were run with a range of α values, chosen to give potentials of similar size to those used in the rectangular investigations.

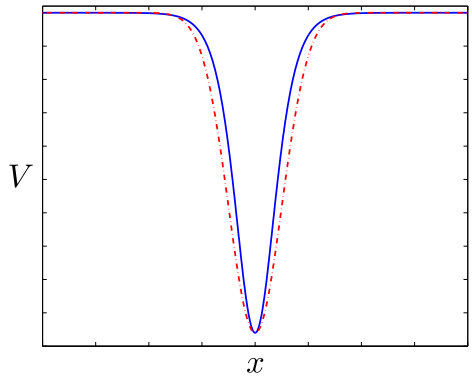

Figure 4.11: Example of an attractive Pöschl-Teller potential shown by the blue line. The dotted red line shows the Gaussian approximation, Eq. (4.35), to the PT potential

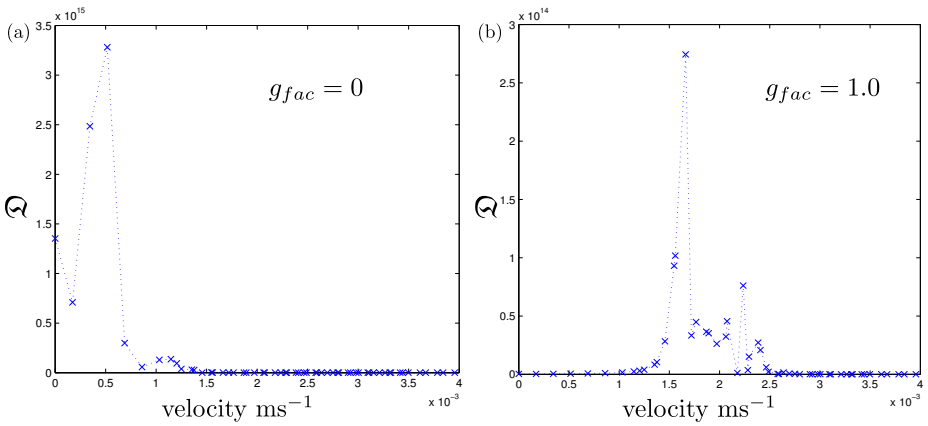

Figure 4.12: Excitation $\mathfrak{D}$ versus velocity plots for a Pöschl-Teller potential. Results are shown for $g_{fac} = 0$ and $g_{fac} = 1.0$. PT potential parameters, $\lambda = 2$, $\alpha = 2\ln(1+\sqrt{2})/6\xi$.

As predicted, there was no sign of any resonances for repulsive potentials. For the attractive potentials, the behaviour was not as predicted by the linear calculation, because the waves propagate without excitation at all speeds. Instead, the form of the $\mathfrak{D}$ versus velocity curves, shown in Figure 4.12, is better described as a cross between the traditional Landau picture, Fig. 4.4, and the results for the well and barrier cases, Fig. 4.5. Though there are velocity values at which the production of Landau excitations is reduced, the suppression is not *complete* as was the case for the rectangular potentials.

As a result, we are unable to assert that these suppression points are linked to the resonances observed either in the linear case, or for a rectangular well or barrier perturbation to a non-linear system. We looked at the possibility that the observation of resonances was affected by the form of the potential, changing the resonance condition. The α value was therefore modified to a time-dependent form,

$$\alpha(t) = \alpha \tanh(t^2/\alpha_t), \tag{4.34}$$

in order to make the potential of the resonant form throughout its introduction. This modification did not, however, cause any noticeable change to the general form of the $\mathfrak{D}$ as a function of velocity.

A modification to the numerical set-up was also implemented. In the work of Kiriushcheva and Kuzmin [67], the linear case was numerically investigated. Their approach was to take a Gaussian wavepacket, incident on a PT potential, and to review its form following transmission.

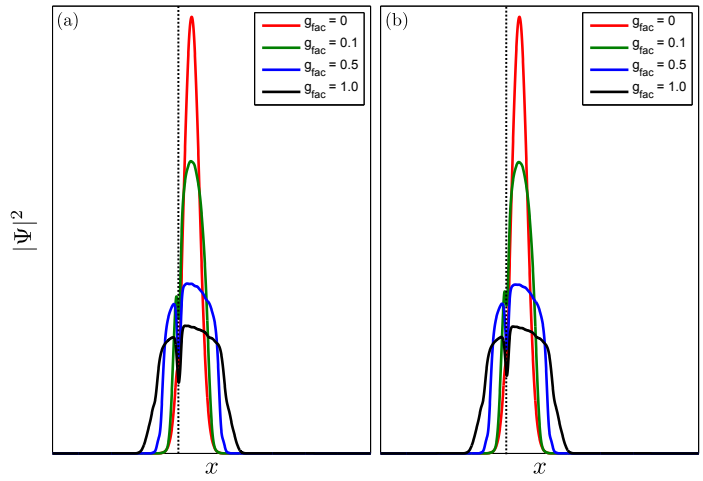

Figure 4.13: Snapshot of a Gaussian, condensate wavepacket, with different g_{fac} values, passing a PT potential located at the dotted line. (a) is for $\lambda = 4.0$ (b) shows the results for $\lambda = 3.5$. These λ values give similarly size PT potentials. As can be seen, the results do not qualitatively differ.

We recreated this approach, utilising our numerical method, which also allowed us to extend into the non-linear regime. Fig. 4.13 shows results for $\lambda = 4.0$. For the linear regime, we observed the behaviour reported in [67], i.e. full reflectionless transmission with preservation of the shape of the Gaussian wavepacket.

On increasing the non-linearity, $g_{fac} > 0$, the transmission remained almost reflectionless. This initially led us to believe that we may be seeing the resonant transmission behaviour in a non-linear system. However, on using a non-integer λ value, $\lambda = 3.5$, we observed results that were qualitatively the same (Fig. 4.13), which seems to preclude this conclusion. The literature lacks [67, 68, 69, 70, 71, 72, 73] results for non-integer values of λ, for comparison.

On visual examination of the shape of the PT potential, shown in Figure 4.11, it closely resembles a Gaussian form. We therefore

also looked at a Gaussian potential,

$$V_{Gauss}(x) = \lambda(\lambda - 1)\frac{\hbar^2}{2m}A^2 e^{-\frac{x^2}{2\sigma^2}}, \tag{4.35}$$

which closely resembles the PT potential for $\sigma = 1/\alpha$ and $A = \alpha$, as shown by the dotted line in Figure 4.11.

The results of simulations for this attractive Gaussian potential were similar to those of the PT potential. Signs of suppression of excitations were found at some velocity values, but with no clear indication of full suppression or bound resonances. This was also the case when an attractive triangular potential was considered.

4.8 Concluding remarks on suppression of Landau excitations

We observed complete suppression of Landau excitations, in supersonic non-linear systems, for rectangular perturbing potentials (both attractive and repulsive). These resonance points are continuously linked to the transmission resonances found in the analogous, linear quantum mechanical system.

Other potentials were examined, some showing signs of suppression of the excitations, but none displayed the bound, complete, resonant suppression of excitations, seen with rectangular potentials.

The suppression of excitations seems to be related to the existence, or possibility, of a *quasi-bound* state within the perturbing potential,

of the standing wave form seen in Figure 4.5 (inset (i) and (ii)), the condensate wavefunction at the resonances. This explains why suppression was only observed for attractive potentials (which allow bound states), but not for a delta-like or repulsive potentials, except for the special case of the repulsive rectangular potential, which allows bound states in the linear regime.

It seems it may be difficult to find, or predict, the form of a perturbing potential that will give complete, bound, resonant suppression of excitations in the non-linear regime. The results for the Gaussian wavepacket, incident on a PT potential, which is predicted to possess a bound state and transmission resonance in the linear case, show hints of resonant suppressiong at all velocities. But, until questions regarding the lack of qualitative difference between the tuned, $\lambda =$ integer value, and untuned, $\lambda =$ non-integer value, results are resolved, we are unable to draw any further conclusions.

If full, bound, resonant suppression of Landau excitations only occurs for potentials which support both a bound state and a transmission resonance, where the transmission $\to 1$, then this behaviour may indeed be rare. Other than rectangular potentials and *special*, reflectionless potentials, such as the PT potential, general, smooth potentials do not possess transmission $\to 1$ behaviour [58].

In conclusion it is remarkable that we have found instances in which expected Landau excitations are stongly suppressed. This violation of Landau criterion in a non-linear system (where we expect the Landau picture to apply) seems to be associated with the presence QM resonances in the corresponding linear system. The demonstration of this link between the linear and non-linear quantum

world, has potentially far-reaching consequences for all systems that may be described by a non-linear wave equation.

Chapter 5

Magnetic field imaging

In this chapter, the use of condensates as an experimental measuring tool is considered. Condensates can be used to make matter-wave analogues of many optical systems, with perhaps the greatest focus being on the creation of interferometric systems. In this work, we consider the use of a condensate as both the imaging medium and measurement tool.

5.1 Imaging

We have already discussed the effect of various magnetic, electric and even surface potentials on condensate systems. So far, this discussion has been led by considering how these potentials affect the condensate. Recently, the converse of this relationship has started to be examined, i.e. using a condensate's response to a potential to measure that potential.

In this work, we choose to concentrate on the imaging of magnetic fields, created by two-dimensional structures, as this allows us to use

a specific, and highly efficient, numerical technique, discussed later. The resolution offered through BEC imaging techniques allows their use as a microscopy device.

We focus on the special case of magnetic fields generated by two dimensional structures and find that, in this case, we are able to use the condensate's density profile to reconstruct both the current density and, in the case of a field generated by a two dimensional electron gas (2DEG), the density of ionised donors, which supply electrons to the 2DEG.

5.1.1 Magnetic field microscopy with a BEC

We illustrate the principles behind magnetic field microscopy/imaging with a simple example. The technique is based on placing a homogeneous BEC within an inhomogeneous field. This inhomogeneous field will produce density fluctuations within the BEC. Through measuring the density fluctuations optically and analysing their spatial form, the form of the field may be reconstructed.

In a typical setup, the BEC will be subject to both the trapping field, B_{trap} and the field under investigation, B_{inv}. The modulation of the magnetic field will change the density by an amount inversely proportional to the chemical potential, μ, of the condensate, $\Delta n/n \sim \mu_F B_{inv}/\mu$.

Any condensate geometry may be used. However, using a quasi-1d condensate simplifies the relation between the magnetic field and atomic density. For a 1d condensate, in the Thomas-Fermi regime and aligned along the x-axis, the density-magnetic field relation along

the x direction is given by

$$\mu_{1d} - m_F g_F \mu_B \left|\mathbf{B}(x)\right| = \hbar\omega_\perp \sqrt{1 + 4a_s n_{1d}(x)}. \tag{5.1}$$

Here, $\omega_\perp$, is the transverse, confining frequency. The 1d chemical potental, μ_{1d}, depends on the system considered, as discussed in Section 1.2.4.

Due to the simplicity of this relationship and the ease of creating needle/cigar shaped, quasi-1d condensates with atom chip setups (which are also ideal for bringing the condensate close to a field-creating structure), this type of setup has been used in experimental work [74].

We can gain a measure of the experimental sensitivity from Eq. (5.1). Within the mean field approximation, where $4a_s n_{1d}(x) \gg 1$, a small change in magnetic field, ΔB_x, will change the density by

$$\Delta n_{1d} = \frac{m_F g_F \mu_B \Delta B_x}{2\hbar\omega_\perp a_s}. \tag{5.2}$$

If the density is measured with resolution, Δx, then the corresponding difference in atom number measure will be

$$\Delta N = \frac{m m_F g_F \mu_B \Delta B_x \Delta x}{2\hbar\omega_\perp a_s}. \tag{5.3}$$

With knowledge of the smallest atom number, ΔN, resolvable by our Δx resolution imaging system, Eq. (5.3) may be rearranged to give,

$$\Delta B = \frac{2\hbar^2 a_s}{m_F g_F \mu_B} \frac{\Delta N}{l_0^2 \Delta x}, \tag{5.4}$$

which is the minimum resolvable variation in magnetic field. Here, m

is the atom's mass and $l_0 = \sqrt{\hbar/m\omega_\perp}$ is the axial harmonic oscillator length, a measure of the width of the cloud in the strongly confined dimensions.

Study of Eq. (5.4) shows that there are two limits to the sensitivity of our magnetic microscope. If $l_0 > \Delta x$, the sensitivity is governed by the spatial resolution of the imaging system in the weakly trapped directions and scales as $\sim 1/\Delta x$. This regime corresponds to trap frequencies of the order ~ 1 Hz, which are experimentally difficult to achieve.

We are therefore more likely to be in the regime where $l_0 < \Delta x$. In this case the condensate is 'narrower' than the spatial resolution of the optical imaging system. Then, the sensitivity depends on the full spatial resolution of the imaging system and scales as $\sim 1/\Delta x^3$. Optical imaging currently achieves resolutions of the order $0.5 - 10$ µm.

Wildermuth et al. achieved a spatial resolution of 3 µm with a field sensitivity of 4 nT [74]. This could, however, be improved by adjusting the atomic scattering length, a_s, via Feshbach resonance processes, as discussed in Section 2.3. In principle, a field sensitivity of ~ 10 pT is attainable in this way [74, 75].

Consideration of existing magnetic field microscopy techniques, covered below, reveals that BEC magnetic field microscopy offers a tool with which to cover an area of sensitivity-resolution phase space, not currently served by other methods.

BECs also offer several other advantages as microscopy tools. Given a well defined trapping field and atom number, then no further calibration is required to extract quantitative information about the

magnetic field being measured. The ability to easily manipulate the spatial position of the BEC allows the BEC to be scanned across the area of interest. This enables imaging to occur over areas, or indeed volumes, much greater than the extent of the cloud. In this way it would also be possible to use a 1d condensate to build up a 2 or even 3 dimensional picture of a magnetic field. Through use of a 2d condensate, it may be possible to image an area equal to the extent of the cloud (a 3d condensate adds complications due to the effective spatial integration of the density caused by 2d imaging processes). Through use of in situ BEC imaging techniques, one can envisage real time imaging of changing magnetic fields.

5.1.2 Existing magnetic field probes

There are a variety of experimental techniques for measuring magnetic fields. The ideal would be a method that offers good spatial resolution and field sensitivity. Unfortunately, as is often the case, the methods which offer higher spatial resolution offer poorer sensitivity and vice-versa. An overview of existing methods, summarised in Table 5.1, is presented below, in order of increasing field sensitivity and decreasing spatial resolution.

Magnetic force microscopes

Magnetic force microscopes use a technique derived from the principles of atomic force microscopy. In atomic force microscopy, a cantilever is micro-fabricated with dimensions small enough to ensure that, on approaching a surface, the atom-surface interaction is sufficient to deflect the cantilever. The topography of the surface

Method	Spatial Resolution	Magnetic Field Sensitivity
Magnetic Force Microscopes	50×10^{-9} m	0.5×10^{-3} T
Scanning Hall-Probe Microscopy	510×10^{-9} m	5×10^{-6} T
SQUIDs	10×10^{-6} m	2×10^{-12} T
Atomic Magnetometers	2×10^{-3} m	1×10^{-15} T

Table 5.1: Comparison of magnetic field microscopy techniques

can then be mapped either through noting the force required to stabilise the cantilever, or by operating the cantilever at its resonant frequency, in which case changes in the resonance amplitude give information on force gradients.

To extend this technique into the magnetic domain, i.e. to achieve magnetic force microscopy, a ferromagnetic tip is used. In some cases, the entire cantilever is etched from ferromagnetic materials. Alternatively, a layer of ferromagnetic material may be deposited on an atomic force microscope tip.

Magnetic force microscopy measurements are able to provide field sensitivity of 0.5 mT at spatial resolutions of ~ 50 nm. Both limits originate primarily from the exact structure of the tip. While the topography extracted through force microscopy measurements will be qualitatively correct, quantitatively correct measurements require calibration of the specific tip in use: a complex procedure.

Scanning Hall-probe microscopy

A magnetic field, perpendicular to a current-carrying wire, causes deflection of the electrons and a change in the voltage drop across the wire. This is known as the Hall effect and is utilised in the creation of Hall-probes to measure magnetic fields. Combining a Hall-probe with a scanning tunnelling microscope allows simultaneous measurement of surface topography and magnetic field strength, a technique known as *scanning Hall-probe microscopy*.

The sensitivity of the device is again linked to the fabrication process. For a spatial resolution of ~ 510 nm, fields may be measured with 5 μT sensitivity.

Superconducting quantum interference device

The starting point for a superconducting quantum interference device, or SQUID, is a strip of superconducting material. At some point this strip is split equally, and then recombined to form a loop. Each side of the superconducting loop is interrupted with a small insulating, or non-superconducting metal, section creating two Josephson junctions. The current through each junction,

$$I(t) = I_C \sin\left(\Delta\phi(t)\right), \tag{5.5}$$

depends on the phase difference, $\Delta\phi(t)$, across the junction, and a constant known as the critical current of the junction, I_C.

A magnetic field perpendicular to a superconducting ring structure creates circulating current around the ring. This circulating current creates a different phase at each of the two Josephson junc-

tions. This then allows measurement of the magnetic field through examining the current within the device. Use of SQUIDs allows field sensitivities of 2 pT at resolutions of 10 μm.

Atomic magnetometers

The final magnetic microscopy technique we will consider is atomic magnetometry. In this technique, a vapour cell of alkali atoms is combined with a light source. Certain energy levels within the atoms may be excited by the light source, causing subsequent photon emission, which may be detected. The energy levels of the atoms is influenced by magnetic fields. This dependency is used to infer the magnetic field strength through resonances in the photon emission spectrum. This technique yields the most precise field resolution, of up to 2 fT, but with a resolution of only 2 mm. Moreover, the magnetometer can only be operated in a very low field environment.

BEC magnetometers

On consideration of Table 5.1, it is apparent that BEC magnetometers fill a gap in the existing spectrum of methods, as well as offering various operational benefits, discussed in Section 5.1.1. As a result it is clear that effort will continue to be placed in developing practical BEC microscopy architectures.

5.2 Magnetic fields from 2d structures

With BEC microscopy offering an interesting and unique tool with which to image fields in new ways, we turn our attention to a specific

case in which knowledge of a magnetic field structure (i.e. its spatial variation), gives insight into the source of the magnetic field. In a general case, in which some electronic structure creates a magnetic field, the vectorial nature of the field and underlying current flow means that it is very difficult to gain, with any certainty, insight into the properties of the field-creating structure.

There exists, however, a special case. If the field is created by a structure that exists exclusively in a two dimensional (2d) plane, we are able to recover information about the structure by measuring the magnetic field profile. We consider magnetic fields created by two dimensional electron gases (2DEGs) as the ability to gain information into the current density and donor distribution of a 2DEG would be a boon to the field of experimental semiconductor physics and device design.

5.2.1 2DEGs, atom chips and BECs

2DEGs represent a huge field in quantum electronics, with a variety of construction techniques and forms. For the purpose of this thesis these details are unimportant, and the simple description of a 2DEG being a thin layer of electrons, possessing higher mobility and lower density than a metal, is sufficient.

Commonly formed at the junction between two types of semiconductor, it would be easy to imagine the use of 2DEGs within a BEC atom chip experimental set up. This could be either to use the BEC as a magnetic field probe, with which to image or monitor a 2DEG, or to use subsurface *wire* structures fabricated within a 2DEG to trap and manipulate a BEC. 2DEG based atom chips could benefit

from the low levels of electromagnetic noise compared to atom chips that use surface mounted wires.

The behaviour of the electrons within the 2DEG is determined by the electron donor distribution, which is influenced by a variety of factors. In turn, the electron dynamics create features within the current density profile. These features then define the magnetic field. As mentioned above, the magnetic field produced by two dimensional structures are most easily analysed using Fourier methods, detailed below.

The normal starting point for calculating the magnetic field, $\mathbf{B}$, created at position, $\mathbf{r}$, by electric current elements is the Biot-Savart law

$$\mathbf{B}(\mathbf{r}) = \frac{\mu_0}{4\pi} \oint \frac{\mathbf{j}(\mathbf{r}') \times (\mathbf{r} - \mathbf{r}')}{|\mathbf{r} - \mathbf{r}'|^3} \mathrm{d}^2\mathbf{r}', \tag{5.6}$$

where $\mathbf{r} = (x, y, z)$ is the position in question, $\mathbf{r}'$, is a position vector in the conductor where the current density is $\mathbf{j}(\mathbf{r}')$, and μ_0 is the permeability of the vacuum. The integral is performed over the entire current-containing region.

If the current is contained within a two dimensional plane, it is possible to use the convolution theorem to process this integral using Fourier methods, which are much faster than performing full numerical evolution [76]. Firstly we consider the x component of the field, at a distance, z, from a current-carrying slab of thickness d and parallel to the $x - y$ plane. The Biot-Savart law gives,

$$B_x(x, y, z) = \frac{\mu_0 d}{4\pi} \oint \frac{J_y(x', y')}{\left[(x - x)^2 + (y - y')^2 + z^2\right]^{3/2}} \mathrm{d}x' \mathrm{d}y'. \tag{5.7}$$

On application of the convolution theorem to Eq. (5.7) we get

$$b_x(\mathbf{k}, z) = g(\mathbf{k}, z) j_y(\mathbf{k}), \tag{5.8}$$

i.e. the two dimensional Fourier transform of the magnetic field, $b_x(\mathbf{k}, z)$, is related to the two dimensional transform of the y component of the current density $j_y(\mathbf{k})$, multiplied by a weighting function, $g(\mathbf{k}, z)$, which takes into account the distance between the current density and the plane at height z. This weighting function is also a Fourier transform of a Green's function and can be evaluated analytically as,

$$g(\mathbf{k}, z) = \frac{\mu_0 d}{2} e^{-kz}, \tag{5.9}$$

where $k = \sqrt{k_x^2 + k_y^2}$ and $\mathbf{k} = (k_x, k_y)$.

Similar equations may be found for b_y,

$$b_y(\mathbf{k}, z) = -g(\mathbf{k}, z) j_x(\mathbf{k}) \tag{5.10}$$

and b_z,

$$b_z(\mathbf{k}, z) = ig(\mathbf{k}, z) \left(\frac{k_y}{k} j_x(\mathbf{k}) - \frac{k_x}{k} j_y(\mathbf{k}) \right). \tag{5.11}$$

Equations (5.8), (5.10) and (5.11) give us, via an inverse Fourier transform, an easy way to determine the magnetic field from knowledge of the current density profile. A great strength of this technique is that it is equally easy to reverse the procedure to reconstruct the current density from the magnetic field profile, which would be measured in a BEC microscopy experiment. Knowledge of the x

component of the Fourier transform of the magnetic field gives, via

$$j_y(\mathbf{k}) = \frac{b_x(\mathbf{k}, z)}{g(\mathbf{k}, z)}, \tag{5.12}$$

the Fourier transform of the y component of the current density. Similar equations give j_y and j_z. It would initially appear that we can only obtain a single component of the current density from a measurement of a component of the magnetic field. However, as current density obeys the continuity equation

$$\nabla \cdot \mathbf{J} = 0, \tag{5.13}$$

which in Fourier space becomes,

$$-ik_x j_x(\mathbf{k}) - ik_y j_y(\mathbf{k}) = 0, \tag{5.14}$$

we can, in fact, obtain both of the two dimensional components of the current density from any single component of the magnetic field. As an example, using Eq. (5.14) with Eq. (5.12) gives a relationship between b_x and j_x

$$j_x(\mathbf{k}) = -\frac{2}{\mu_0 d}\frac{k_y}{k_x} e^{\sqrt{k_x^2+k_y^2}z} b_x(\mathbf{k}, z). \tag{5.15}$$

These inverse equations do have limitations. In the case of Eq. (5.15), if $k_x \to 0$, $\dfrac{k_y}{k_x} \to \infty$ indicating that a uniform current in the x direction, does not produce a magnetic field in the x direction. Thus, information about the magnetic field in a given direction is not sufficient to also gain information about the current density in the same direction. Additionally, Eq. (5.15) also approaches infinity as

$\sqrt{k_x^2 + k_y^2}$ approaches infinity. However this difficulty may be dealt with by using a high band pass filter, applied to the momentum space [76].

Additional filters may be required for other circumstances. In the inverse case, the Fourier transform of a real measured magnetic field profile will be dominated by high-frequency noise. If left in, this would be incorrectly attributed to the current density, rather than the magnetic field measuring method. A Hanning window [76] may be used to eliminate this noise,

$$W(k) = \begin{cases} 0.5[1 + \cos(\pi k/k_{max}], & k < k_{max} \\ 0, & k > k_{max} \end{cases}, \tag{5.16}$$

where the cut off frequency, k_{max}, must be determined empirically. If one is looking to find the measured magnetic field from a known current density, it is equally important to apply an appropriate filter to replicate the magnetic field measuring process [76, 74].

Having equipped ourselves with a set of equations with which to move between a magnetic field and the two dimensional current density producing it we can now, in the case of a 2DEG, go a step further and introduce another set of equations, with which to relate the current density to the underlying ionised donor distribution.

In the case of a typical 2DEG within a semiconductor hetero-junction, the electrostatic potential created by the ionised donors is partially screened. In the linear screening reqime, the screened electrostatic potential within the 2DEG is given by [77],

$$\Phi_{scr}(\mathbf{r}') = \frac{e^2}{4\pi\epsilon\epsilon_0} \int e^{-kd_0} \frac{n_d(\mathbf{k}) e^{i\mathbf{k}\cdot\mathbf{r}'}}{k + k_s} \mathrm{d}\mathbf{k}, \tag{5.17}$$

in which d_0 is the distance between the donor layer and the 2DEG, $n_d(\mathbf{k})$ is the Fourier transform of the ionised donor density, $\mathbf{r}'$ is a vector position in the 2DEG, ϵ is the permittivity of the semiconductor material and

$$k_s = \frac{e^2 m_e^*}{2\epsilon\epsilon_0 \pi \hbar^2} \tag{5.18}$$

is the screening wavevector, with m_e^* the effective electron mass.

The current density created by applying a small electric field, is then determined by the gradient of this potential according to,

$$\mathbf{j}(\mathbf{r}') = -\sigma \nabla \frac{\Phi_{scr}(\mathbf{r})}{e}, \tag{5.19}$$

where σ is the 2d conductivity of the 2DEG. In performing the Fourier transform to gain $j(\mathbf{k})$, as needed for the convolution equations, the derivative is multiplied by by the corresponding wave vector component to give

$$\mathbf{j}(\mathbf{k}) = -\sigma \frac{\Phi_{scr}(\mathbf{k})}{e} \mathbf{k}. \tag{5.20}$$

Using the expression for $\Phi_{scr}(\mathbf{k})$ that follows from the Fourier expression, Eq. (5.17) for $\Phi_{scr}(\mathbf{r})$, Eq. (5.20) becomes

$$\mathbf{j}(\mathbf{k}) = \sigma \, \mathbf{k} \, \frac{e}{2\epsilon\epsilon_0} \, e^{-kd_0} \, \frac{n_d(\mathbf{k})}{k + k_s}. \tag{5.21}$$

At this stage, we have a set of equations which can take us all the way from the donor density to a magnetic field and vice versa. The reliance of these equations on Fourier and inverse Fourier transforms, for which efficient numerical algorithms exist, enable fast efficient calculations of the various fields and densities.

Property	Value
Electron density, n_e	$3.3 \times 10^{15}\mathrm{m}^{-2}$
Fermi energy, ϵ_F	11.79 meV
Fermi velocity, v_F	$2.49 \times 10^5\ \mathrm{ms}^{-1}$
Fermi wavelength, λ_F	$4.3635 \times 10^{-8}\mathrm{m}$
Scattering time, τ_{sc}	$5.33 \times 10^{-11}\mathrm{s}$, $(1.9047 \times 10^{-13}\mathrm{s})$
Scattering length, L_{sc}	$13.29 \times 10^{-6}\mathrm{m}$, $(4.747 \times 10^{-7}\mathrm{m})$
Mobility, μ	$140\ \mathrm{m}^2(\mathrm{Vs})^{-1}$, $(0.5\mathrm{m}^2(\mathrm{Vs})^{-1})$
Conductivity, σ	$7.4 \times 10^{-2}\Omega^{-1}$, $(2.644 \times 10^{-4}\Omega^{-1})$
Donor - 2DEG distance	500 nm

Table 5.2: Relevent properties of the 2DEG, NU2239. In the cases with parentheses, parenthesised values are for room temperature, unparenthesised values correspond to $T = 4\mathrm{K}$.

5.3 The magnetic field from a 2DEG

Having established a model to calculate the magnetic field from a 2DEG, we now use this model to find the form of a typical magnetic field profile that might be experienced by a BEC. Throughout this section we have used values corresponding to a a 2DEG heterojunction structure, prepared within the University of Nottingham Semiconductor Physics Group (grown by M. Henini), identification code *NU2239*, whose properties are summarised in Table 5.2.

5.3.1 Relating the donor distribution to the magnetic field profile

Our starting point is a typical, uncorrelated, ionised donor distribution like that shown in Figure 5.1. This is characterised by an

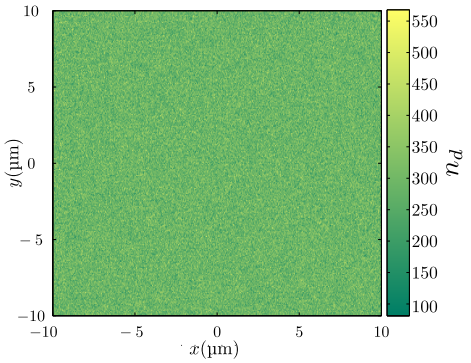

Figure 5.1: Colour map showing a section of the uncorrelated ionised donor density profile used in our calculations. This donor layer has an average donor density of 3.3×10^{15} m^{-2}

ensemble average,

$$\langle n_d(\mathbf{r}) n_d(\mathbf{r}') \rangle = n_d^2 \delta(\mathbf{r} - \mathbf{r}'), \tag{5.22}$$

which may be achieved through randomly placing N_d donors on an M-cell array, of area A. The total number of donors, N_d, is chosen to give an average density of $n_e = 3.3 \times 10^{15}$ m^{-2}, corresponding to sample NU2239.

We then used the linear screening model, Eq. (5.17), to calculate the effective screened potential that an electron in the 2DEG experiences. This screened potential was then converted into a current density, using Eq. (5.19).

The x-component of the magnetic field resulting from the current density was then numerically calculated, by Sinuco [77], using a standard Biot-Savart method. This was done for three different heights above the 2DEG, $z = 1, 3, 5$ µm, where a BEC might be held over a surface in an experiment.

The results are shown in Figure 5.2, which reveals inhomogeneous

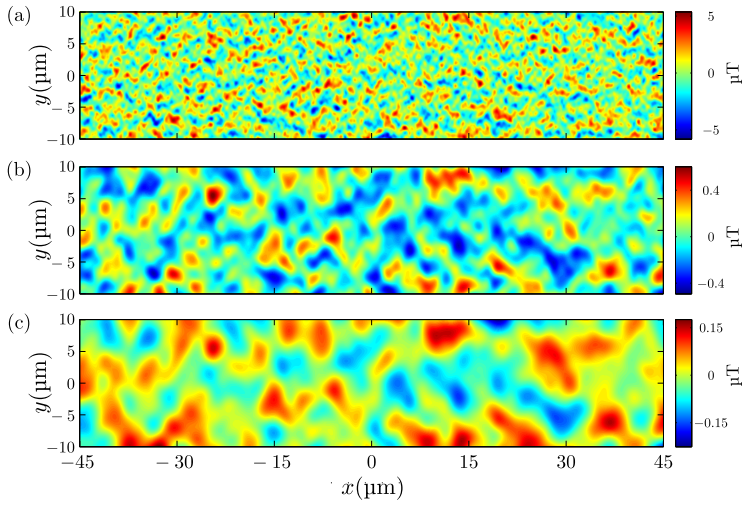

Figure 5.2: x-component of the magnetic field above a 2DEG, calculated using a Biot-Savart method, for the donor density shown in Figure 5.1, at temperature, $T = 4$ K. Panels correspond to the field at height (a) $z = 1$ µm (b) $z = 3$ µm (c) $z = 5$ µm

features originating from fluctuations in the ionised donor density. The intensity and length scale of these inhomogeneities drops off, due to the exponential term in Eq. (5.15), as the distance from the 2DEG increases. In all three cases, the values of the magnetic field, of order µT, and typical feature size, > 1 µm, are both well within the scope of BEC microscopy. It is worth noting that these results are for a cold, 4 K, 2DEG. At room temperature, the field magnitude produced by a given electric field applied to the 2DEG would be lower due to the reduced 2DEG conductivity. Specifically, the fields would then be in the nT range, representing a much harder, though still achievable, BEC microscopy situation.

We now compare the magnetic field profile obtained from the Biot-Savart law with that given by the convolution method, Eq. (5.8). Figure 5.3 shows a comparison of a sample section of the calculated fields, $B_x(x, y)$, at $z = 1$ µm. Comparison of the field profile ob-

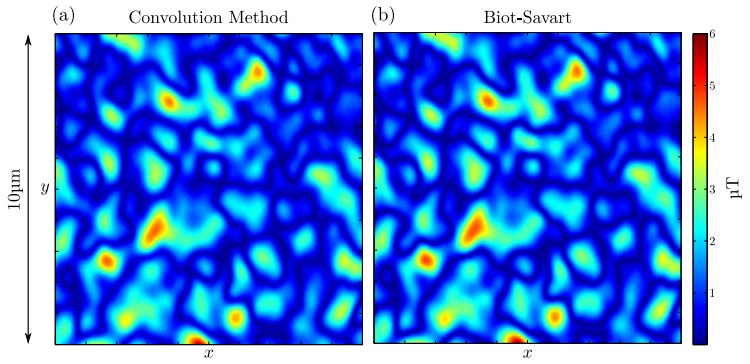

Figure 5.3: Comparison of a 10×10 μm section of $|B_x|$, sampled at height $z = 1$ μm computed using (a) the convolution (Fourier) method, (b) using the traditional, Biot-Savart method.

tained using the convolution method [Fig. 5.3(a)] and Biot-Savart law [Fig. 5.3(b)] reveals that the two methods do indeed produce near identical results, both qualitatively and quantitatively. But the large, fine, grids required to sample the current and, hence, calculate $|B_x|$ using the Biot-Savart law, meant that this method took days to compute $|B_x|$. By contrast, the convolution method produces the same results in less than a second. It is therefore clear that in any scenario where the magnetic field from a two dimensional structure is required, use of the convolution method is going to be highly advantageous to the experimentalist or theorist.

5.3.2 Magnetic field to current density

Having successfully used the convolution method to calculate the magnetic field from a known current density, we now attempt the reverse: to calculate the current density from a given field profile. We choose to start with the magnetic field calculated using the Biot-Savart law at the closest height above the 2DEG, $z = 1$ μm,

(Figure 5.2). We chose this field profile because it contains the greatest spatial detail with which to reconstruct the current density. The value of z, in fact, sets the expected resolution of the convolution method. Out calculations proceeded as follows. First, the $B_{x,z}$ field profile was fed in to Eq. (5.12) and Eq. (5.15) to find J_y and J_x. These current components were then compared to the original current density profiles, which were resampled to a 1μm resolution to be consistent with the expected resolution of the convolution method.

The results from this procedure are shown in Figure 5.4, with plots of the corresponding Fourier spectra shown in Figure 5.5. Again, the convolution method proved to be extremely computationally efficient, giving results in seconds. In both cases there is strong correlation, qualitatively and quantitatively, between the resampled original current densities and the values given via the convolution method. In the case of the y-component of the current density, J_y, the agreement is particularly good. The two current density profiles are near identical as seen by comparing panels (b) and (c) Figure 5.4. The results for the x-component, J_x, panels (e) and (f) Figure 5.4 also show some identically positioned features, some of which are highlighted by a dotted circle in Figure 5.4, which are quantitatively similar. However the agreement is less strong than for the y-component, as we now explain.

This discrepancy can be understood through consideration of the momentum space picture, Figure 5.5. When using the Fourier method on the magnetic field density, the momentum space [panels (b) and (d) Fig. 5.5], is greatly reduced in comparison to the original momentum space [panels (a) and (c) Fig. 5.5]. Despite this reduction

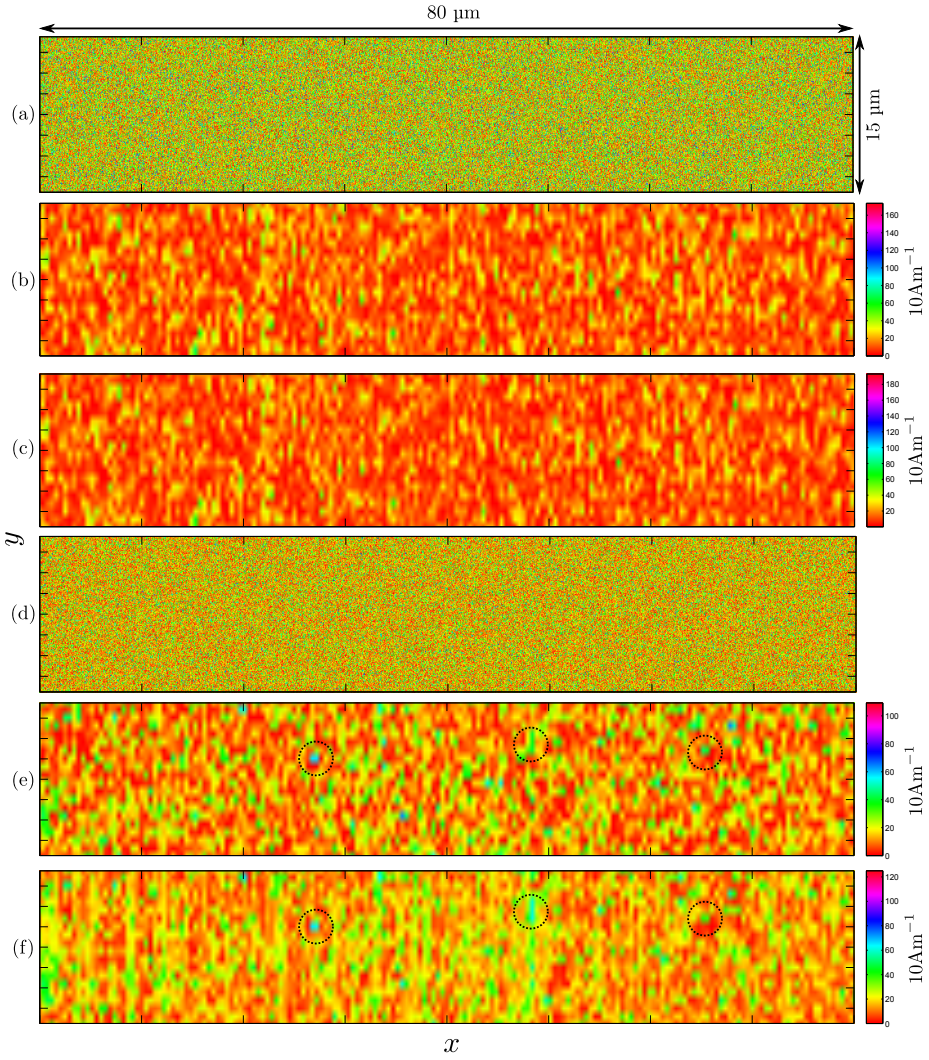

Figure 5.4: Current density profiles, calculated using two methods, for the sample whose ionised donor distribution is shown in Figure 5.1. (a) and (d) show J_y and J_x respectively, calculated using Eq. (5.19). (b) and (e) present the same data, resampled to a 1 µm resolution, to match that of the convolution method. (c) shows J_y calculated using the convolution method, from the $B_{x,y}$ data, in panel (a) of Figure 5.3. (f) is J_x calculated using Eq. (5.15). Some matching features are highlighted (by dotted circles) in (e) and (f).

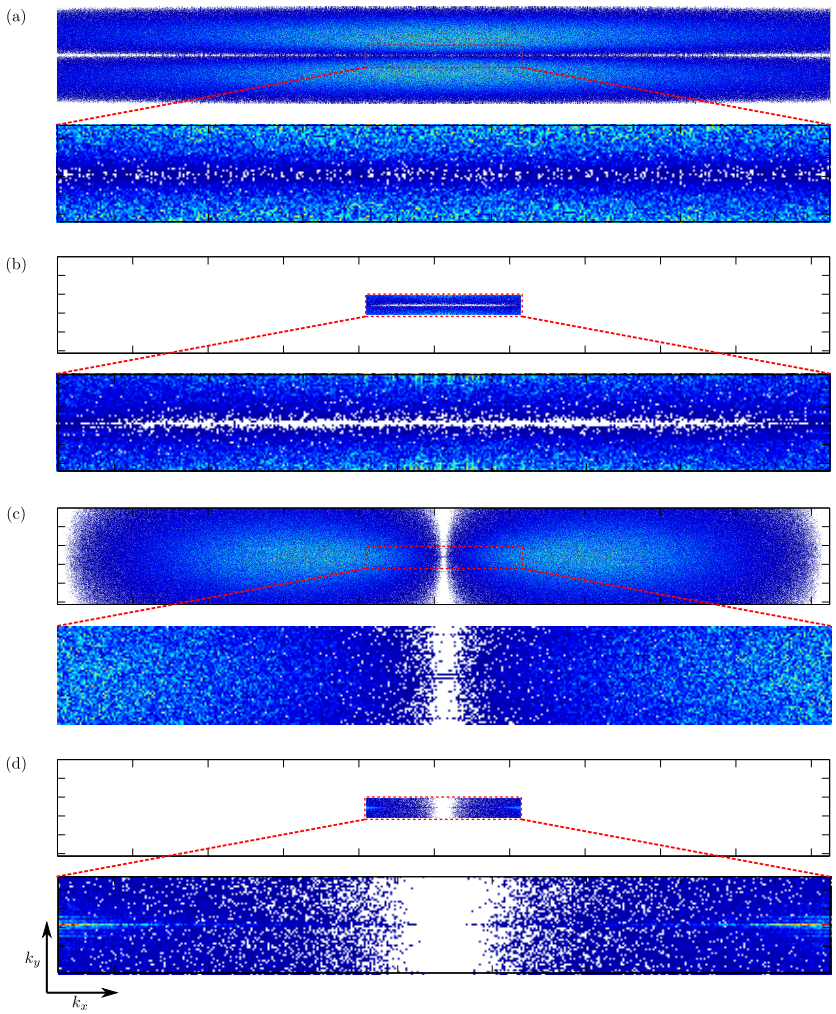

Figure 5.5: Plots illustrating momentum space information available to the Fourier method. (a) shows $J_y(k)$, the Fourier transform of the current density profile, as shown in Fig. 5.4 (a), calculated from the ionised donor density, Fig. 5.1. (b) also shows $J_y(k)$ but now calculated from the magnetic field profile, shown in Fig. 5.3 (b). Panels (c) and (d) are the equivalent plots for $J_x(k)$. Enlargements correspond to the area $k_i < k_{max}$, where k_{max} is limited by the height, z, at which the magnetic field is probed, in this case, 1 µm.

in information, the enlargements under each panel, which show the $k_i < k_{max}$ areas of both the convoluted magnetic field (b) and (d) and the original current density (a) and (c) are clearly similar hence the good match of current density profile, Figure 5.4.

The fact that the reconstructed current map, $J_x(x, y)$, obtained from the convolution method [Fig. 5.4 (e)] agreed less well than with the actual current flow than for $J_y(x, y)$ [Fig. 5.4 (b)] is explained by the noticeably more sparse momentum space, Fig. 5.5 (d) compared to Fig. 5.5 (b). This sparseness results from the additional operations in converting from J_y to J_x, Eq. (5.15).

It is clear that BEC microscopy, in combination with the convolution method explained above can map the current density profile of a 2DEG with resolution comparable to the separation of the BEC from the 2DEG.

It is also clear that due to the resolution limitations of the microscopy or convolution method, it is not possible to directly image patterns or features on the small length scales of the correlations within the donor density or current density. These features are both on the nm scale, so unless it becomes possible to hold a BEC at a similar, nm, separation, which would seem unlikely, it remains necessary to find another way to extract information about these short-range correlations.

5.3.3 Potential roughness from 2DEG wires

One way to gain insight into the correlations within the donor layer is to look at the root mean square (rms) average of the magnetic field fluctuations along the BEC, B_x^{rms}. In the case of the homogenous

donor distribution function, Eq. (5.22), this is given by

$$B_{x=0}^{rms}(z)^2 = \left(\frac{\mu_0 \sigma e}{4\epsilon\epsilon_0}\right)^2 \int\int \frac{k_y k_y' S(\mathbf{k},\mathbf{k}')}{(k+k_s)(k'+k_s)} e^{-(k+k')(d_0+z)} d^2\mathbf{k} d^2\mathbf{k}', \tag{5.23}$$

where $S(\mathbf{k},\mathbf{k}') = \langle \Delta n(\mathbf{k}) \Delta n(\mathbf{k}') \rangle$ is the correlation function of the ionised donor density fluctuations in Fourier space. In the case of a random, uncorrelated, donor density profile, as would be given through standard fabrication techniques, $S(\mathbf{k},\mathbf{k}') \propto \delta(\mathbf{k}+\mathbf{k}')$ [77]. Inserting this into Eq (5.23), shows that the root mean square average of the magnetic field fluctuations varies as $1/z^2$ [78].

Comparing this drop off in field fluctuations (the major limitation to near surface condensate experiments [57]) to that above a typical metal wire [79], shows that the *roughness* of the magnetic field from a 2DEG wire, of similar width, will be lower when $z \gtrsim 1.5$ µm [78].

While this is already an improvement on traditional conducting wires, 2DEG fabrication techniques allow us to lower B_x^{rms} yet further. Instead of using an uncorrelated donor distribution, it is possible to write periodic structures into the donor layer, either through ion implantation [80] or via optical illumination [81]. In this case, the correlation function of the periodically-patterned ionised donor distribution is not a delta function. As a result, $B_{x=0}^{rms}(z)$ decays exponentially with increasing z. Specifically, for a pattern with period $\Lambda = 2\pi/k_0$ and amplitude δn, Eq. (5.23) gives

$$B_{x=0}^{rms}(z)^2 = \left(\frac{\mu_0 \sigma e}{4\epsilon\epsilon_0}\right)^2 (\delta n)^2 \frac{4k_0^2}{(2k_0+k_s^2)^2} e^{-4k_0(d_0+z)}. \tag{5.24}$$

This patterning technique, which smoothes the magnetic field fluctuations, is similar to the patterned magnetic mirrors discussed in [82]

and allows one to create magnetic fields which are extremely smooth. Compared to a typical metal wire like that in [79], the field fluctuations above a patterned 2DEG wire are *three orders of magnitude smaller* at sub-micron BEC-wire separations [78].

The smooth and adaptable magnetic field profiles offered by patterned 2DEG wire structures hint at a possible new tool for use in BEC atom chip experiments. The smoothness of the fields at near surface ($\lesssim 1\mu$m) trapping distances is particularly exciting as it opens up the possibility of probing the sub-micron atom-surface regime, where many interesting physical effects such as the Casimir-Polder attraction occur.

5.3.4 Patterned structures

Having discussed the field profile created by current through a 2DEG, and the possibility of imprinting patterns in the donor distribution to modulate the field characteristics, we now shift our focus towards patterning the 2DEG itself, rather than the donor distribution.

Patterning the 2DEG is a fairly simple operation, normally done by using etching, to remove sections of 2DEG, leaving the desired pattern behind. A structure of some interest is an *antidot array*. Antidots are the conceptual opposites of quantum dots, areas in which there is no electron occupation. They are made by removing a, usually circular, section of the 2DEG. Arrays of antidot structures can induce resonant nonlinear electron transport, particularly when an magnetic field is applied, which can be used to probe 2DEG behaviour.

We use a relaxation method to calculate the current density

within a 2DEG whose density profile is patterned to approximate that of an antidot array. The potential energy of the array pattern is

$$V_{lattice} = V_0 \left(\sin\left(\frac{\pi x}{a}\right) \sin\left(\frac{\pi y}{a}\right) \right)^2, \tag{5.25}$$

where a gives the period of the lattice and V_0 is chosen to be large enough to fully deplete the 2DEG in the position of the antidots. We use the same electron density as for the NU2239 sample, $3.3\times10^{15}\mathrm{m}^{-2}$. This lattice, is then run through a relaxation method, which solves Laplace's equations, subject to the boundary conditions, in this case, a voltage drop of 1 mV across the array. The current density is then calculated using

$$\mathbf{J} = \sigma\mathbf{E}, \tag{5.26}$$

where σ is the conductivity of the 2DEG, for use with the convolution method.

Figure 5.6 shows the magnetic field profile, $B_x(x, y)$, calculated for three different lattice periods, $a = 1, 1.25, 1.5$ µm shown in panels (a), (b) and (c), all sampled at a height $z = 1$ µm. As expected from our previous investigations of the field profiles from a given current flow pattern (Section 5.3.1), if the patterning/correlations in the current density are $\sim z$, in this case when $a = 1$ µm, the field is approximately uniform. Field variations are on the nT scale and would therefore be too small to detect with existing BEC microscope sensitivity.

Even if it were possible to detect the field fluctuations from a sub-micron period lattice, due to the limitations on the momentum space within the convolution method, set by the height at which one

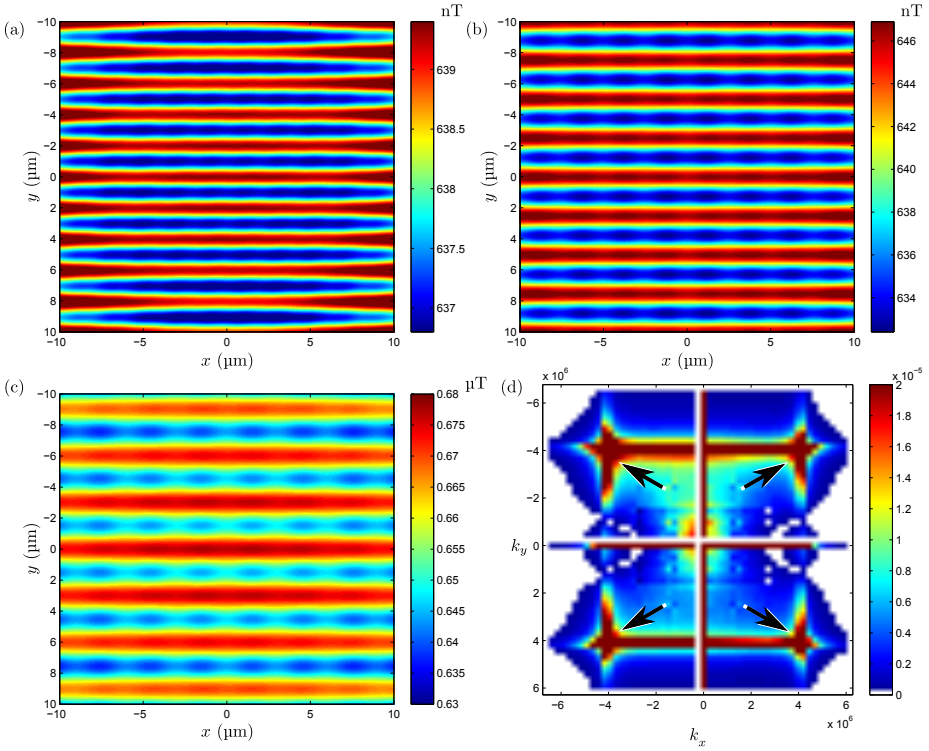

Figure 5.6: (a), (b) and (c) show $B_x(x, y)$ calculated at a distance $z = 1$ μm above current-carrying antidot arrays with periods of 1μm, 1.25μm and 1.5μm respectively. (d) shows the Fourier spectrum of (c), plotted for $k < k_{max}$. Positions of maxima corresponding to the $a = 1.5$ μm period of the antidot array are shown by black arrows.

is able to hold the condensate above the object (currently $z \gtrsim 1$ µm), reconstructing the current density using the convolution method would not reveal flow patterns originating from the periodic antidot potential.

On moving to antidot periods $a > z$, the results are much more promising. For $a = 1.25$ µm, the field varies by tens of nT and should therefore be detectable with a suitably designed BEC field microscope. When $a = 1.5$ µm, the field variations are now in the micro-Tesla range, detectable even with present, *crude*, BEC microscopy techniques. Consequently, current flow patterns imparted by the antidot array should be detectable using existing instuments.

Additionally, examination of, Fig. 5.6 (d), which shows the Fourier spectrum of the field profile for $a = 1.5$ µm, plotted for $k > k_{max}$, clearly reveals the peaks corresponding to the 1.5µm period of the antidot lattice, indicated by arrows on the figure. As a result, we are able to use the convolution method to recreate the current density through the antidot array, as shown in Figure 5.7.

In Section 5.3.3, we discussed the possibility that, by patterning the ionised donor density, it may be possible to hold a BEC at sub-micron distances from a surface. Figure 5.8 shows the magnetic field profile, $B_x(x, y)$, at a distance $z = 0.3$ µm above an antidot array with a period of 0.4 µm. It shows field variations on the tens of nT scale, which is detectable using BEC microscopy. Consequently, BEC microscopy may be able to image spatially-small patterns in a 2DEG, including individual quantum dots, provided the atoms can be held close enough i.e. at distances comparable to the scale of the pattern one wishes to image.

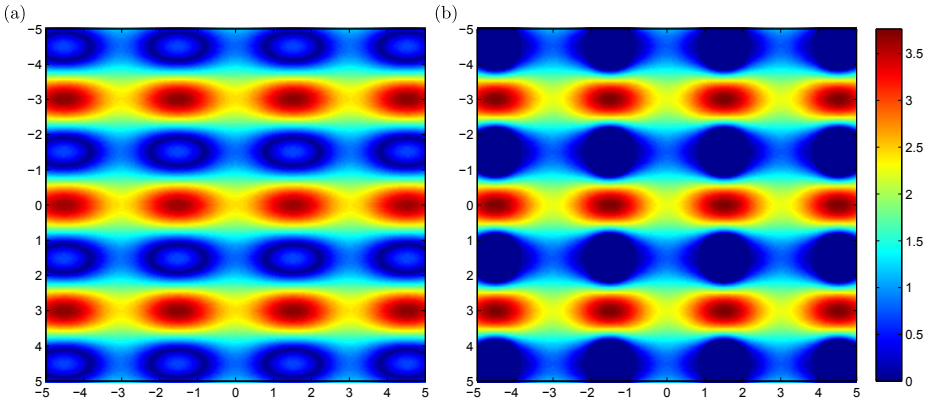

Figure 5.7: Current density profile of the antidot array with period $a = 1.5$ µm. (a) shows the current density profile reconstructed from the magnetic field landscape [Figure 5.6(c)]. For comparison (b) shows the original current density profile calculated using the relaxation method for comparison.

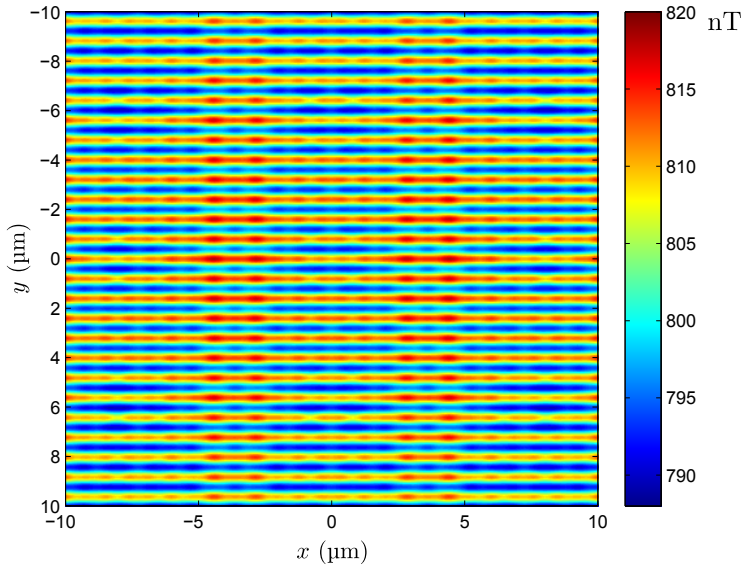

Figure 5.8: $B_x(x, y)$ at height $z = 0.3$ µm above a 0.4 µm period antidot array.

The choice of an antidot array is merely indicative of the possibilities fo using of BEC microscopy to image magnetic field profiles with feature sizes of order the cloud-device separation. Other situations have previously been considered, both for imaging and for manipulation of a condensate. For example, Sinuco [77] showed how the activation of a single conduction channel in a quantum point contact, is enough to completely split a BEC.

This class of experiment offers an ideal, non-invasive, way to image the behaviour of quantum electronic devices. Additionally, the use of engineered 2DEG structures provides a path to create small scale (sub-micron micro/nano Tesla) potential landscapes for use in condensate experiments. Such structures may be suitable for creating the sorts of potentials needed for the investigations into the behaviour of supersonic BECs in inhomogeneous landscapes, discussed in Chapter 4.

Appendix A

Details of the RK4IP-P

To conduct our numerical simulations of condensates, we evolve the GPE, using a fourth order Runge-Kutta method, developed for a system with interactions and with use of a projection operator, in the plane wave basis. We follow the implementation of this method detailed by Norrie [46].

In contrast to his work, we begin and end in real, rather than momentum space. The sequence for one time step iteration of the mode amplitudes, α_j is,

$$\alpha_j^h \leftarrow -i\Delta t P_j e^{-ik_j^2 \frac{\Delta t}{2}} FFT \left\{ \left[U_{ext}(t_i) + U_0 |\alpha_j^h| \right] \alpha_j^h \right\} \tag{A.1a}$$

$$\alpha_j^I \leftarrow e^{-ik_j^2 \frac{\Delta t}{2}} \alpha_j \tag{A.1b}$$

$$\alpha_j \leftarrow \alpha_j^I + \frac{1}{6}\alpha_j^h \tag{A.1c}$$

$$\alpha_j^h \leftarrow IFFT \left\{ \alpha_j^I + \frac{1}{2}\alpha_j^h \right\} \tag{A.1d}$$

$$\alpha_j^h \leftarrow -i\Delta t P_j FFT \left\{ \left[U_{ext}\left(t_i + \frac{\Delta t}{2} \right) + U_0 |\alpha_j^h| \right] \alpha_j^h \right\} \tag{A.1e}$$

$$\alpha_j \leftarrow \alpha_j + \frac{1}{3}\alpha_j^h \tag{A.1f}$$

$$\alpha_j^h \leftarrow IFFT\left\{\alpha_j^I + \frac{1}{2}\alpha_j^h\right\} \tag{A.1g}$$

$$\alpha_j^h \leftarrow -i\Delta t P_j FFT\left\{\left[U_{ext}\left(t_i + \frac{\Delta t}{2}\right) + U_0|\alpha_j^h|\right]\alpha_j^h\right\} \tag{A.1h}$$

$$\alpha_j \leftarrow \alpha_j + \frac{1}{3}\alpha_j^h \tag{A.1i}$$

$$\alpha_j^h \leftarrow IFFT\left\{e^{-ik_j^2\frac{\Delta t}{2}}[\alpha_j^I + \alpha_j^h]\right\} \tag{A.1j}$$

$$\alpha_j^h \leftarrow -i\Delta t P_j FFT\left\{\left[U_{ext}\left(t_i + \Delta t\right) + U_0|\alpha_j^h|\right]\alpha_j^h\right\} \tag{A.1k}$$

$$\alpha_j \leftarrow e^{-ik_j^2\frac{\Delta t}{2}}\alpha_j + \frac{1}{6}\alpha_j^h \tag{A.1l}$$

$$\alpha_j^h \leftarrow IFFT\{\alpha_j\}. \tag{A.1m}$$

In which FFT and $IFFT$ correspond to forward and inverse Fourier transforms, performed using the FFTW3 algorithm. As mentioned in Chapter 3, part of the motivation for use of this algorithm was its numerical efficiency. On examination, only α_j^h requires the full, padded grid, α_j^I, α_j and $e^{-ik_j^2}$ can be stored on a reduced grid, whose length is given by the size of the low energy subspace modes.

References

[1] E. Fermi. Sulla quantizzazione del gas perfetto monoatomico. *Rend. Lincei*, 3:145, 1926.

[2] P. A. M. Dirac. On the theory of quantum mechanics. *Proceedings of the Royal Society of London. Series A*, 112:661, 1926.

[3] W. Pauli. *Exclusion principle and quantum mechanics*. Éds. du Griffon, 1947.

[4] C. J. Pethick and H. Smith. *Bose-Einstein Condensation in Dilute Gases*. Cambridge University Press, 2008.

[5] S. N. Bose. Plancks gesetz und lichtquantenhypothese. *Z. Phys*, 26:178, 1924.

[6] A. Einstein. Quantentheorie des einatomigen idealen Gases II. *Sitz. Preess. Akad. Wiss.*, 1:3, 1925.

[7] J. Wilks and J. Wilks. *The properties of liquid and solid helium*. Clarendon Press Oxford, 1967.

[8] F. London. The l-Phenomenon of Liquid Helium and the Bose-Einstein Degeneracy. *Nature*, 141:643, 1938.

[9] M. H. Anderson, J. R. Ensher, M. R. Matthews, C. E. Wieman, E. A. Cornell, et al. Observation of Bose-Einstein condensation in a dilute atomic vapor. *Science*, 269(5221):198–201, 1995.

[10] K. B. Davis, M. O. Mewes, M. R. Andrews, N. J. Van Druten, D. S. Durfee, D. M. Kurn, and W. Ketterle. Bose-Einstein condensation in a gas of sodium atoms. *Phys. Rev. Lett.*, 75(22):3969–3973, 1995.

[11] B. M. Caradoc-Davies, R. J. Ballagh, and K. Burnett. Coherent Dynamics of Vortex Formation in Trapped Bose-Einstein Condensates. *Phys. Rev. Lett.*, 83:895–898, Aug 1999.

[12] T. van Zoest, N. Gaaloul, Y. Singh, H. Ahlers, W. Herr, S. T. Seidel, W. Ertmer, E. Rasel, M. Eckart, E. Kajari, et al. Bose-Einstein condensation in microgravity. *Science*, 328(5985):1540–1543, 2010.

[13] S. Chu, C. Cohen-Tannoudji, and W. D. Philips. For development of methods to cool and trap atoms with laser light. *Nobel Prize in Physics*, pages 4–10, 1997.

[14] E. A. Cornell, W. Ketterle, and C. E. Wieman. For the achievement of Bose-Einstein condensation in dilute gases of alkali atoms, and for early fundamental studies of the properties of the condensates. *Nobel Prise in Physics*, 2001.

[15] F. Dalfovo, S. Giorgini, L. P. Pitaevskii, and S. Stringari. Theory of Bose-Einstein condensation in trapped gases. *Reviews of Modern Physics*, 71(3):463–512, 1999.

[16] V. S. Mathur and S. P. Singh. *Concepts in quantum mechanics*. Chapman & Hall/CRC, 2008.

[17] W. Krauth. Quantum Monte Carlo Calculations for a Large Number of Bosons in a Harmonic Trap. *Phys. Rev. Lett.*, 77:3695–3699, Oct 1996.

[18] N. N. Bogoliubov. On the theory of superfluidity. *J. phys. (USSR)*, 11(23):4–2, 1947.

[19] E. P. Gross. Structure of a quantized vortex in boson systems. *Il Nuovo Cimento*, 20(3):454–477, 1961.

[20] E. P. Gross. Hydrodynamics of a superfluid condensate. *Journal of Mathematical Physics*, 4:195, 1963.

[21] L. P. Pitaevskii. Vortex lines in an imperfect Bose gas. *Sov. Phys. JETP*, 13(2):451–454, 1961.

[22] P. Kapitza. Viscosity of liquid helium below the l-point. *Nature*, 141(3558):74, 1938.

[23] J. F. Allen and A. D. Misener. Flow of liquid helium II. *Nature*, 141(3558):75, 1938.

[24] I. M. Khalatnikov. *An Introduction to the Theory of Superfluidity*. Addison-Wesley Publishing, 1989.

[25] L. D. Landau and E. M. Lifshitz. *Fluid Mechanics*, volume 6. Butterworth-Heinemann, 1987.

[26] J. R. Abo-Shaeer, C. Raman, J. M. Vogels, and W. Ketterle. Observation of vortex lattices in Bose-Einstein condensates. *Science*, 292(5516):476–479, 2001.

[27] A. Einstein. On the quantum mechanics of radiation. *Physikalische Zeitschrift*, 18:121–128, 1917.

[28] D. Wineland and H. Dehmelt. Proposed $1014\delta\nu/\nu$ laser fluorescence spectroscopy on Tl+ mono-ion oscillator. *Bull. Am. Phys. Soc*, 20:637, 1975.

[29] T. W. Hänsch and A. L. Schawlow. Cooling of gases by laser radiation. *Optics Communications*, 13(1):68–69, 1975.

[30] W. H. Wing. On neutral particle trapping in quasistatic electromagnetic fields. *Progress in Quantum Electronics*, 8(3):181–199, 1984.

[31] J. Reichel. Microchip traps and Bose–Einstein condensation. *Applied Physics B: Lasers and Optics*, 74(6):469–487, 2002.

[32] M. Cristiani, O. Morsch, J. H. Müller, D. Ciampini, and E. Arimondo. Experimental properties of Bose-Einstein condensates in one-dimensional optical lattices: Bloch oscillations, Landau-Zener tunneling, and mean-field effects. *Phys. Rev. A*, 65:063612, Jun 2002.

[33] I. B. Spielman, W. D. Phillips, and J. V. Porto. Mott-Insulator Transition in a Two-Dimensional Atomic Bose Gas. *Phys. Rev. Lett.*, 98:080404, Feb 2007.

[34] L. Pitaevskii and S. Stringari. *Bose-Einstein Condensation*. Oxford Science Publications, 2003.

[35] S. L. Cornish, N. R. Claussen, J. L. Roberts, E. A. Cornell, and C. E. Wieman. Stable ^{85}Rb Bose-Einstein Condensates with Widely Tunable Interactions. *Phys. Rev. Lett.*, 85:1795–1798, Aug 2000.

[36] A. M. Kaufman, R. P. Anderson, Thomas M. Hanna, E. Tiesinga, P. S. Julienne, and D. S. Hall. Radio-frequency dressing of multiple Feshbach resonances. *Phys. Rev. A*, 80:050701, Nov 2009.

[37] B. L. Lev. *Magnetic microtraps for cavity QED, Bose-Einstein condensates, and atom optics*. PhD thesis, California Institute of Technology, 2005.

[38] D. S. Durfee. *Dynamic Properties of Dilute Bose-Einstein Condensates*. PhD thesis, Department of Physics, Massachusetts Institute of Technology, 1999.

[39] A. Robert, O. Sirjean, A. Browaeys, J. Poupard, S. Nowak, D. Boiron, C. I. Westbrook, and A. Aspect. A Bose-Einstein condensate of metastable atoms. *Science*, 292(5516):461–464, 2001.

[40] O. Sirjean, S. Seidelin, J. V. Gomes, D. Boiron, C.I. Westbrook, A. Aspect, and G. V. Shlyapnikov. Ionization rates in a Bose-Einstein condensate of metastable helium. *Phys. Rev. Lett.*, 89(22):220406, 2002.

[41] S. Seidelin, J. V. Gomes, R. Hoppeler, O. Sirjean, D. Boiron, A. Aspect, and C. I. Westbrook. Getting the elastic scattering length by observing inelastic collisions in ultracold metastable helium atoms. *Phys. Rev. Lett.*, 93(9):90409, 2004.

[42] T. Gericke, C. Utfeld, N. Hommerstad, and H. Ott. A scanning electron microscope for ultracold atoms. *Laser Physics Letters*, 3(8):415–419, 2006.

[43] T. Gericke, P. Würtz, D. Reitz, T. Langen, and H. Ott. High-resolution scanning electron microscopy of an ultracold quantum gas. *Nature Physics*, 4(12):949–953, 2008.

[44] P. Würtz, T. Langen, T. Gericke, A. Koglbauer, and H. Ott. Experimental demonstration of single-site addressability in a two-dimensional optical lattice. *Phys. Rev. Lett.*, 103(8):80404, 2009.

[45] N. P. Proukakis and B. Jackson. Finite-temperature models of Bose–Einstein condensation. *Journal of Physics B: Atomic, Molecular and Optical Physics*, 41(20):203002, 2008.

[46] A. A. Norrie. *A classical field treatment of colliding Bose-Einstein condensates*. PhD thesis, PhD thesis University of Otago, New Zealand, 2005.

[47] M. Frigo and S. G. Johnson. The design and implementation of FFTW3. *Proceedings of the IEEE*, 93(2):216–231, 2005.

[48] R. G. Scott, A. M. Martin, T. M. Fromhold, and F. W. Sheard. Anomalous Quantum Reflection of Bose-Einstein Condensates

from a Silicon Surface: The Role of Dynamical Excitations. *Phys. Rev. Lett.*, 95:073201, Aug 2005.

[49] T. A. Pasquini, M. Saba, G.-B. Jo, Y. Shin, W. Ketterle, D. E. Pritchard, T. A. Savas, and N. Mulders. Low Velocity Quantum Reflection of Bose-Einstein Condensates. *Phys. Rev. Lett.*, 97(9):093201, 2006.

[50] Y. Shin, M. Saba, T. A. Pasquini, W. Ketterle, D. E. Pritchard, and A. E. Leanhardt. Atom Interferometry with Bose-Einstein Condensates in a Double-Well Potential. *Phys. Rev. Lett.*, 92(5):050405, Feb 2004.

[51] KW Madison, F. Chevy, W. Wohlleben, and J. Dalibard. Vortex formation in a stirred Bose-Einstein condensate. *Phys. Rev. Lett.*, 84(5):806–809, 2000.

[52] S. Burger, K. Bongs, S. Dettmer, W. Ertmer, K. Sengstock, A. Sanpera, G. V. Shlyapnikov, and M. Lewenstein. Dark solitons in Bose-Einstein condensates. *Phys. Rev. Lett.*, 83(25):5198–5201, 1999.

[53] M. Lewenstein, A. Sanpera, V. Ahufinger, B. Damski, A. Sen, and U. Sen. Ultracold atomic gases in optical lattices: mimicking condensed matter physics and beyond. *Advances in Physics*, 56(2):243–379, 2007.

[54] D. L. Price, M. L. Saboungi, and F. J. Bermejo. Dynamical aspects of disorder in condensed matter. *Reports on Progress in Physics*, 66(4):407, 2003.

[55] J. Billy, V. Josse, Z. Zuo, A. Bernard, B. Hambrecht, P. Lugan, D. Clément, L. Sanchez-Palencia, P. Bouyer, and A. Aspect. Direct observation of Anderson localization of matter waves in a controlled disorder. *Nature*, 453(7197):891–894, 2008.

[56] G. Roati, C. D'Errico, L. Fallani, M. Fattori, C. Fort, M. Zaccanti, G. Modugno, M. Modugno, and M. Inguscio. Anderson localization of a non-interacting Bose-Einstein condensate. *Nature*, 453(7197):895–898, 2008.

[57] P. Krüger, L. M. Andersson, S. Wildermuth, S. Hofferberth, E. Haller, S. Aigner, S. Groth, I. Bar-Joseph, and J. Schmiedmayer. Potential roughness near lithographically fabricated atom chips. *Phys. Rev. A*, 76:063621, Dec 2007.

[58] R. Gilmore. *Elementary quantum mechanics in one dimension*. Johns Hopkins University Press, 2004.

[59] N. Pavloff. Breakdown of superfluidity of an atom laser past an obstacle. *Phys. Rev. A*, 66(1):013610, Jul 2002.

[60] T. Paul, M. Hartung, K. Richter, and P. Schlagheck. Nonlinear transport of Bose-Einstein condensates through mesoscopic waveguides. *Phys. Rev. A*, 76:063605, Dec 2007.

[61] M. Albert, T. Paul, N. Pavloff, and P. Leboeuf. Dipole Oscillations of a Bose-Einstein Condensate in the Presence of Defects and Disorder. *Phys. Rev. Lett.*, 100(25):250405, 2008.

[62] C. A. Sackett, J. M. Gerton, M. Welling, and R. G. Hulet. Measurements of collective collapse in a Bose-Einstein condensate

with attractive interactions. *Phys. Rev. Lett.*, 82(5):876–879, 1999.

[63] H. A. Ishkhanyan and V. P. Krainov. Multiple-scale analysis for resonance reflection by a one-dimensional rectangular barrier in the Gross-Pitaevskii problem. *Phys. Rev. A*, 80:045601, 2009.

[64] S. Flügge. *Practical quantum mechanics*. Springer Verlag, 1994.

[65] L. D. Landau, E. M. Lifshitz, J. B. Sykes, J. S. Bell, and M. E. Rose. *Quantum Mechanics: Non-Relativistic Theory*. Butterworth-Heinemann, 1977.

[66] F. Cooper, A. Khare, and U. P. Sukhatme. *Supersymmetry in quantum mechanics*. World Scientific Publishing Company Incorporated, 2001.

[67] N. Kiriushcheva and S. Kuzmin. Scattering of a Gaussian wave packet by a reflectionless potential. *American Journal of Physics*, 66:867, 1998.

[68] Timothy Cox and John Lekner. Reflection and non-reflection of particle wavepackets. *European Journal of Physics*, 29(4):671–679, July 2008.

[69] Er'el Granot and Avi Marchewka. Universal potential-barrier penetration by initially confined wave packets. *Physical Review A*, 76(1):012708, July 2007.

[70] John Lekner. Reflectionless eigenstates of the sech(2) potential. *American Journal of Physics*, 75(12):1151–1157, December 2007.

[71] Chang-Soo Park. Transmission time of a particle in the reflectionless Sech-squared potential: Quantum clock approach. *Physics Letters A*, 375(38):3348–3354, September 2011.

[72] Chang-Soo Park. Scattering Times In the Modified Poschl-teller Potential Well. *Modern Physics Letters B*, 26(8):1250046, March 2012.

[73] Christian Wickles and Wolfgang Belzig. Reflectionless transport of surface Dirac fermions on topological insulators with induced ferromagnetic domain walls. *Physical Review B*, 86(3):035151, July 2012.

[74] S. Wildermuth, S. Hofferberth, I. Lesanovsky, S. Groth, P. Krüger, J. Schmiedmayer, and I. Bar-Joseph. Sensing electric and magnetic fields with Bose-Einstein condensates. *Applied Physics Letters*, 88:264103, 2006.

[75] S. Wildermuth. *One-dimensional Bose-Einstein condensates in micro-traps*. PhD thesis, University of Heidelberg, 2005.

[76] B. J. Roth, N. G. Sepulveda, and J. P. Wikswo. Using a magnetometer to image a two dimensional current distribution. *Journal of Applied Physics*, 65(1):361–372, 1989.

[77] G. Sinuco. *Quantum properties of Bose-Einstein condensates coupled to semiconductor heterojunctions*. PhD thesis, University of Nottingham, 2010.

[78] G. Sinuco, B. Kaczmarek, P. Krüger, and T. M. Fromhold. Atom chips with two-dimensional electron gases: Theory of near-

surface trapping and ultracold-atom microscopy of quantum electronic systems. *Phys. Rev. A*, 83(2):021401, 2011.

[79] T. Schumm, J. Estève, C. Figl, J.B. Trebbia, C. Aussibal, H. Nguyen, D. Mailly, I. Bouchoule, C. I. Westbrook, and A. Aspect. Atom chips in the real world: the effects of wire corrugation. *The European Physical Journal D-Atomic, Molecular, Optical and Plasma Physics*, 32(2):171–180, 2005.

[80] K. Ensslin and P. M. Petroff. Magnetotransport through an antidot lattice in GaAs-Al_ {x} Ga_ {1-x} As heterostructures. *Phys.Rev. B*, 41(17):12307, 1990.

[81] JJ Koonen, H. Buhmann, and LW Molenkamp. Probing the potential landscape inside a two-dimensional electron Gas. *Phys. Rev. Lett.*, 84(11):2473–2476, 2000.

[82] E. A. Hinds and I. G. Hughes. Magnetic atom optics: mirrors, guides, traps, and chips for atoms. *Journal of Physics D: Applied Physics*, 32:R119–R146, 1999.